Targeting ATP2B1 impairs PI3K/Akt/Fox-O3 signaling and reduces SARS-COV-2 replication *in vivo*.

Pasqualino de Antonellis[1,2]*, Veronica Ferrucci [1,2]*, Francesca Bibbo [1,2$], Fathemeh Asadzadeh[1-2$], Francesca Gorini[2], Angelo Boccia[1,2], Carmen Sorice[1,2], Roberto Siciliano[1], Roberta Russo[1,2], Immacolata Andolfo[1,2], Vito Alessandro Lasorsa[1,2], Sueva Cantalupo[1,2], Giovanni Paolella[1,2], Giovanna Fusco[3], Maurizio Viscardi[3], Sergio Brandi[3], Bianca Maria Pierri[3], Pellegrino Cerino[3], Vittoria Monaco[1,4], Dong-Rac choi[5,6], Jae-Ho Cheong[6], Maria Monti[1,4], Achille Iolascon[1,2], Stefano Amente[2], Mario Capasso[1,2], Hong-Yeoul Kim[6#] and Massimo Zollo[1,2,7,8#]

1 CEINGE Biotecnologie Avanzate, Naples, 80145, Italy
2 Dipartimento di Medicina Molecolare e Biotecnologie Mediche (DMMBM), 'Federico II' University of Naples, Naples, 80131, Italy
3 Istituto Zooprofilattico Sperimentale del Mezzogiorno, Naples, 80055, Italy
4 Department of Chemical Sciences, University 'Federico II' University of Naples, Naples 80125, Italy.
5 Department of Surgery, Yonsei University College of Medicine, Seoul, Korea
6 HAIM BIO Co. Ltd, Industrial Park, Korea University, Seoul, South Korea
7 DAI Medicina di Laboratorio e Trasfusionale, 'Federico II' University of Naples, 80131 Naples, Italy
8 Lead contact

(*) co-first
($) co-second
(#) corresponding authors

Correspondence:
massimo.zollo@unina.it (M.Z.)
hykim@haimbio.com (H.Y.K.)

Abstract

ATP2B1 is a known regulator of calcium (Ca^{2+}) cellular export and homeostasis. Diminished levels of extra- or intra-cellular Ca^{2+} content have been suggested to block SARS-CoV-2 replication. Here, we demonstrate that a newly nontoxic caloxin-derivative compound (PI-7) inhibits ATP2B1, reduces the extra- and intra-cellular Ca^{2+} levels and impairs SARS-CoV-2 replication and propagation (VOCs: Delta and Omicron 2), as also measured by inhibition of syncytia *in vitro*. Furthermore, a FOXO3 transcriptional site of regulation of expression at the 5' end of the *ATP2B1* locus, together with a rare homozygous intronic variant in the *ATP2B1* locus (rs11337717; chr12:89643729, T>C), are shown to be associated with severity of COVID19 (symptomatic *versus* asymptomatic patients). Here, we identify the mechanism of action during SARS-CoV-2 infection, which involves the PI3K/Akt signaling pathway, inactivation of FOXO3 (i.e., phosphorylation), and inhibition of transcriptional control of both membrane and reticulum Ca^{2+} pumps (ATP2B1 and *ATP2A1* [i.e., SERCA1], respectively). The pharmacological action of compound PI-7 on sustaining both *ATP2B1* and *ATP2A1* expression reduces the intracellular cytoplasmic Ca^{2+} pool and thus negatively influences SARS-CoV-2 replication and propagation. As compound PI-7 shows a lack of toxicity, its prophylactic use as a therapy against the COVID19 pandemic is here proposed.

In brief

De Antonellis et al. shows the importance of the Ca^{2+} channel pump ATP2B1 in the regulation of extracellular and intracellular Ca^{2+} levels that positively influence SARS-CoV-2 replication in human cells. Our study identifies the mechanism of action of SARS-CoV-2 in the regulation of the expression of *ATP2B1* and *ATP2A1* loci during infection via FOXO3 transcriptional factor. Furthermore, a small caloxin-derivative molecule (compound PI-7) can inhibit ATP2B1 activity, thus resulting in SARS-CoV-2 impairment. In further support, we have identified a genetic variant within the noncoding upstream region of *ATP2B1* in symtomatic patients affected by severe COVID19, thus indicating this polymorphism as a genetic predisposition factor to SARS-CoV-2 infection.

SHORT Title:

ATP2B1 (*PMCA1*) regulated by FOXO3 is a target for COVID19 therapy

Key words: SARS-CoV-2, ATP2B1, ATP2A1, PI3K/Akt , Ca^{2+}, endoplasmic reticulum, FOXO3

Highlights:

1. An anti-viral model of network of action for ATP2B1 against SARS-CoV-2 at the intracellular level that involves the PI3K/Akt signaling pathway, inactivation (i.e., phosphorylation) of FOXO3 and its transcriptional control, and inhibition of both membrane and reticulum Ca^{2+} pumps (i.e., ATP2B1, ATP2A1, respectively).

2. A new drug and its lack of toxicity “compound PI-7”, thus envisioning both preventive and therapeutic applications in patients with COVID-19.

3. The specificity of action in the context of Ca^{2+} homeostasis is one of the strategies that coronaviruses (including SARS-CoV-2 and any new VOC, including Omicron 2) use to infect host cells and promote organ dysfunction.

4. Therapeutic applications for compound PI-7 against all other viruses belonging to the Coronoviridae family (e.g., SARS-CoV, MERS-CoV), and against the main families of positive sense ssRNA viruses from other hosts (e.g., Nidovirales), as these are all Ca^{2+} dependent.

5. Identification of a rare homozygous intronic variant in the *ATP2B1* locus (rs11337717; chr12:89643729, T>C) that is associated with severity of COVID19 (i.e., symptomatic *versus* asymptomatic patients). This variant can be used as a marker to identify those patients that might show severe COVID19 following their SARS-COV-2 infection.

Introduction

The coronavirus disease 2019 (COVID19) pandemic is one of the worst crises of our times, which prompted the urgent need to uncover the mechanisms that have pivotal roles with severe acute respiratory syndrome coronavirus 2 (SARS-CoV-2). SARS-CoV-2 uses multiple approaches to infect its host (Baggen et al., 2021), to evade the host responses that are still poorly understood (Xie and Chen, 2020). SARS-CoV-2 infection shows a wide range of clinical features, which range from asymptomatic to mild and severe, which mainly depends on both host genetic factors and virus–host interactions.

Coronaviruses (CoVs) contain positive-sense, single-stranded RNA (~30 kb). Four major categories have been reported, with alphaCoV and betaCoV known to infect humans. Those that can replicate in the lower respiratory tract cause pneumonia, which can be fatal (Tay et al., 2020); they include SARS-CoV, Middle East respiratory syndrome-CoV, and the new SARS-CoV-2. This last CoV belongs to the betaCoV genus (Andersen et al., 2020) and has resulted in pandemic acute respiratory syndrome in humans (i.e., COVID19 disease). This can progress to acute respiratory distress syndrome, generally around 8 to 9 days after symptom onset (Huang et al., 2020). Like the other respiratory CoVs, SARS-CoV-2 is transmitted via respiratory droplets, with possible fecal–oral transmission (Huang *et al.*, 2020).

When SARS-CoV-2 infects host cells, according to the discontinuous transcription mechanism its full-length positive-sense genomic RNA (gRNA) is used to produce both full-length negative-sense RNA copies (–gRNAs) and subgenomic negative-sense RNAs (–sgRNAs) that act as templates for the synthesis of positive gRNA and sgRNA, respectively. Among those sgRNAs, four encode the structural viral proteins Spike (S), Envelope (E), Membrane (M) and Nucleoprotein (N) (Kim et al., 2020; V'Kovski et al., 2021). To date, the most recognized receptor used by SARS-CoV-2 to enter host cells is angiotensin-converting enzyme 2 (ACE2), which is mainly expressed in lung and intestine, and to a lesser extent in kidney, heart, adipose, brain, and reproductive tissues (Lukassen et al., 2020; Walls et al., 2020; Wrapp et al., 2020), together with the cellular serine protease TMPRSS2. Binding to the host ACE2 receptor is mediated by the viral S protein, which consists of two noncovalently associated subunits: the S1 subunit that binds ACE2, and the S2 subunit that anchors the S protein to the membrane. The S2 subunit also includes a fusion peptide and other machinery necessary to mediate membrane fusion upon infection of a new cell. Furthermore, ACE2 engagement by the virus exposes an additional site internal to the S2 subunit, termed the S2′ site; following ACE2-mediated endocytosis, the S2’ site is cleaved by the transmembrane protease serine 2 (TMPRSS2) at the cell surface, or by cathepsin L in the endosomal compartment (Jackson et al., 2022). This "priming" process triggers the fusion of the viral envelope with cellular membranes, thereby allowing the release of the viral genome into the host cell (Hoffmann et al., 2020; Jackson *et al.*, 2022). Despite data showing that ACE2 is a high-affinity receptor for SARS-CoV-2 (Lan et al., 2020), several lines of evidence have suggested that other factors are involved in the priming process.

Calcium (Ca^{2+}) signals have long been known to have an essential role during the viral cycle (i.e., virion structure formation, virus entry, viral gene expression, posttranslational processing of viral proteins, and virion maturation and release [Zhou et al., 2009]). The role of Ca^{2+} in virus–host cell interactions has been shown for various types of envelope viruses (e.g., Rubella virus [Dube et al., 2014], Ebola virus [Nathan et al., 2020]), including CoVs (Berlansky et al., 2022). In this regard, the depletion of extra- and/or intra-cellular Ca^{2+} pools was shown to significantly reduce the infectivity of SARS-CoV, thus suggesting that both the plasma membrane and endosomal cell entry pathways (Lai et al., 2017) are regulated by Ca^{2+}. Of importance, recent studies have also provided evidence that the use of Ca^{2+} channel blockers (e.g., amlodipine, nifedipine) can reduce mortality from COVID19 (Crespi and Alcock, 2021), thus further underlining the importance of Ca^{2+} in SARS-CoV-2 infection and replication.

Intracellular and organellar Ca^{2+} concentrations are tightly controlled via various pumps, including the calcium pumps (Ca^{2+} ATPases). Among the plasma membrane Ca^{2+} pumps, the plasma membrane Ca^{2+} ATPases (PMCAs) are ATP-driven Ca^{2+} pumps that are ubiquitously expressed in the plasma membrane of all eukaryotic cells. The PMCA proteins are encoded by four genes (*ATP2B1-4*) with numerous splice variants that modulate their tissue distribution, cellular localization, and functional diversity (Krebs, 2015). Among the *ATP2Bs* genes, the homozygous deletion of the *ATP2B1* gene in mice was shown to give rise to a lethal phenotype, thus suggesting that ATP2B1 has a role as the housekeeping isoform (Okunade et al., 2004) required for the maintenance of intracellular Ca^{2+}. Indeed, ATP2B1 is critical for the maintenance of cytosolic Ca^{2+} concentrations below 300 nM (i.e., at ~100 nM), due to its high affinity for Ca^{2+} (Kd, ~0.2 M)[17,18], and it represents the major Ca^{2+} efflux pathway in nonexcitable cells (Muallem et al., 1988), with an important role in regulation of the frequency of Ca^{2+} oscillations (Caride et al., 2001). ATP2B1 activity is regulated by the Ca^{2+} signaling protein calmodulin (CaM), which stimulates ATP2B1 activity through its binding to an autoinhibitory domain (Bruce, 2018).

Here, using gene expression analysis, we demonstrate the unbalancing of Ca^{2+} signaling pathways during SARS-CoV-2 infection *in vitro* using human HEK-293T cells overexpressing ACE2 on the plasma membrane (HEK293T-ACE2). This is mostly due to deregulation of ATP2B1 and ATP2A1 (i.e., SERCA1) proteins on the plasma membrane and the endoplasmic reticulum, respectively, thus also clarifying the role of Ca^{2+} in SARS-CoV-2 replication. In this regard, using human primary cells obtained from nasal brushing from a healthy donor, the downregulation of ATP2B1 expression levels promotes SARS-CoV-2 replication, as shown here by increased viral Nucleoprotein (N) levels in infected cells, by augmenting the intracellular Ca^{2+} levels. A model describing this mechanism of action on both *ATP2B1* and *ATP2A1* further describes the action of SARS-CoV-2 (variants of concern [VOCs]: Delta and Omicron 2) during their status of replication and infection. Here, viral entry into the host cells enhances PI3K/Akt signaling pathways, which in turn diminishes the transcriptional nuclear activity of the transcriptional factor FOXO3 by promoting its phosphorylation (Brunet et al., 1999), thus causing a reduction in the transcriptional activation of their target genes, including *ATP2B1* and *ATP2A1*. This, sequentially, causes an increase in the intracellular Ca^{2+} concentration that enhances SARS-CoV-2 replication and propagation. Furthermore, the inactivation of FOXO3 also causes an increase in the NF-κB inflammatory pathway (Thompson et al., 2015), thus further promoting the cytokine storm induced by SARS-CoV-2.

Of importance, using artificial intelligence screening, we identify a new non toxic caloxin-derivative compound (PI-7) that *(i)* inhibits ATP2B1 activity via reduction of extra-intracellular cellular Ca^{2+} levels and *(ii)* enhances *ATP2B1* and *ATP2A1* mRNA and protein levels via FOXO3 transcriptional regulation. Further, compound PI-7 also *(iii)* impairs SARS-CoV-2 (VOCs: Delta and Omicron 2) infection and propagation by negatively affecting the generation of syncytia, and *(iv)* prevents the release of inflammatory cytokines that are targets of NF-κB.

Furthermore, through the search of rare genetic variants associated with severe disease status we identified a rare (0.038187 global frequency) intronic homozygous 'rs11337717' polymorphisim (chr12:89643729, T>C) in *ATP2B1* locus that is positively associated with severity of COVID19.

Altogether, these data identify a new genetic factor that is responsible for severe COVID19 predisposition, and also report the potential use of a new nontoxic molecule in the fight against SARS-CoV-2 infection.

Results

SARS-CoV-2 infection reduces intracellular Ca^{2+} signaling via downregulation of ATP2B1 and ATP2A1

Ca^{2+} homeostasis has been reported to have an important role during SARS-CoV-2 viral infection (Chen et al., 2019; Zhou *et al.*, 2009). Here, to study the physiological response of ATP2B1 to Ca^{2+} oscillations in the presence of SARS-CoV-2, we generated HEK293T cells that stably express its main receptor, ACE2 (i.e., HEK293T-ACE2 cells; Ferrucci et al., 2022). As a control, we used immunoblotting analyses to verify that overexpression of ACE2 does not alter the subcellular localization of the ATP2B1 protein (Figure 1A). These data show the presence of ATP2B1 protein only in the membranes enriched fraction obtained from HEK293T-ACE2 cells (and in their total protein lysates, as the positive control) (Figure 1A).

Then, to have a global picture of the transcriptome landscape in response to the "early phase" of SARS-CoV-2 infection and to confirm the above data of the importance of Ca^{2+} homeostasis in SARS-COV-2 infection, gene expression (i.e., RNAseq) analysis was performed in the HEK293T-ACE2 cellular model upon infection with viral particles belonging to the VOC Delta (multiplicity of infection [MOI]: 0.026) for 24 h (Figure 1B). Viral infection was confirmed through immunoblotting analyses, which showed the presence of the viral N protein in the HEK293T-ACE2–infected cells, in comparison with noninfected cells (Figure 1C). RNAseq analyses revealed downregulation of 1742 and upregulation of 34 gene transcripts in HEK293T-ACE2–infected cells (i.e., differentially expressed genes [DEGs]; Figure S1A).

Gene set enrichment analysis on these DEGs using both SARS-CoV-2–infected and noninfected cells showed downregulation of several signaling pathways, where after 24 h of infection, "Calcium signaling" was in the top 20 list (Figure S1B, Figure 1D, Table S1). Within this gene expression picture, there was downregulation of Ca^{2+} pump gene transcripts, including PMCAs on the cell membrane and SERCAs on the endoplasmic reticulum (Figure 1D).

Epithelial lung cells are the most common target of SARS-CoV-2. Acheampong et al. (Acheampong et al., 2022) used a single-cell RNA sequencing (RNA-seq) approach to show that a substantial number of the plasma membrane Ca^{2+} ATPases (PMCAs or ATP2B; members of the large family of Ca^{2+} ion pumps) are expressed here (Figure S1C). This analysis revealed that *ATP2B1* and *ATP2B4* mRNA expression levels are augmented in multiple cell types in the lung parenchyma (i.e., alveolar cells, including macrophages, and in alveolar epithelial cells type I and type II), in contrast to *ATP2B2* and *ATP2B3* (Figure S1C).

Here, we interrogated publicly available datasets obtained from single-nuclei RNA-seq for >116,000 nuclei sequenced from 19 COVID19 autopsy lungs and seven pre-pandemic controls (Melms et al., 2021) (https://singlecell.broadinstitute.org/single_cell/study/SCP1052/covid-19-lung-autopsy-samples). We found that the ATP2B1-4 (PMCAs) and SERCA pumps (*ATP2A1*-3) showed distinct fractional and dysfunctional changes across the lungs from patients who died with COVID19. Of interest, there were decreased levels of ATP2B1 and ATP2B4 in the lungs of COVID19 patients, while in contrast, the levels of ATP2A2 were increased (Figure S1D). Furthermore, there were undetectable expression levels of ATP2A1, ATP2A3, ATP2B2, and ATP2B3 in the lungs of both COVID19 patients and controls (Figure S1D). These results obtained from COVID19 patients further confirm those obtained from our *in-vitro* RNA-seq analyses, with downregulation of ATP2B4 and increased levels of ATP2A2 upon SARS-CoV-2 infection in these HEK293T-ACE2 cells (Table S1).

Among these Ca^{2+} pumps, we focused on *ATP2B1* because of its pivotal role in the maintenance of Ca^{2+} homeostasis in the cells (Muallem *et al.*, 1988). Using the public single-nuclei RNA-seq data, we show that ATP2B1 was reduced in COVID19 patients (i.e., 0.507 vs 0.513 ATP2B1 expression; Figure S1D-E). However, its expression level was unchanged in the "early phase" of SARS-CoV-2 infection (i.e., after 24 h) in the HEK293T-ACE2 cells (Table S1).

To better dissect out the ATP2B1 expression levels during SARS-CoV-2 infection, we used the HEK293T-ACE2 cell model (Ferrucci *et al.*, 2022). Thus, these cells were infected with viral particles belonging to VOC Delta for 48 h (MOI: 0.026) (Figure 1E). The data obtained from qPCR analyses (using SYBR-green approach) showed upregulated levels of viral N protein genes (as the positive control) and downregulated levels of ATP2B1 in the cells infected for 48 h, in comparison to the noninfected cells (fold: 0.7), thus suggesting that the decrease in ATP2B1 levels is not an "early event" during viral infection (i.e., within 24 h) (Figure 1F).

To better decipher the correlation between ATP2B1 expression levels and SARS-CoV-2 infection, we transiently downregulated ATP2B1 using a siRNA that specifically targets ATP2B1 (see ATP2B4 as control in Figure S2A-B), with a control of target specificity using an unrelated ATP2B1 siRNA sequence. In the same cellular model (i.e., HEK293T-ACE2 cells), after 12 h of transfection with siRNA, the cells were infected with viral particles belonging to VOC Delta (MOI: 0.026), for additional 60 h (Figure 1G). Immunoblotting analyses confirmed increased levels of the viral N protein in cells silenced for ATP2B1 (Figure 1H), thus indicating that reduced levels of ATP2B1 fosters SARS-CoV-2 replication.

Altogether, these data indicate that SARS-CoV-2 infection decreases the Ca^{2+} signaling pathways mainly due to downregulation of Ca^{2+} pumps on the cell membranes (i.e., ATP2B1). Of interest, decreased levels of ATP2B1 are also found in lungs from COVID19 patients (Figure S1D-E). Furthemore, reduced amounts of ATP2B1 during SARS-CoV-2 infection are shown to increase viral replication *in vitro* using the HEK293T-ACE2 cells (Figure 1F, H).

Reduced ATP2B1 levels increase SARS-CoV-2 replication in human primary epithelial nasal cells

Here, the aim was to better dissect out any correlations between ATP2B1 expression, the intracellular Ca^{2+} pool, and the replication of SARS-CoV-2, through measurement of the intracellular Ca^{2+} levels upon overexpression or downregulation of *ATP2B1* in human primary epithelial cells obtained by nasal brushing from healthy donors (Ferrucci et al., 2021). This cellular model has been previously described (Ferrucci *et al.*, 2021) and sequenced using whole exome sequence technology (EVA - EMBL-EBI; project ID: PRJEB42411; analyses: ERZ1700617). To this end, we transiently downregulated *ATP2B1* using siRNA approach (Figure S2A-B) in human primary epithelial nasal cells, with immunoblotting analyses performed 48 h after transfection was started. This showed a downregolution of *ATP2B1* expression (Fold 0.4) (Figure 2A). In contrast, ATP2B1-overexpressing cells (Fold 1.5) augment of 50% the expression of *ATP2B1* (Figure 2A).

We then measured the intracellular Ca^{2+} levels using the Fluo3-AM substrate (as described in Star-Methods). These data showed decreased intracellular Ca^{2+} levels in ATP2B1-overexpressing human primary epithelial nasal cells (recorded for up to 72 min; Figure 2B). In contrast, the downregulation of *ATP2B1* in the same cells did not change the intracellular Ca^{2+} levels (Figure 2C). At this time, we cannot exclude that the downregulation of *ATP2B1* can be compensated by a transcriptional activation and protein synthesis of other paralog gene transcripts, which could consequentially regulate Ca^{2+} signaling. Further studies will clarify the other mechanisms responsible for Ca^{2+} homeostasis beyond *ATP2B1* downregulation.

The opposite trend between SARS-CoV-2 infection and ATP2B1 levels was then also investigated in this cellular model (i.e., human primary epithelial nasal cells). To this aim, human primary epithelial nasal cells were infected with SARS-CoV-2 viral particles belonging to VOC Delta for 72 h at 0.026 MOI, with noninfected cells used as the negative control (Figure

2D). Immunoblotting analyses showed increased viral N protein levels upon SARS-CoV-2 infection (72 h; fold: 1.5) and reduced protein levels of ATP2B1 (fold: 0.7; Figure 2E). Taken together, these data validate the opposite trend between viral infection and ATP2B1 expression at the protein level in this other cellular model. Overall, the data suggest that SARS-CoV-2 infection requires *ATP2B1* downregulation for its propagation also in the airway epithelium (Figure 2F).

ATP2B1 **intronic polymorphism influences susceptibility for severe COVID19**

As ATP2B1 has been shown to be downregulated in the lungs of COVID19 patients and here in our *in-vitro* infected cellular models (Figure S1D-E; Figure 1F), we evaluated potential genetics associations between ATP2B1 locus and the risk of developing severe COVID19. To select potential disease causative variants, we downloaded 351 coding variants of *ATP2B1* from "The Genome Aggregation Database" (GnomAD v2.1), where 13 were pathogenic according to their "Functional Analysis through Hidden Markov Models" (FATHMM) prediction scores (Table S2). However, these variants were extremely rare and were thus excluded from further investigations. The results indicate that loss of function mutations of *ATP2B1* are rare (observed/expected score = 0.08; data from GnomAD v2.1) and we postulate the hypothesis that the *ATP2B1* gene is essential for the physiological action within the cell. Further, no pathogenetic nucleotide variations within the coding protein region of ATP2B1 can be allowed for the cell to survive.

Thus, a second analysis was performed to verify the presence of noncoding variants in the genomic region of the *ATP2B1* locus that act as "expression quantitative traits loci" (eQTLs). We used an analytic approach to select candidate functional noncoding variants single nucleotide polymorphisms (SNPs; Table S3). We first selected 76 SNPs that were eQTLs for the *ATP2B1* gene ($P<1 \times 10^{-6}$) using the "Genotype-Tissue Expression" (GTex) database (Table S4). These SNPs were then annotated with prediction functional scores calculated using the "Genome-Wide Annotation of Variants" (GWAVA) tool (Table S4), and the top six SNPs were selected: rs11105352, rs11105353, rs10777221, rs73437358, rs111337717, and rs2681492. At this time we excluded rs10777221 (the most 5' region in the extragenic region) of the *ATP2B1* locus (Figure S3A). Linkage disequilibrium (LD) analyses on the remaining SNPs showed that the only variant that is not in linkage disequilibrium was rs111337717 (Figure S3B; Figure 3A). This, thus, further indicated that this SNP deserved further analyses as a good candidate for searching for associations to COVID19 severe and asymtomatic patients.

To this end, we tested these SNPs in a cohort of 197 patients affected by severe COVID19 and 370 asymptomatic cases (D'Alterio et al., 2022). Here, the minor allele “C” of the rs111337717 (NC_000012.12:g.89643729T>C) SNP [(CACATG(T/C)ACATTAT)] was significantly more frequent among severe COVID19 cases, when compared with asymptomatic individuals (p=0.0004; Table 1), thus suggesting that rs111337717 can be listed among the genetic risk factors for predisposition to severe COVID19. Of note, alignament sequence analyses of the genomic region flanking rs111337717 [(CACATG(T/C)ACATTAT)] showed high homology identity across different species (Figure 3B), thus suggesting a potential significant and conserved role during evolution. How this intron SNP variant influences SARS-CoV-2 infection and propagation will be an issue for future studies.

ATP2B1 and *ATP2A1* are transcriptionally regulated by FOXO3 transcription factor

To determine how the locus is transcriptionally regulated, we used recent literature data showing forkhead box O (FOXO) transcription factors as strong candidates for antiviral responses against SARS-CoV-2. Their transcriptional mechanism is under epigenetic control, which in turn regulates anti-apoptotic and anti-inflammatory pathways, also acting as negative regulators of NF-κB inflammatory signaling (i.e., FOXO3) (Cheema et al., 2021).

To this end, we performed *in-silico* analysis of publicly available datasets of single-cell RNA sequencing from 19 COVID19 autopsy lungs and 7 pre-pandemic controls (Melms *et al.*, 2021); https://singlecell.broadinstitute.org/single_cell/study/SCP1052/covid-19-lung-autopsy-samples). These analyses were performed to define the potential differential expression of FOXOs transcription factors in COVID19 patients. These data showed higher expression levels in the lung of FOXJ3, FOXK2, FOXN3, FOXO1, FOXO3, and FOXP1 (Figure 3C). Among these, the expression levels of FOXK2, FOXO3, and FOXP1 were lower in the lungs from COVID19 patients, compared to controls (Figure 3C), thus showing the same expression levels and trends as observed for ATP2B1 (Figure S1D-E).

The epigenetic changes regulating chromatin structure have been previously implicated in the pathophysiology of SARS-CoV-2 infection (Chlamydas et al., 2021), and, among the epigenetic drugs, the histone deacetylase inhibitor valproic acid (VPA) has been suggested to protect against the development of severe COVID19 (Collazos et al., 2022; Pitt et al., 2021). For the above reason, we have here verified which FOXO transcription factor (whose expression was found downregulated in COVID19 patients, see Figure 3C) was restored following VPA treatment. We treated HEK293T-ACE2 cells with 20 mM VPA for 16 h to investigate whether FOXO-related genes are regulated. Of note, both HEK293T-ACE2 cells and human epithelial primary nasopharyngeal cells are not characterized by SNPs in the region of the *ATP2B1* locus, as described previously (Figure S3C-D). Our qPCR data showed increased expression of FOXO3 in VPA-treated cells, compared to the vehicle control (Fold: 4.38; see Figure S3E). In contrast, the levels of *FOXK2* and *FOXP1* mRNAs were both decreased upon VPA treatment (Fold: *FOXK2*, 0.44; *FOXP1*, 0.65; see Figure S3E). Furthermore, FOXO3 also shows the same expression trend as ATP2B1, with reduced expression levels in the lung of COVID19 patients (ATP2B1, Figure S1E; FOXO3, Figure S3F).

Thus, we hypothesized that FOXO3 is a candidate transcription factor that can control ATP2B1 expression. We then used genome views of *FOXO3* ChIP-Seq signals over the *ATP2B1* locus using publicly deposited data (Figure 3D). The normalized *FOXO3* signals were visualized with the UCSC genome browser, together with layered CromHMM and H3K4me3 ENCONDE tracks, respectively. The results here indicate that FOXO3 peaks show preferential binding at the promoter and enhancer regions of both the *ATP2B1* (Figure 3D), thus indicating the potential positive transcriptional regulator activity of FOXO3.

Thus, to verify whether FOXO3 and ATP2B1 have the same downregulation trend upon SARS-CoV-2 infection *in vitro*, we infected the HEK293T-ACE2 cells with viral particles of VOC Delta (MOI 0.026) for 72 h. The immunoblotting data showed downregulated levels of ATP2B1 and FOXO3 in SARS-CoV-2 infected cells, with increased levels of phosphorylated (S253)-FOXO3 (Figure 3E). These results thus indicate increased levels of the cytosolic inactive phosphorylated-FOXO3 protein, and a reduction in the total FOXO3 and ATP2B1 protein levels following SARS-CoV-2 infection. Of interest, our data also show decreased levels of ATP2A1 upon SARS-CoV-2 infection (Figure 3E). The expression of ATP2A1 has been previously shown to be reduced upon SARS-CoV-2 infection (Figure 1D, Table S1). Of interest, the genome view of FOXO3 ChIP-Seq signals over the *ATP2A1* locus indicated that FOXO3 peaks also showed binding at the promoter region of *ATP2A1* (Figure S3G), thus indicating a potential activity of FOXO3 as a transcriptional regulator of both the *ATP2B1* and *ATP2A1* loci.

The phosphorylation of FOXO3 has been previously shown to be mainly triggered by PI3K/Akt pathway activation, which results in its exclusion from the nucleus and inhibition of the transcriptional activation of its target genes (Brunet *et al.*, 1999; Manning and Cantley, 2007; Stefanetti et al., 2018). Thus, we further investigated the phosphorylation of Akt in the same cells infected with SARS-CoV-2. As expected, we confirmed the literature data showing increased levels of phosphorylated(S473)-Akt also in this *in-vitro* model (i.e., HEK293T-ACE2 cells) upon SARS-CoV-2 infection (Khezri et al., 2022) (Figure 3E).

Then, in order to validate the role of FOXO3 as a positive transcriptional regulator of *ATP2B1* and *ATP2A1*, we transiently overexpressed a FOXO3-encoding plasmid (containing the coding region of FOXO3; #14937, Addgene) in HEK293T-ACE2 cells. After 48 h from the start of transfection, immunoblotting data showed increased levels of both the FOXO3, ATP2B1 and ATP2A1 proteins (Figure 3F), thus suggesting that FOXO3 is a positive regulator of the *ATP2B1* and *ATP2A1* loci. These data confirm our hypothesis that FOXO3 is a good candidate to transcriptionally activate both membrane (i.e., ATP2B1) and endoplasmic reticulum (i.e., ATP2A1) Ca^{2+} pump expression.

Altogether, these data indicate that following SARS-CoV-2 infection, the activation of the PI3K/Akt pathway increases the levels of phosphorylated-FOXO3, thus causing its exclusion of FOXO3 from the nucleus, and, as a consequence, the inhibition of their target genes transcription, including the newly identified *ATP2B1* and *ATP2A1*. This mechanism leads to downregulation of ATP2B1 on plasma membranes and ATP2A1 on endoplasmic reticulum, thus increasing the intracellular Ca^{2+} levels, which enhances SARS-CoV-2 replication, as shown in the model presented in Figure 3G.

Identification of an ATP2B1 targeting molecule that impairs SARS-CoV-2 infection and replication

To identify novel candidate compounds in the fight against SARS-CoV-2, we used artificial intelligence as a drug design computational tool to model the structure of ATP2B1 (PMCA1)–caloxin 2a1 (as a known ATP2B1 inhibitor; Pande et al., 2011) by docking and energy minimization modeling (Chaudhary et al., 2001) (Figure S4A). Thus, a pharmacophore model was built using the structures that we assumed for ATP2B1–exodom-2 and caloxin 2a1 (Figure S4A). Five pharmacophore features were produced. Among 230 million screened compounds, we selected 30 million by considering database filtering for solubility and absorption, 7,201 molecules by pharmacophore searches, and 1,028 molecules by docking scoring (Figure S4B). We then manually selected the top 22 molecules. Finally, two compounds (PI-7 and PI-8; Figure 4A, B) were identified and selected for further functional assays.

We first assessed the cytotoxicity of these two compounds (PI-7 and PI-8) in terms of cell proliferation and apoptosis in HEK293T-ACE2 cells. The cell proliferation assay (based on the measurement of electrical impedance in real-time; i.e., cells index) was used to determine the half-maximal inhibitory concentrations (i.e., IC_{50}) of PI-7 and PI-8. To this aim, we tested escalating doses (from 200 μM to 1200 μM) of PI-7 and PI-8 on HEK293T-ACE2 cells, and calculated the IC_{50} 48 h after the treatment started (IC_{50} values: PI-7, 580 μM, R^2 0.9; PI-8, 336 μM, R^2 0.9; Figure 4C-D and Figure S4C-D). Of interest, the lower doses of PI-7 and PI-8 (0.1-10 μM) did not alter the cell proliferation rates, as compared to vehicle-treated cells (vehicle: 0.001% dimethylsulfoxide [DMSO]) (Figure S4C-D). Similar results were obtained for apoptosis assays. Here, no activation of caspase 3 activity was shown in the HEK293T-ACE2 cells upon treatment with escalating doses of PI-7 and PI-8 (from 1 to 100 μM; Figure S5A). These data were further validated by immunoblotting analyses performed on the same treated cells with antibodies against the cleaved fragment of caspase 3 (i.e., activated caspase 3; Figure S5B, C). Altogether, these *in-vitro* data exclude anti-proliferative and pro-apoptotic actions of both PI-7 and PI-8 compounds.

Since an interplay between the Ca^{2+} homeostasis (regulated by ATPase 2B Ca^{2+} family pumps) and glucose metabolism has been since described (Dejos et al., 2020), we measured both the extracellular and intracellular Ca^{2+} level in human primary epithelial nasal cells in high (+) and low (-) glucose conditions. The data show that both extracellular and intracellular Ca^{2+} content are higher in those cells cultured in low (-) glucose conditions thus confirming literature data (Figure S5D-E on the left).

Thus, we evaluated the efficacy of both compounds PI-7 and PI-8 on *ATP2B1* pump inhibition in primary human epithelial nasal cells grown in media containing high (+) glucose and low (-) glucose content (see Figure 4E, F: red box, high (+) glucose; green box, low (-) glucose). The results indicate that both compounds (i.e., PI-7 and PI-8) reduced the extracellular Ca^{2+} content as compared to vehicle control (i.e., 0.001% DMSO) (Figure 4E, Figure S5D; high (+) glucose condition: PI-7, 0.79 fold lower [21% inhibition]; PI-8, 0.83 fold lower [17% inhibition]; low (-) glucose condition: PI-7, 0.88 fold lower [12 % inhibition]; PI-8, 0.92 fold lower [8% inhibition]). A similar trend was observed for the inhibition of the intracellular cytosolic Ca^{2+} content (Figure 4F, Figure S5E; high (+) glucose condition: PI-7, 0.82 fold lower [18% inhibition]; PI-8, 0.76 fold lower [24% inhibition]; low (-) glucose condition: PI-7, 0.69 fold lower [31% inhibition]; PI-8, 0.86 fold lower [14% inhibition]).

Taken altogether, the data show that compound PI-7 has a better performance in both extracellular and intracellular Ca^{2+} inhibition in low (-) glucose condition. This latest condition is responsible for increased intracellular and extracellular Ca^{2+} levels (Figure S5D-E on the left) that are both required for SARS-CoV-2 infection and replication.

For the above reasons, we focused on compound PI-7 for the following experiments. To dissect the intracellular alterations due to treatment with PI-7, we performed a proteomic analysis in the HEK293T-ACE2 cells upon treatment with 1 μM PI-7 for 24 h (Figure S6A). In the treated cells, there were 17 downregulated and 66 upregulated proteins (Table S5). We then generated a network of protein interactions through the "Search Tool for Retrieval of Interacting Genes/Proteins" (STRING) database, with both the upregulated and downregulated (Figure S6A) proteins. This showed that the upregulated proteins take part in the common networks mostly involved in the regulation of metabolic processes and gene expression (Figure S6A, Table S6). Of importance, among the down-regulated proteins, we found some that are involved in viral transcription and viral processes (Figure S6A in bold, Table S7).

To dissect out the potential antiviral activity of compound PI-7, we treated HEK193T-ACE2 cells with 1 μM PI-7 and then infected them with SARS-CoV-2 (VOC Delta) at 0.026 MOI for 72 h (Figure 5A). Immunoblotting data show that PI-7 decreased the viral N protein levels, thus demonstrating inhibition of viral replication (Figure 5B). Of note, the data also showed increased ATP2B1 and ATP2A1 protein levels in PI-7-treated and infected cells, as compared to vehicle control (Figure 5B). The overexpression of ATP2B1 was found to decrease the intracellular Ca^{2+} levels (Figure 2B) and the treatment with compound PI-7 was shown to diminish both the extracellular and intracellular Ca^{2+} levels (Figure 4E-F). Our data are here suggesting that compound PI-7 exerts antiviral activity by decreasing the extracellular and intracellular Ca^{2+} levels, also by potentially promoting its uptake into the endoplasmic reticulum) mostly due to inhibition of ATP2B1 activity and upregulation of ATP2A1.

Then, because of the positive transcriptional regulation of *ATP2B1* and *ATP2A1* mediated by FOXO3 (Figure 3F), we also verified its protein levels upon treatment with compound PI-7 in the same infected cells. These data show an increased level of total unphosphorylated (transcriptionally active) FOXO3 protein amount, and decreased levels of inactive phosphorylated (S253)-FOXO3 (Figure 5B). Thus, the enhanced transcriptional activity of unphosphorylated FOXO3, due to PI-7 treatment, would also explain why *ATP2B1* protein amount is found upregulated in the treated cells (Figure 5B).

Furthermore, because the phosphorylation of FOXO3, and its exclusion from nucleus, had been previously shown to be triggered by PI3K/Akt pathway activation (Brunet *et al.*, 1999; Manning and Cantley, 2007; Stefanetti *et al.*, 2018) also during SARS-CoV-2 infection (Figure 3E), we further investigated the phosphorylation status of Akt in those cells infected with SARS-CoV-2. As expected, our data confirmed a decrease amount of phosphorylated

(S473)-AKT upon compound PI-7 treatment (Figure 5B), thus further confirming the antiviral action of this molecule against SARS-CoV-2 infection.

Altogether, compounds PI-7 inhibits AKT signaling that in turn lowers the phosphorylation of FOXO3 (on Serine 253), thus resulting in increased levels of transcriptionally active (unphosphorylated) FOXO3 that modulates the expression of its target at nuclear levels, including the transcriptional activation of *ATP2B1* and *ATP2A1* (Figure 5B). Dissecting further how AKT/FOXO3 phosphorylation mechanism of action is occurring during SARS-CoV-2 infection will be an issue of future studies.

Of interest, FoxO transcriptional factors have already been shown to have a role in immune cell maturation and inflammatory cytokines secretion (Cheema *et al.*, 2021). Among the FoxOs, FoxO3 has already been shown to modulate innate immune responses to infections of the airway epithelium through modulation of secretion of several cytokines from immune cells (Xin et al., 2018). This occurs through inhibition of the NF-κB inflammatory pathway, the activation of which is exploited by the SARS-CoV-2 (Thompson *et al.*, 2015). Thus, restoring the transcriptional activity of FoxO3 might relieve the inflammatory burst following SARS-CoV-2 infection.

To test this hypothesis, we investigated NF-κB inflammatory pathway through immunoblotting in the same PI-7-treated and infected cells. Our data show decreased levels of phosphorylated (Ser311)-p65 in PI-7-treated cells, as compared to the vehicle control (Figure 5B). Furthermore, in order to exclude that NF-κB inhibition is only a consequence of a reduced viral infection in these SARS-CoV-2-infected cells previously treated with compound PI-7, we have also tested the phosphorylation of p65 in non-infected human primary nasal cells treated with compound PI-7 for 24 hours (Figure S6B). Our data show decreased levels of phosphorylated (Ser311)-p65 in PI-7-treated cells in absence of SARS-CoV-2 (Figure S6B), thus showing the efficacy of compound PI-7 to impair NF-κB inflammatory pathway. To further confirm, the anti-inflammatory action of this molecule in HEK-293T-ACE2 cells upon SARS-CoV-2 infection, we measured the expression levels of some of the main cytokines targeted by NF-κB that take part in the COVID19 cytokine storm (Hu et al., 2021; Rabaan et al., 2021) (i.e., IL-1β, IL-6, and TNF-α). Our qPCR data showed a statistically significant reduction in the levels of these cytokines in PI-7-treated cells, as compared to the vehicle controls (Figure S6C).

Altogether, these results show the ability of compound PI-7 to (i) reduce phosphorylated (S473)-AKT and phosphorylated (S253)-FOXO3 and (ii) increase unphosphorylated active

FOXO3 protein levels as a result of reduced viral replication in HEK293T-ACE2 cells upon infection by SARS-CoV-2 (VOC Delta, 72 h) (Figure 5B). As a consequence, this leads to impairment of the NF-κB inflammatory pathway (also mediated by activation of FOXO3) and inhibition of cytokine expression upon treatment with compound PI-7 (Figure 5B, Figure S6C). Overall this data show an anti-inflammatory property of compound PI-7 by reducing phosphorylated (S473)-AKT and phosphorylated (S253)-FOXO3 phosphorylations. When this action is taking part in infected SARS-CoV-2 cells will be issue of future investigations.

Of interest, the treatment with compound PI-7 not only restored *ATP2B1 and ATP2A1* protein amounts, but also increased their transcritpional levels, mostly as a consequence of FOXO3 transcriptional activity (Figure 5C).

As Ca^{2+} transition had been previously reported to be correlated to the endoplasmic reticulum stress(Deniaud et al., 2008), we validated our qPCR data on ATP2A1 levels through the levels of endoplasmic reticulum stress. To this aim, high-resolution immunofluorescence analyses were performed using the lattice SIM^2 technology (ELYRA7, ZEISS), which showed increased levels of GRP78, as a marker of endoplasmic reticulum stress, in the SARS-CoV-2–infected HEK293T-ACE2 cells upon treatment with compound PI-7, in comparison with vehicle-treated cells (Figure 5D). These results suggested that treatment with PI-7 decreases intracellular Ca^{2+} levels also by restoring the expression of *ATP2A1* (whose levels were decreased in the presence of SARS-CoV-2, Figure 1D) that is involved in the translocation of Ca^{2+} from the cytosol to the sarcoplasmic reticulum lumen (Minton, 2014).

Taking all together, compound PI-7 is able to impair *ATP2B1* pump activity in terms of extracellular and intracellular Ca^{2+} decrease during SARS-CoV-2 infection, potentially because of the PI3K/AKT pathway inhibition, reduction of phosphorylation of FOXO3 and enhanced expression of *ATP2B1* (that is responsible for decreased levels of intracellular Ca2+, see Figure 2B) and *ATP2A1* (that promotes Ca^{2+} uptake into the endoplasmic reticulum, thus causing reticulum stress, see Figure 5D). A more comprehensive action at the transcriptional level of compound PI-7 will be further detailed in the near future.

As many enveloped viruses (including SARS-CoV-2) have been shown to cause fusion of the neighboring cells into multinucleated 'syncytia' (Braga et al., 2021), we further investigated here the antiviral activity of compound PI-7 on inhibition of syncytia generation. Thus, to determine the relative proportions of syncytia, the same HEK293T-ACE2 cells were treated with PI-7 (1 μM) or vehicle (0.001% DMSO), infected with SARS-CoV-2, and fixed for immunofluorescence analyses using an antibody against the ACE2 protein (Figure 5E). We found decreased syncytia percentages in the cells upon treatment with PI-7 (P=7.9E-5) (Figure 5E). As a further control, lower expression levels of the "syncytia marker" TMEM16 (Braga *et al.*, 2021) were found in PI-7-treated HEK293T-ACE2 cells upon SARS-CoV-2 infection, (fold: 0.6, see Figure S6D).

Altogether, these data indicate the anti-viral activity of compound PI-7 against SARS-CoV-2 infection in these HEK293T-ACE2 cells, with decreased levels of the viral N protein and lowered levels of syncytia formation.

The anti-inflammatory actions of compound PI-7 via FOXO3–NF-κB block the COVID19 cytokine storm against Omicron 2 variant

Finally, the antiviral activity of compound PI-7 was validated in human primary epithelial nasal cells infected with the latest SARS-CoV-2 variant (VOC: Omicron 2) at 0.04 MOI for 70 hours of infection (Figure 6A). Our qPCR analyses supported the antiviral activity of PI-7 also against the Omicron 2 SARS-CoV-2 variant, with a reduction in the viral N protein levels, the expression of which was increased in these infected cells (Figure 6B). Furthermore, the data show that PI-7 can restore the expression levels of the calcium pumps (i.e., ATP2B1, ATP2A1) and can also reduce the NF-κB–induced cytokines (i.e., IL-1β, IL-6, TNF-α) in these cells infected with the Omicron 2 SARS-CoV-2 variant (Figure 6B).

Overall, these data show the efficacy of compound PI-7 against SARS-CoV-2 VOC Omicron 2 via targeting inflammatory pathways in coordination of Ca^{2+} signaling.

Discussion

Ca^{2+} as an important second messenger in excitable and non-excitable cells, where it controls essential functions including cellular signaling processes and immune responses(Brini et al., 2013). Intracellular and organellar Ca^{2+} concentrations are tightly controlled via various pumps, ATPases, ion channels, and uniporters. Among these pumps, PMCAs and SERCAs are considered an efficient line of defense against abnormal Ca^{2+} rises. During viral infection, cellular Ca^{2+} dynamics are highly affected, as dysregulation of the host cell signaling cascades is elicited by these infectious agents (Berlansky *et al.*, 2022).

Two mechanisms of regulation of Ca^{2+} can be envisioned upon SARS-Cov-2 infection: one related to the extracellular virus-host interaction, and the other linked to an intracellular mode of action once the virus has entered the cell. The presence of extracellular Ca^{2+} can positively influence virus-host interactions for the correct binding of CoVs to the ACE2 receptor and during membrane fusion when the virus is entering the cell(Shang et al., 2020). Intracellular Ca^{2+} has been reported to enhance SARS-CoV-2 replication by activating downstream processes, such as alteration of the host cellular metabolism and acceleration of inflammation (Serebrovska et al., 2020).

Here, we focused on understanding how intracellular Ca^{2+} modulation can influence SARS-CoV-2 infection and replication. Gene expression data obtained using HEK293T-ACE2 cells infected with SARS-CoV-2 showed downregulation of Ca^{2+} signaling pathways, mostly mediated by decreased levels of the PMCA and SERCA Ca^{2+} pumps. This thus suggests increased levels of intracellular Ca^{2+} defined by indirect, but positive, evidence (gene expression data), as almost all of the Ca^{2+} pumps were downregulated (Figure 1D in blue and Table S1). Then in the additional validation studies we focused on ATP2B1, showing a time-dependent decrease in expression in response to SARS-CoV-2 infection. Furthermore, an opposite correlation was seen between viral replication (as shown by the viral N protein levels; and ATP2B1 levels of expression in the two different cellular models (i.e., HEK293T-ACE2 cells [see Figure 1F, H] and human primary epithelial nasal cells [Figure 2E]). At this time we envision future studies to investigate the responses to other Ca^{2+} pumps on the endoplasmic reticulum, mitochondria, and Golgi complex following SARS-CoV-2 infection, to dissect out further its mechanism of action.

Of interest, using a new caloxin-derivative molecule (i.e., compound PI-7), we show decreased intracellular Ca^{2+} levels (mimicking ATP2B1 overexpression in human primary epithelial nasal cells) and also extracellular Ca^{2+} content. Whether the addition of PI-7 results in binding and blocking of ATP2B1 pump to decrease the exports of Ca^{2+} into the extracellular environment will be the aim of future deep investigations, potentially through structural conformational studies and protein–drug crystallography. Here we hypothesized a secondary mechanism of control of expression of ATP2B1 and other Ca^{2+} pumps to maintain protein expression by juxtaposing compound PI-7 action and by controlling the intracellular and extracellular Ca^{2+} signaling.

Of importance, prophylactic treatment of HEK293T-ACE2 cells before SARS-CoV-2 infection (VOCs Delta and Omicron 2) exerts antiviral actions on viral replication (as measured by decreased viral N protein levels). The results showing decreased syncytia formation in the PI-7-treated cells, compared to vehicle controls, provide further support here (see Figure 5E). This is a result of impairment of the generation of syncytia activation by the SARS-CoV-2 Spike protein at the level of the cell plasma membrane. Furthermore, Ca^{2+} is known to be of importance for syncytia generation; indeed, drugs that inhibit TMEM16 activity (a Ca^{2+}-

activated ion channel; e.g., niclosamide) blunted Ca^{2+} oscillations in Spike-expressing cells, and as a consequence, inhibited Spike-driven syncytia formation (Braga *et al.*, 2021). The expression of TMEM16 in our assays further confirmed these results (see Figure 5E and S6D). Of importance, our data also show restoration of ATP2A1 (ATPase sarcoplasmic/endoplasmic reticulum Ca^{2+} transporting 1; SERCA1) (see Figure 5B, C). Results supporting this hypothesis are also presented in a model upon compound PI-7 treatment of SARS-Cov-2 infection (Figure 6C).

Overall, our data indicate that upon SARS-CoV-2 infection there is downregulation of Ca^{2+} pumps on the cell membrane (ATP2B1) and the endoplasmic reticulum (ATP2A1) due to a further mechanism of action responsible for increased intracellular Ca^{2+} levels during viral infection and replication. How and when Ca^{2+} can pass between the endoplasmic reticulum, cytoplasm, and plasma membrane during SARS-CoV-2 replication are questions to address in the near future.

One of the mechanisms responsible for reduction of expression of ATP2B1 and ATP2A1 during SARS-CoV-2 infection involves the FOXO3 transcription factor and its functional regulation. Our study also demonstrates positive regulation of the *ATP2B1* and *ATP2A1* locus by FOXO3. Of interest, during SARS-CoV-2 infection, we observed increased levels of inactive phosphorylated-(Ser253)-FOXO3 and a substantial reduction in its total protein content under these specific cellular conditions (see Figure 3E). The phosphorylation of FOXO3 has been previously shown to be triggered by the PI3K/Akt pathway, thus causing its exclusion from the nucleus and inhibiting the transcriptional activation of its target genes (Brunet *et al.*, 1999; Manning and Cantley, 2007; Stefanetti *et al.*, 2018), including the newly identified target here (ATP2B1 and ATP2A1). Of note, over-activation of PI3K/Akt pathway during SARS-CoV-2 infection has also been reported (Khezri *et al.*, 2022), and is here confirmed in our *in-vitro* model.

Thus, we hypothesized that one of the mechanisms responsible for the increased FOXO3 phosphorylation that inactivates the transcriptional regulation function of FOXO3 will accordingly decrease ATP2B1 and ATP2A1 levels during SARS-CoV-2 infection. Of interest, activated Akt is also required for intracellular Ca^{2+} release during other viral infections (e.g., Herpes simplex virus; Cheshenko et al., 2013). Thus, taken together, activation of ATP2B1 and ATP2A1 by FOXO3 is a mechanism of escape from virus replication of infected cells, with ATP2B1 being both responsible for the pumping of Ca^{2+} from the cytoplasm (and consequently out of the cells) together with the action of ATP2A1, which stores the cytoplasmic Ca^{2+} in the endoplasmic reticulum. Together, these two controlled mechanisms of action will impair viral replication. Future studies will further investigate the link between PI3K/Akt and the intracellular Ca^{2+} release during SARS-Cov-2 infection (see model presented in Figure 6C).

Of importance, in a cohort of infected symptomatic patients (n. 197 patients affected by severe COVID19 and 370 asymptomatic cases), we identified a rare homozygous intron variant in the *ATP2B1* locus as a novel genetic factor responsible for severe COVID19 predisposition (Table 1). It remains to be identified how the nucleotide region that contains the polymorphism (i.e., rs111337717) can act as a modulator (enhancer or inhibitor). According to our model, we postulate the presence of this SNP variant would influence negatively on the regulation of the ATP2B1 locus and its expression. Future experiments need to be demonstrated to address this hypothesis.

To date, variants in the *ATP2A1* genes that are responsible for COVID19 predisposition have not been reported. The data presented here underline the marker identification to stratify those people who retain the C/C variant in ATP2B1 (rs111337717), as they might be subjected to severe COVID19 following virus infection and replication (see Table 1).

As summarized in (Figure S4 and S5), compound PI-7 was tested here at nontoxic concentrations (i.e., 1 μM), in terms of cell proliferation and apoptosis. It has the potential to reduce the intracellular Ca^{2+} levels (Figure 4E-F) that are necessary for SARS-CoV-2 replication and propagation, as measured by the reduced levels of the viral N protein (see Figure 5B) (the activity of which is essential for genome/ subgenome transcription and maturation of newly formed virions) and reduced numbers of syncytia (Figure 5E).

Finally, the literature data show negative cross-talk between FOXO3 and the NF-κB inflammatory pathway (Thompson *et al.*, 2015), which allowed us to visualize the anti-inflammatory actions of PI-7 in SARS-CoV-2–infected human cells. Treatment with compound PI-7 increased FOXO3 protein levels, and definitively reduced the activation of NF-κB, thus further diminishing the levels of inflammatory cytokines with a known role in the cytokine storm in COVID19 patients (see Figure 6C and Figure S6C). We thus envision compound PI-7 in preventive nd therapeutic manner, and with this anti-inflammatory action could prevent the cytokine storm during SARS-CoV-2 infection. At this time, it remains to investigate whether additional NPRL3 inflammasome signaling is further affected (Lee et al., 2012; Nieto-Torres et al., 2015). However, how an increase in cytosolic Ca^{2+} promotes NLRP3 inflammasome activation is not yet clear. It has been proposed that an increase in cytosolic Ca^{2+} causes Ca^{2+} overloading of the mitochondria, resulting in mitochondrial dysfunction, and thus leading to NLRP3 inflammasome activation. Moreover, the Golgi complex has a key role as an intracellular Ca^{2+} store, in synergy with the endoplasmic reticulum. Regulation of the NLPR3 inflammasome by compound PI-7 is today unclear or uninvestigated and will be an issue of future studies.

Thus, considering the ubiquitous action of compound PI-7 on the mechanism of regulation of the virus machinery that influences both virus replication and propagation during the early status of infection, we envision its use in preventive therapeutic strategies to fight the COVID19 pandemia. As compound PI-7 affects Ca^{2+} cellular homeostasis and the expression of both membrane ATP2B1 and endoplasmic reticulum specific ATP2A1 Ca^{2+}-dependent cellular pumps, and most importantly, as it has anti-inflammation properties with downregulation of the pro-inflammatory function of NF-κB, we envision here that infection by any emerging SARS-CoV-2 variants (e.g., VOC Delta and Omicron 2) will also be inhibited. Indeed, both SARS-Cov-2 Delta and Omicron 2 showed inhibition here and impairment of the most related cytokines of the early storm (see Figure 6B and S6C). Finally, knowing the impaired PI3K/Akt signaling of phosphorylation by compound PI-7, we predict here its application in cancer, in those tumors where such enhanced signalings is evident and pronounced. It is not a surprise that an anti-COVID19 drug can provide benefits in the fight against cancer, and we foresee its use in fragile or cancer-affected patients with poor innate and adaptive immunity (Hosseini et al., 2020; Schultze and Aschenbrenner, 2021; Sette and Crotty, 2021). In light of the determining effect of Ca^{2+} signaling in viral infection and replication and in the immune response, we used the alternative approach of molecular docking to screen for compounds that target the host machinery hijacked by the virus during infection. This approach represents a promising therapeutic strategy that instead of looking for the development of antiviral therapeutic molecules that target viral proteins, looks directly at the host Ca^{2+} channels, resulting in broad applicability.

However, progress to bring such drugs to the clinic faces important challenges. There are three main reasons for hesitation. First, Ca^{2+} signaling might affect several biological pathways. Indeed, side effects might be observed in patients treated with these types of drugs. Secondly, genetic loss-of-function studies in mice and in cells suggest incorrect regulation of the inflammatory responses caused by global Ca^{2+} misregulation. Thirdly, and more critically, animal studies with these small molecules to sustain ATP2B1 expression have to confirm the absence of risk of overt adverse effects. At this time, the mechanism of action and compound PI-7 represent additional weapons to impair further waves of infections by COVID19, as new variants are now expected.

ETHICAL COMMITTEE APPROVAL

The Ethical Committee approvals for the COVID19 samples use in this study were as follows: (i) protocol no. 141/20; date: 10 April 2020, CEINGE TaskForce Covid19; Azienda Ospedaliera Universitaria Federico II, Direzione Sanitaria, protocol no. 000576 of 10 April 2020; (ii) protocol no. 157/20; date: 22 April 2020, GENECOVID, with the experimental procedures for the use of SAR-CoV-2 in a biosafety level 3 (BSL3) laboratory were authorized by Ministero della Sanità and Dipartimento Di Medicina Molecolare e Biotecnologie Mediche, Università degli Studi di Napoli Federico II and Azienda Ospedaliera Universitaria Federico II, Direzione Sanitaria protocol no. 0007133 of 08 May 2020; (iii) protocol no. 18/20; date: 10 June 2020, Genetics CEINGE TaskForce Covid19; Azienda Ospedaliera Universitaria Federico II, Direzione Sanitaria protocol no. 000576 of 10 April 2020.

STAR-METHODS

Cell culture

HEK-293T cells (CRL-3216, ATCC) and HEK-293T stable clones overexpressing human ACE2 (HEK293T-ACE2 cells) were grown in a humidified 37 °C incubator with 5% CO_2. The cells were cultured under feeder-free conditions using Dulbecco’s modified Eagle’s medium (DMEM; 41966-029; Gibco) with 10% fetal bovine serum (10270-106; Gibco), 2 mM L-glutamine (25030-024; Gibco), and 1% penicillin/streptomycin (P0781; Sigma-Aldrich), with the medium changed daily.

Freshly isolated human nasal epithelial cells were collected by nasal brushing of healthy donors (as previously described; Ferrucci *et al.*, 2021). These primary human epithelial cells (EVA - EMBL-EBI; project ID: PRJEB42411; analyses: ERZ1700617) were cultured in PneumaCult (no. 05009; STEMCELL Technologies) with 2 mM L-glutamine (25030-024, Gibco), and 1% penicillin/streptomycin (P0781, Sigma-Aldrich). The cells were dissociated with Trypsin-EDTA solution (T4049, Sigma-Aldrich) when the cultures reached ~80% confluency.

Generation of HEK293T-ACE2 stable clones

HEK293T-ACE2 stable clones were generated as previously described (Ferrucci *et al.*, 2022). Briefly, HEK293T cells (at ~70% confluency) were transfected with 1 μg DNA plasmid pCEP4-myc-ACE2 (#141185, Addgene) using X-tremeGENE 9 DNA Transfection Reagent (06365779001; Sigma-Aldrich) diluted with serum-free DMEM (41966-029; Gibco), to a concentration of 3 µL reagent/100 µL medium (3:1 ratio [µL]). The transfection complex was added to the cells after 15 min of incubation, in a dropwise manner. At 48 h from transfection, the cell culture medium was changed, and the cell clones were selected using 800 mg/mL hygromycin.

Transient transfections

ATP2B1-overexpressing cells. Primary human nasal epithelial cells (5×10^5) were seeded into 6-well culture plates, and after 24 h they were transiently transfected with the plasmid DNA construct pMM2-hATP2B1b (#47758, Addgene). Transient transfections were performed with X-tremeGENE 360 Transfection Reagent (XTG360-RO, #08724105001, Roche), according to the manufacturer instructions. Briefly, XTG360-RO DNA Transfection Reagent was diluted with serum-free DMEM (41966-029; Gibco) (10 µL reagent/500 µL medium). Then, 5 µg DNA plasmid was added to 500 µL diluted X-tremeGENE 9 DNA Transfection Reagent. The transfection reagent:RNA complex was incubated for 15 min at room temperature. The transfection complex was then added to the cells in a dropwise manner. Twelve hours after transfection, the cell culture medium was changed. At 48 h after transfection started, the cells were used for Ca^{2+} assays and immunoblotting analyses.

FOXO3-overexpressing cells. HEK-293T-ACE2 cells (3x105) were seeded in a 6 well plate and transfected for 48 hours with Flag-FOXO3 (Addgene Flag-FOXO3 #153142) plasmid. Transient transfections were performed with X-tremeGENE™ 360 Transfection Reagent (XTG360-RO, #08724105001, Roche), according to the manufacturer's instructions. Briefly, XTG360-RO DNA Transfection Reagent diluted with serum-free Dulbecco's modified Eagle's medium (41966-029; Gibco) (10 µl reagent/500 µl medium). Then, 2 µg per well of DNA plasmid were added to 250 µl of diluted X-tremeGENE 360 DNA Transfection Reagent. The transfection reagent:DNA complex was incubated for 15 minutes at room temperature. The transfection complex was then added to the cells in a dropwise manner. Twelve hours after transfection, the cell culture medium was changed. After 48 hours from the transfection started, the cells were used for immunoblotting analyses.

RNA interference

Primary human nasal epithelial cells. Primary human nasal epithelial cells (5×10^5) were seeded into 6-well culture plates, and after 12 h they were transiently transfected with the ATP2B1 siRNA (sc-42596, Santa-Cruz). A pool of a three siRNAs (sc-37007, sc-44230, sc-

44231, Santa-Cruz) was used as the negative control. RNA interference via siRNAs was performed using X-tremeGENE 360 Transfection Reagent (XTG360-RO), according to the manufacturer instructions. Briefly, X-tremeGENE 360:DNA (1μg/μL) (3:1) were mixed in DMEM without fetal bovine serum, and incubated at room temperature for 20 min. The mixture was then added to the cells in a dropwise manner and incubated for 48 h and 72 h for intracellular Ca^{2+} assays (as described below).

HEK293T-ACE2 cells. HEK-293T-ACE2 cells (3×10^5) were seeded into 6-well culture plates, and after 24 h they were transiently transfected with the ATP2B1 siRNA (sc-42596, Santa-Cruz). A pool of three siRNAs (sc-37007, sc-44230, sc-44231, Santa-Cruz) was used as the negative control. Transient transfections were performed with Lipofectamine RNAimax (13778-150, Invitrogen), according to the manufacturer instructions. Briefly, Lipofectamine RNAimax was diluted with serum-free DMEM (41966-029; Gibco) (9 μL reagent/150 μL medium). The siRNAs were then diluted in serum-free DMEM (3 μL siRNA/150 μL medium) to obtain the 30 pmol concentration. The transfection reagent:RNA complex was then incubated for 5 min at room temperature. The transfection complex was then added to the cells in a dropwise manner. After 12 h and 24 h the cells were infected with SARS-CoV-2 viral particles or lysed for immunoblotting analyses.

In-vitro treatment with compound PI-7

HEK293T-ACE and primary human nasal epithelial cells (2.5×10^5) were plated in 6-well plates and treated with 1 μM compound PI-7, or with 0.001% DMSO as the vehicle control. The proteomic analyses were performed after 24 h of treatment. The viral infections were performed after 1 h of treatment.

In-vitro treatment with Valproic Acid (VPA)

HEK293T-ACE2 cells were plated (2×10^5 cells/well) into 6-well plates. They were them treated with 20 mM Valproic Acid (VPA, #P4543, Sigma-Aldrich) or 0.01% DMSO (as negative control) for 16 h (as previously described; Zhang et al., 2013). Later the cells were lysed to investigate whether FOXO related genes are regulated.

Cell proliferation assays (i.e., cell index)

Real-time cell proliferation analysis for the Cell Index (i.e., the cell-sensor impedance was expressed every two minutes as a unit called "Cell Index"). HEK-293T-ACE2 cells (1.5 ×10^4) were plated. After 2 hours cells were treated with the indicated concentrations of PI-7 and PI-8 (from 200 to 1200 uM or from 0,1 to 10 uM); with vehicle-treated cells were the negative control. Impedance was measured every 2 min over 48 hours. The IC50 values were calculated through nonlinear regression analysis performed with Graph Pad Prism 9 ([inhibitor] vs. response (three parameters). Data are means ± SD of three independent experiments.

Ca^{2+} assays

Extra- and intra-cellular Ca^{2+} assays in human primary epithelial nasal cells treated with compound PI-7. Human nasal primary epithelial cells were plated (1.2 ×10^4 cells/well) into 24-well plates previously coated with PureCol (1:30,000; #5005, Advanced BioMatrix) with DMEM High Glucose (4500 mg/L, 41966-029; Gibco) or DMEM Low Glucose (1 g/L, D6046, Sigma-Aldrich). The cells were then treated with 100 µM compound PI-7 or vehicle (i.e., 0.001% DMSO) as negative control. After 24 hours from the treatment started, the cell media supernatant was used for the extracellular Ca^{2+} measurement, while the cell lysates for the intracellular Ca^{2+} relevation.

Regarding to the extracellular Ca^{2+}, the cell media supernatant (100 µl) was transfer into 96-well plates (3917, Costar) and incubated for 30 min at room temperature, and further 30 min at 37°C, with a solution (1:1, v:v; i.e., 100 µl) of MEM without phenol red and fetal bovine serum containing 2.5 µM Flu-3-AM (F1241, Invitrogen) supplemented with Pluronic F-127 (1:1, v:v; P3000MP, Invitrogen) and 2.5 mM probenecid inhibitor (57-66-9, Invitrogen). The relative fluorescent units (RFUs) were acquired (excitation, 506 nm; emission, 526 nm) and recorded every two minutes (for 30 min) by using a multimode plate reader (Enspire 2300, PerkinElmer). Regarding the intracellular Ca^{2+} measurement, the treated human nasal primary epithelial cells were washed two times with minimum essential medium (MEM; 21090-022, Gibco) without phenol red and fetal bovine serum. They were then incubated for two hours at room temperature with a solution (300 µl) of MEM without phenol red and fetal bovine serum containing 2.5 µM Flu-3-AM (F1241, Invitrogen) supplemented with Pluronic F-127 (1:1, v:v; P3000MP, Invitrogen) and 2.5 mM probenecid inhibitor (57-66-9, Invitrogen). The cells were subsequently washed three times with MEM containing probenecid. The cells were then further incubated for 1 hour at room temperature with 300 µl of 2 mM probenecid inhibitor dissolved in MEM, to allow hydrolysis of the AM ester bond, and then rinsed with MEM containing probenecid. The cells were then mechanically lysed and 100 μl were transferred into 96-well plates (3917, Costar) for intracellular (cytoplasmic) Ca^{2+} measurment. The relative fluorescent units (RFUs) were acquired (excitation, 506 nm; emission, 526 nm) every two minutes (up to 90 min) using a multimode plate reader (Enspire 2300, PerkinElmer).

Intracellular Ca2+ assays in human primary epithelial nasal cells overexpressing- or downregulating- ATP2B1. Nontransfected human nasal primary epithelial cells and those transfected with the ATP2B1 siRNA (for 48 h) were plated (3×10^4 cells/well) into 96-well plates (3917, Costar) previously coated with PureCol (1:30,000; #5005, Advanced BioMatrix). The cells were washed two times with minimum essential medium (MEM; 21090-022, Gibco) without phenol red and fetal bovine serum. They were then incubated for 30 min at room temperature with a solution of MEM without phenol red and fetal bovine serum containing 2.5 μM Flu-3-AM (F1241, Invitrogen) supplemented with Pluronic F-127 (1:1, v:v; P3000MP, Invitrogen) and 2 mM probenecid inhibitor (57-66-9, Invitrogen). The cells were subsequently washed three times to remove any dye that was nonspecifically associated with the cell surface, with MEM containing probenecid. The cells were then further incubated for 20 min at room temperature with 2 mM probenecid inhibitor dissolved in MEM, to allow hydrolysis of the AM ester bond, and then rinsed with MEM containing probenecid. The cells were then treated with 10 mM $CaCl_2$ (C3306-500G, Sigma) in MEM containing probenecid. The relative fluorescent units (RFUs) were immediately acquired (excitation, 506 nm; emission, 526 nm) using a multimode plate reader (Enspire 2300, PerkinElmer).

Caspase assay

HEK-293T-ACE2 ($3x10^4$) were plated in 96-well plate and treated with escalating doses (1 uM, 10 uM, 100 uM) of the drug PI-7 or the drug PI-8. Vehicle-treated (0.001% DMSO) cells were used as negative controls. Staurosporine-treated cells (10 μM) were used as positive controls of the assays. The assay was performed by using Caspase-3 Activity Assay Kit (#5723, Cell Signaling), by following the manufacture's instruction. Briefly, after 18 hours from the treatment started, cell medium was removed and 30 ul of cell lysis buffer (PI-7018, Cell Signaling) were added. The plate was then incubated for 5 minutes on ice. Later, 25 ul of cell lysate were mixed with 200 ul substrate solution B (#11734S, Cell Signaling) in a black 96 well plate. Fluorescence was detected by using a multimode plate reader (Enspire, 2300, PerkinElmer). The positive control AMC (25 µl, #11735S, Cell Signaling) mixed with 200 ul 1X assay buffer A (#11736S, Cell Signaling) was used as positive control of fluorescence.

SARS-CoV-2 isolation

SARS-CoV-2 was isolated from a nasopharyngeal swab obtained from an Italian patient, as previously described (Ferrucci *et al.*, 2021). Briefly, Vero E6 cells (8 $\times 10^5$) were plated in DMEM (41966-029; Gibco) with 2% fetal bovine serum in a T25 flask, to which the clinical specimen was added. The inoculated cultures were grown in a humidified 37 °C incubator with 5% CO_2. When cytopathic effects were observed (7 days after infection), the cell monolayers were scraped with the back of a pipette tip, and the cell culture supernatant containing the viral particles was aliquoted and frozen at −80 °C. Viral lysates were used for total nucleic acid extraction for confirmatory testing and sequencing (GISAID accession numbers: VOC Delta, EPI_ISL_3770696; VOC Omicron2, EPI_ISL_10743523).

SARS-CoV-2 infection

HEK293T-ACE2 and human primary epithelial nasal cells treated with 1 µM compound **PI-7** or vehicle (0.001% DMSO) were infected with SARS-CoV-2 viral particles. Noninfected cells were used as the negative control of infection. After 24, 48 and 72 h of infection, the cells were lysed for qPCR, immunoblotting, and RNA-seq, or fixed for immunofluorescence analyses. These experiments were performed in a BLS3-authorized laboratory.

RNA extraction and qPCR assays

RNA samples were extracted using TRIzol RNA Isolation Reagent (15596026, Invitrogen), according to the manufacturer instructions. Reverse transcription was performed with 5× All-In-One RT MasterMix (g592; ABM), according to the manufacturer instructions. The reverse transcription products (cDNA) were amplified by qRT-PCR using an RT-PCR system (7900; Applied Biosystems, Foster City, CA, USA). The cDNA preparation was through the cycling method, by incubating the complete reaction mix as follows: cDNA reactions: (37 °C for 10 min and 60 °C for 15 min); Heat-inactivation: 95 °C for 3 min; Hold stage: 4 °C.The targets were detected with the SYBR green approach, using BrightGreen BlasTaq 2× PCR MasterMix (G895; ABM). Human *ACTB* was used as the housekeeping gene to normalize the quantification cycle (Cq) values of the other genes. These runs were performed on a PCR machine (Quantstudio5, Lifetechnologies) with the following thermal protocol:

Hold stage: 50 °C for 2 min; Denaturation Step: 95 °C for 10 min; Denaturation and annealing (×45 cycles): 95 °C for 15 s and 60 °C for 60 s; Melt curve stage: 95 °C for 15 s, 60 °C for 1 min, and 95 °C for 15 s. Relative expression of the target genes was determined using the $2^{-\Delta\Delta Cq}$ method, as the fold increase compared with the controls. The data are presented as means ±SD of the $2^{-\Delta\Delta Cq}$ values (normalized to human ACTB) of three replicates.

Primers sequences for qPCR analyses

The details of the primers used in these SYBR green assays are provided in the supplementary information.

CoV-2 N1 Forward: GACCCCAAAATCAGCGAAAT
CoV-2 N1 Reverse: TCTGGTTACTGCCAGTTGAATCTG
ACTB Forward: GACCCAGATCATGTTTGAGACCTT
ACTB Reverse: CCAGAGGCGTACAGGGATAGC
IL-1β Forward: ATGATGGCTTATTACAGTGGCAA
IL-1β Reverse: GTCGGAGATTCGTAGCTGGA
TNFA Forward: CTCTTCTGCCTGCTGCACTTTG
TNFA Reverse: ATGGGCTACAGGCTTGTCACTC
ATP2B1 Forward: CGATCTCACTGGCTTATTCAGTCA
ATP2B1 Reverse: TAGCTGTAGCATTTCCCATGGTT
ATP2A1 Forward: AAC GAG GCC AAA GGT GTC TA
ATP2A1 Reverse: TCG AGA GGC TTC TCA CAT C
IL-12 Forward: TGA TGG CCC TGT GCC TTA GT
IL-12 Reverse: GGA TCC ATC AGA AGC TTT GCAT

Immunoblotting

Cells were lysed in 20 mM sodium phosphate, pH 7.4, 150 mM NaCl, 10% (v/v) glycerol, 1% (w/v) sodium deoxycholate, 1% (v/v) Triton X-100, supplemented with protease inhibitors (Roche). The cell lysates were cleared by centrifugation at 16,200× *g* for 30 min at room temperature, and the supernatants were removed and assayed for protein concentrations with Protein Assay Dye Reagent (BioRad). The cell lysates (20 μg) were resolved on 10% SDS-PAGE gels. The proteins were transferred to PVDF membranes (Millipore). After 1 h in blocking solution with 5% (w/v) dry milk fat in Tris-buffered saline containing 0.02% [v/v] Tween-20, the PVDF membranes were incubated with the primary antibody overnight at 4 °C:

anti-SARS-CoV-2 N protein (1:250; 35-579; ProSci Inc.); anti-PMCA ATPase (1:500; 5F10; # MA3-914, Invitrogen); anti-β-actin (1:10000; A5441; Sigma); anti-p65 (1:1000; sc-372, Santa Cruz Biotechnology); anti–p-(Ser^{311})p65–NF-κB (1:500; sc-101748. Santa Cruz Biotechnology); anti-Caspase-3 (1:500, ab49822, Abcam); anti-phosphorylated-Ser473-AKT (1:250, ab81283, Abcam); anti-AKT1 (1:500, #2967, Cell Signaling); anti-p-(Ser^{253})FOXO3A (1:500, ab47285, Abcam); anti-FOXO3A (1:1000, ab47409, Abcam). The membranes were then incubated with the required secondary antibodies for 1 h at room temperature, as secondary mouse or rabbit horseradish-peroxidase-conjugated antibodies (NC 15 27606; ImmunoReagents, Inc.), diluted in 5% (w/v) milk in TBS-Tween. The protein bands were visualized by chemiluminescence detection (Pierce-Thermo Fisher Scientific Inc., IL, USA). Densitometry analysis was performed with the ImageJ software. The peak areas of the bands were measured on the densitometry plots, and the relative proportions (%) were calculated. Then, the density areas of the peaks were normalized with those of the loading controls, and the ratios for the corresponding controls are presented as fold-changes. Immunoblotting was performed in triplicate. Densitometry analyses shown were derived from three independent experiments. Membrane and cytoplasmic protein fractions of the cultured cells were obtained with Mem-PER Plus Membrane Protein Extraction kits (89842, Thermo Scientific).

High resolution immunofluorescence

SARS-CoV-2–infected HEK293T-ACE2 cells were fixed in 4% paraformaldehyde in phosphate-buffered saline (PBS) for 30 min, washed three times with PBS, and permeabilized for 15 min with 0.1% Triton X-100 (215680010; Acros Organics) diluted in PBS. The cells were then blocked with 3% bovine serum albumin (A9418; Sigma) in PBS for 1 h at room temperature. The samples were incubated with the appropriate primary antibodies overnight at 4 °C: anti-ACE2 (1:1000; ab15348; Abcam); anti-SARS N protein (1:100; 35-579; ProSci Inc); or anti-GRP78 BiP (1:1000, ab21685, Abcam). After washing with PBS, the samples were incubated with the secondary antibody at room temperature for 1 h, as anti-mouse Alexa Fluor 488 (1:200; ab150113; Abcam) or anti-rabbit Alexa Fluor 647 (1:200; ab150075; Abcam). DNA was stained with DAPI (1:1000; #62254, Thermo Fisher). The slides were washed and mounted with cover slips with 50% glycerol (G5150; Sigma-Aldrich). Microscopy images were obtained using the Elyra 7 platform (Zeiss) with the optical Lattice SIM^2 technology (with the ZEN software, Zeiss, blue edition), using the 63× oil immersion objective.

Differential proteomics analysis

Differential proteomic analysis was carried out using a shotgun approach. In detail, three biological replicates of HEK293T-ACE2 cells treated for 24 h with compound PI-7 or with the vehicle control (0.001% DMSO) were lysed with lysis buffer (50 mM ammonium bicarbonate, 5% sodium dodecyl sulfate), and the protein extracts were quantified by BCA assay. The equivalent of 50 µg of each protein extract was reduced, alkylated, and digested onto S-Trap filters according to the Protifi protocol (Protifi, Huntington, NY), as previously reported. Peptide mixtures were dried in a SpeedVac system (Thermo Fisher, Waltham, MA) and an aliquot for each replicate was subjected to a clean-up procedure using a C18 zip-tip system (Merck KGaA, Darmstadt, Germany). Desalted peptide mixtures were resuspended in a solution of 0.2% HCOOH in LC-MS grade water (Waters, Milford, MA, USA) and 1 µL of each was analyzed using an LTQ Orbitrap XL (Thermo Scientific, Waltham, MA) coupled to the nanoACQUITY UPLC system (Waters). Samples were initially concentrated onto a C18 capillary reverse-phase pre-column (20 mm, 180 µm, 5 µm) and then fractionated onto a C18 capillary reverse-phase analytical column (250 mm, 75 µm, 1.8 µm), working at a flow rate of 300 nL/min. Eluents "B" (0.2% formic acid in 95% acetonitrile) and "A" (0.2% formic acid, 2% acetonitrile, in LC-MS/MS grade water, Merck) were used with a linear two-step gradient. The first step went from 5% B to 35% B in 150 min, and the second step from 35% B to 50% B in 10 min. MS/MS analyses were performed using Data-Dependent Acquisition (DDA) mode, after one full scan (mass range from 400 to 1800 *m/z*), with the 10 most abundant ions selected for the MS/MS scan events, and applying a dynamic exclusion window of 40 s. All of the samples were run in technical duplicates. The raw data were analyzed with MaxQuant 1.5.2 integrated with the Andromeda search engine. For the MaxQuant, the following parameters were used: a minimum of four peptides including at least two unique for protein identification; a false discovery rate (FDR) of 0.01 was used. Protein quantification was performed according to the label free quantification intensities, using at least four unmodified peptides razor + unique.

Protein-protein interaction networks

To investigate the interactions between the protein products of the top differentially expressed proteins in the HEK293T-ACE2 cells following treatment with compound PI-7, a protein interaction network was generated using the Search Tool for the Retrieval of Interacting Genes/ Proteins (STRING) database (https://string-db.org). The nodes consisted of genes and the edges were derived from experimentally validated protein-protein interactions.

RNA sequencing (RNA-seq)

RNA isolation and library construction and sequencing. Total RNA was isolated from the HEK293T-ACE2 cells using TRIzol RNA Isolation Reagent (#15596018; Ambion, Thermo Fisher Scientific). It was then quantified in a NanoDrop One/OneC Microvolume UV-Vis spectrophotometer (Thermo Scientific), checked for purity and integrity, and submitted to Macrogen Europe B.V. for sequencing. Libraries were prepared using TruSeq Stranded mRNA Library Prep kits according to the protocols recommended by the manufacturer (i.e., TruSeq Stranded mRNA Reference Guide # 1000000040498 v00). Trimmed reads were mapped to the reference genome with HISAT2 (https://ccb.jhu.edu/software/hisat2/index.shtml), a splice-aware aligner. After the read mapping, Stringtie (https://ccb.jhu.edu/software/stringtie/) was used for transcript assembly. The expression profile was calculated for each sample and transcript/gene as read counts, FPKM (fragment per kilobase of transcript per million mapped reads) and TPM (transcripts per kilobase million).

Analysis of differentially expressed genes. Differentially expressed genes analysis was performed on a comparison pair (SARS-CoV-2–infected *vs* noninfected cells). The read count value of the known genes obtained through the -e option of the StringTie was used as the original raw data. During data preprocessing, low quality transcripts were filtered out. Afterwards, Trimmed Mean of M-values (TMM) normalization was performed. Statistical analysis was performed using Fold Change, with exactTest using edgeR per comparison pair. For significant lists, hierarchical clustering analysis (Euclidean method, complete linkage) was performed to group the similar samples and genes. These results are depicted graphically using a heatmap and dendogram. For the enrichment test, which is based on Gene Ontology (http://geneontology.org/), DB was carried out with a significant gene list using g: Profiler tool (https://biit.cs.ut.ee/gprofiler/). Pathway enrichment analysis was performed using the KEGG database (http://www.genome.jp/kegg/).

ChIP-Seq analysis

ChIP-Seq of FOXO3 and the input control were downloaded from E-MTAB-2701.XC1. Reads were quality checked and filtered with Trimmomatic(Bolger et al., 2014). Alignments to the reference genome (hg19) were performed with BWA aln(Li and Durbin, 2010), using the default parameters. SAMtools rmdup (Li et al., 2009) was used to remove potential PCR duplicates. SAMtools sort and index were used to sort and index the bam files. Uniquely mapped reads of the FOXO3 signal were normalized over genomic input $\log_2$[FOXO3/Input]) using the bamCompare tool from Deeptools suite(Diaz et al., 2012) with the exactScaling method as the scaling factor. The normalized FOXO3 signal was visualized with UCSC genome browser.

Phenotype definition

The COVID19 asymptomatic cohort were selected as previously described [PMID:33815819]. The cohort included individuals from Campania (Italy) screened in May 2020 for SARS-CoV-2 who were positive for SARS-CoV-2 antibodies but without any COVID19 symptoms in the three previous months, such as hospitalization requirement, fever, cough or at least two symptoms among sore throat, headache, diarrhea, vomiting, asthenia, muscle pain, joint pain, smell or taste loss, and shortness of breath (Lavezzo et al., 2020). The COVID19 hospitalized cohort was selected as previously described (Russo et al., 2021; Andolfo et al., 2021).

In-silico analysis. The list of 351 coding variants of ATP2B1 was obtained from gnomAD (https://gnomad.broadinstitute.org/). FATHMM scores were used to assess the pathogenicity of the coding variants(Shihab et al., 2013). The GTEx database(Consortium, 2020)was used to select the eQTLs for ATP2B1, setting the level of significance at $P<1 \times 10^{-6}$. The GWAVA tool was used to assign a functional score to each SNP(Ritchie et al., 2014). RegulomeDB was used to evaluate the effects of SNPs on altering TFBS(Boyle et al., 2012).

DNA extraction, SNP genotyping. Genomic DNA of cases was extracted from peripheral blood using Maxwell RSC Blood DNA kits (Promega, Madison, WI, USA), and DNA concentrations and purities were evaluated using a NanoDrop 8000 spectrophotometer. The DNA samples were genotyped by the TaqMan SNP Genotyping Assay for the SNPs rs111337717 and rs116858620 (Applied Biosystems by Thermo Fisher Scientific, Waltham, MA, USA).

In-silico analysis of single-cell RNA-sequencing data

Publicly available single-cell RNA-sequencing data for adult human lung from COVID19 patients were used, from https://singlecell.broadinstitute.org/single_cell/study/SCP1219/columbia-university-nyp-covid-19-lung-atlas(Melms *et al.*, 2021). The proportions of ATP2B1-, ATP2B2-, ATP2B3-, and ATP2B4-positive cells in different lung cell types were calculated. In a similar manner, the expression of ATP2B1, ATP2B2, ATP2B3, ATP2B4, ATP2A1, ATP2A2, ATP2A3, and FOXOs in these lungs from COVID19 patients and controls were investigated.

Statistical analyses

Statistical significance was defined as $P < 0.05$ by unpaired two-tailed Student's *t*-tests. All of the data are given as means ±SD. In the Figures, statistical significance is represented as follows: $^{*}P < 0.05$, $^{**}P < 0.01$, and $^{***}P < 0.001$.

All of the data from the qRT-PCR assays were analyzed using un-paired two-tailed Student's *t*-tests, by comparing: (i) noninfected *versus* vehicle control infected cells (i.e., cells infected and treated with the vehicle as a control for the PI-7 treatment); and (ii) PI-7-treated cells *versus* vehicle control infected cells. Caspase-3 activities were analyzed using unpaired two-tailed Student's *t*-tests, by comparing the RFU values measured after 1 h of incubation to those obtained at the experimental starting point (i.e., time 0). The IC_{50} values for PI-7 and PI-8 were calculated by nonlinear regression analysis, performed with Graph- Pad Prism 9 (using [inhibitor] *versus* response [three parameters]). All of the experiments were performed in triplicate. Allele and genotype frequencies were compared using chi-square or Armitage tests. A two-sided $p < 0.05$ was considered statistically significant. Proteomic data were statistically analyzed using the Perseus software (Perseus version 1.6.15.0). Briefly, a Student's *t*-tests were applied with a false discovery rate cut-off of 0.05 and with a $\log_2FC$ cut-off of 0.5.

RESOURCE AVAILABILITY

Lead contact

Further information and requests for resources and reagents should be directed to and will be fulfilled by the lead contact, Prof. Massimo Zollo (massimo.zollo@unina.it).

Materials availability

This study did not generate new unique reagents.

Data and code availability

- Gene expression (RNAseq) data are deposited on RNA data bank at EBI (https://www.ebi.ac.uk), July 11- 2022 (code: E-MTAB-11973).
- Any additional information required to reanalyze the data reported in this paper is available from the lead contact upon request.

Acknowledgements

We thank P. Forestieri (President, CEINGE) and M. Giustino (CEO, CEINGE) for collaborative support of the program within the Regione Campania Covid19 Taskforce. We thank Christofer Berrie for providing professional and critical editing of the manuscript. We thank Prof. Francesco Broccolo for his valuable discussion on the therapeutic uses of the drug in a future therapeutic settings.

Funding

This study was supported by the project "CEINGE TaskForce COVID19," code D64I200003800 by Regione Campania for the fight against COVID19 (DGR no. 140; 17 March 2020). We further thank for support the Italian Association for Cancer Research (AIRC) Grant IG no. 22129 (M.Z.), the European School of Molecular Medicine for a doctorate program Fellowship (F.A.) and the Molecular Medicine Doctorate program Fellowship (F.B.), Fondazione Celeghin Italiana (M.Z.), and Ministero dell'Università e della Ricerca Italiana (PRIN) grant no. 2017FNZRN3 (M.Z.). We also thank NRF 2018R1A5A2025079–Korean Ministry of Science and ICT (J.-H.C.).

Author contributions

P.D.A. generated the HEK293T-ACE2 stable cell clones; V.F. performed immunofluorescence analyses and syncytia measurements. F.B. and F.A. performed immunoblotting analyses. R.S. prepared RNA and performed qPCR analyses; C.S. prepared proteins from cell lysates. F.A. performed intracellular Ca^{2+} assays and caspase analyses. F.G. and S.A. performed Chip-Seq analyses. A.B. and G.P. performed bioinformatic analyses. G.F., S.B., M.V., B.M.P., and P.C. performed SARS-CoV-2 infections in a BSL3-authorized laboratory; R.R., V.A.L., S.C., M.C., and A.I. performed polymorphisms analyses. J.H.C. and H.Y.K. performed docking analyses. M.Z. designed the experiments, discussed the experimental plans with the authors, and wrote the manuscript. All of the authors discussed the results and commented on the manuscript.

Conflicts of interest

The authors declare that they have no conflicts of interest.

Table

Table 1. Genetic association of the rs111337717 and rs116858620 SNPs in the *ATP2B1* gene according to severe and asymptomatic cases.

The rs111337717 and rs116858620 SNPs in the *ATP2B1* gene were tested in a cohort of 197 patients affected by severe COVID19 and 370 asymptomatic cases (D'Alterio *et al.*, 2022). The minor allele "C" of rs111337717 (NC_000012.12:g.89643729T>C) SNP [(CACATG(T/C)ACATTAT)] is significantly more frequent among severe COVID19 cases when compared with asymptomatic individuals (p=0.0004), thus indicating that rs111337717 can be listed among the genetic risk factors for predisposition to severe COVID19.

SNP	**Genetic association**	**Severe cases**	**Asymptomatic cases**	**P**	**Odds ratio**
rs111337717	Genotype	N=197	N=379		
	TT	165 (0.84)	345 (0.93)		
	CT	31 (0.15)	24 (0.06)		
	CC	1 (0.005)	1 (0.002)	0.0005*	2.3
	Allele	N=394	N=740		
	T	361 (0.92)	714 (0.96)		
	C	33 (0.08)	26 (0.03)	0.0004#	2.5
rs116858620	Genotype	N=199	N=364		
	TT	189 (0.95)	343 (0.94)		
	CT	10 (0.05)	21 (0.06)		
	CC	0 (0.0)	0 (0.0)	0.71	0.86
	Allele	N=398	N=728		
	T	388 (0.97)	707 (0.97)		
	C	10 (0.03)	21 (0.03)	0.71	0.86

*Armitage trend test: severe cases vs. asymptomatic cases

Fisher's exact test: severe cases vs. asymptomatic cases

Figures

Figure 1

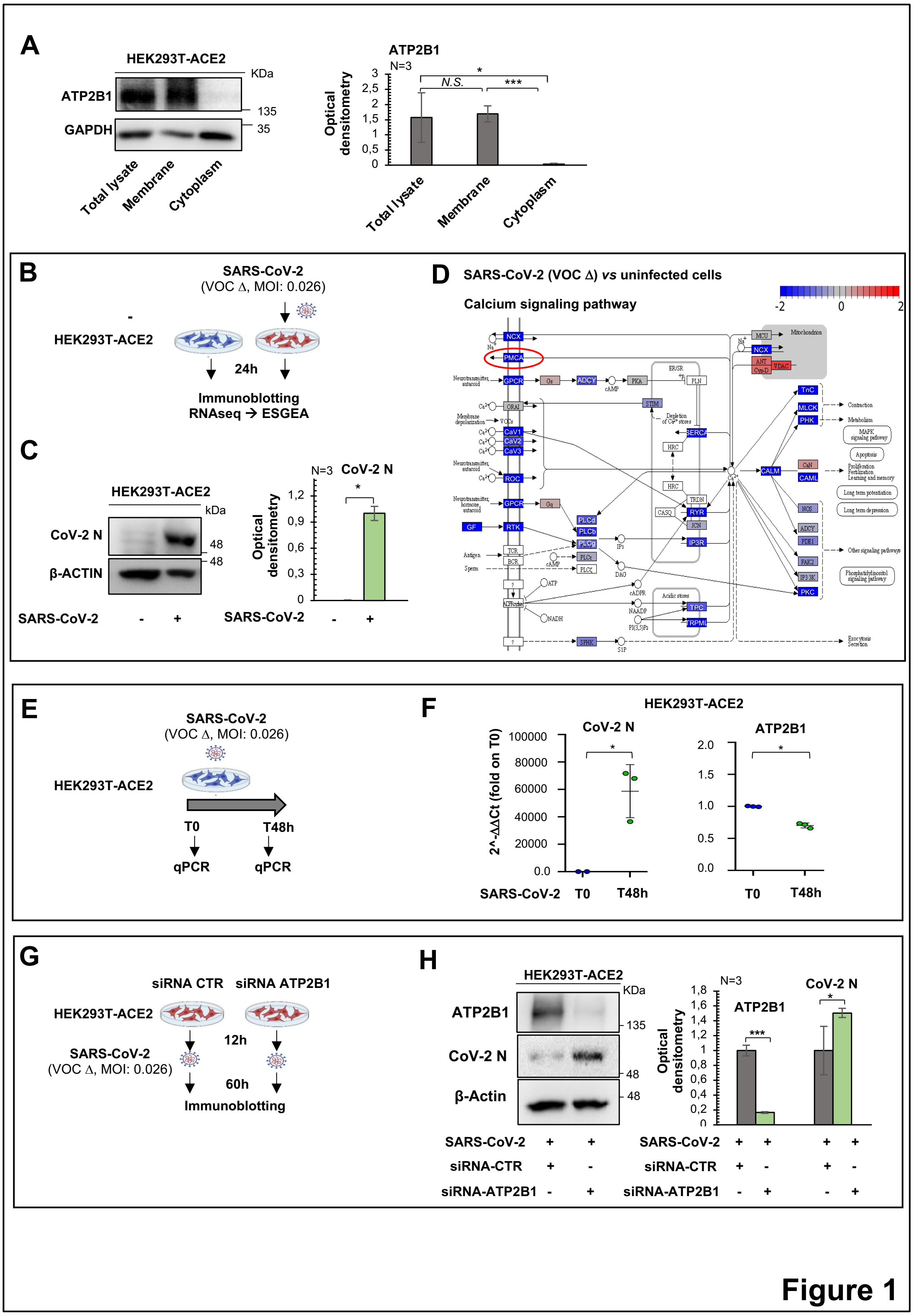

Figure 1. Dysregulated expression of Ca^{2+} pumps, including ATP2B1, during SARS-CoV-2 infection.

(A) Left: Representative immunoblotting analysis of cytosolic, membrane, and total protein lysate fractions obtained from HEK293T-ACE2 cells, using antibodies against the indicated proteins. β-Actin was used as the loading control. The experiment was performed in triplicate. Right: Densitometry analysis of the ATP2B1 band intensities from blots from three independent experiments. Data are means ±SD. * $p < 0.05$; *** $p < 0.0001$; NS, not significant (unpaired two-tailed student's *t*-tests; N = 3 independent experiments per group). **(B)** Experimental design for the HEK293T-ACE2 cells infected with SARS-CoV-2 (VOC Delta at 0.026 MOI) for 24 h. Noninfected cells cells were used as control. **(C)** Left: Representative immunoblotting analysis using antibodies against the indicated proteins on total protein lysates obtained from cells treated as above. Noninfected cells were used as control. All experiments were performed in triplicate. Right: Densitometry analysis of the viral N protein (CoV-2 N) band intensities in blots from three independent experiments. Data are means ±SD. * $p < 0.05$, (N = 3 independent experiments per group). **(D)** The Reactome pathway for "Calcium Signaling" displayed in a Reactome diagram view obtained from the differentially expresed genes between noninfected and SARS-CoV-2–infected HEK293T-ACE2 cells (VOC Delta, 0.026 MOI, 24 h) found through RNAseq analyses. Blue, downregulated genes upon SARS-CoV-2 infection; red, upregulated genes upon SARS-CoV-2 infection; red circle, PMCA Ca^{2+} pumps (or ATP2Bs). **(E)** Experimental design showing analyses of HEK293T-ACE2 cells infected with SARS-CoV-2 (VOC Delta at 0.026 MOI) for 48 h. Total RNA was extracted at T0 and after 48 h. **(F)** Quantification of mRNA abundance relative to control cells at T0 ($2^{-\Delta\Delta Ct}$) for the human *ATP2B1* and viral CoV-2 N genes. RT-PCR analysis of RNA extracted from HEK293T-ACE2 cells infected with SARS-CoV-2 VOC Delta for 48 h. Data are means ±SD. * $p < 0.05$, (unpaired two-tailed student's *t*-tests; N = 3 independent experiments per group). **(G)** Experimental design showing HEK293T-ACE2 cells downregulated for ATP2B1 (i.e., 12 h from transfection with the ATP2B1 siRNA) and then infected with SARS-CoV-2 (VOC Delta at 0.026 MOI) for a further 60 h. Control (CTR) cells were transfected with a pool of three unrelated siRNAs and then infected with SARS-CoV-2. **(H)** Left: Representative immunoblotting analysis using antibodies against the indicated proteins on total protein lysates obtained from HEK293T-ACE2 cells downregulated for ATP2B1 and infected with SARS-CoV-2. All experiments were performed in triplicate. Right: Densitometry analysis of the indicated band intensities in blots from three independent experiments. Data are means ±SD. * $p < 0.05$, *** $p < 0.001$ (unpaired two-tailed student's *t*-tests; N = 3 independent experiments per group).

Figure 2

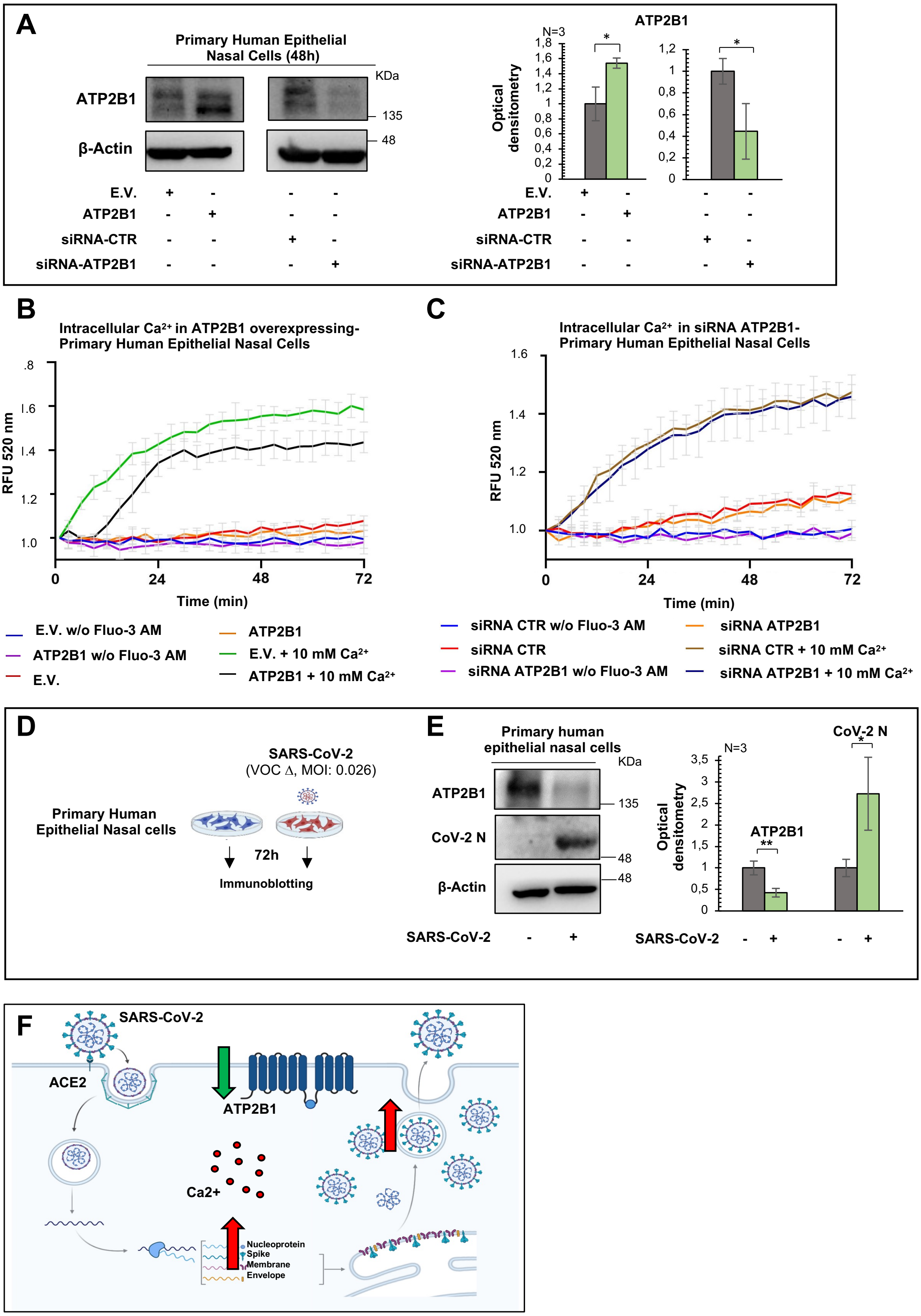

Figure 2

Figure 2. Reduced ATP2B1 protein levels promote SARS-CoV-2 replication via increasing intracellular Ca^{2+}.

(A) Left: Representative immunoblotting analysis using antibodies against the indicated proteins on total protein lysates obtained from human primary epithelial nasal cells transiently overexpressing ATP2B1 (48 h after transfection with the plasmid DNA construct pMM2-hATP2B1b) without (siRNA-CTR) and with (siRNA-ATP2B1) downregulation of ATP2B1. Cells overexpressing the empty vector (E.V.) or a pool of three unrelated siRNAs (siRNA-CTR) were used as negative controls. β-Actin was used as the loading control. All experiments were performed in triplicate. Right: Densitometry analysis of the ATP2B1 band intensities in blots from three independent experiments. Data are means ±SD. * $p < 0.05$ (unpaired two-tailed student's *t*-tests; N = 3 independent experiments per group). E.V., Empty Vector. **(B, C)** Quantification of relative fluorescence changes of Fluo3 as a measure of intracellular Ca^{2+} levels. Intracellular calcium (Ca^{2+}) levels were measured using Fluo3-AM for up to 72 min in human primary epithelial nasal cells overexpressing ATP2B1 (48 h after transfection with the plasmid DNA construct pMM2-hATP2B1b), cells overexpressing the empty vector [E.V.] used as negative control) **(B)** and cells downregulated for ATP2B1 (48 h after transfection with the ATP2B1 siRNA; with cells transfected with a pool of three unrelated siRNAs as negative control) **(C)**. RFU, relative fluorescent units. Cells without Fluo3-AM were also used as negative control of the experiments. All experiments were performed in triplicate. N = 3 independent experiments per group. **(D)** Experimental design showing primary human epithelial nasal cells infected with SARS-CoV-2 (VOC Delta at 0.026 MOI) for 72 h. **(E)** Left: Representative immunoblotting analysis using antibodies against the indicated proteins for total protein lysates obtained from cells treated as above. Noninfected cells were used as control. All experiments were performed in triplicate. Right: Densitometry analysis of the indicated band intensities in blots from three independent experiments. Data are means ±SD. * $p < 0.05$, ** $p < 0.01$; (unpaired two-tailed student's *t*-tests; N = 3 independent experiments per group). **(F)** Cartoon representation to illustrate our hypothesis for the role of ATP2B1 during SARS-CoV-2 infection. Downregulation of ATP2B1 can stimulate SARS-CoV-2 replication (increased expression of the viral N protein), via increased intracellular Ca^{2+} levels.

Figure 3

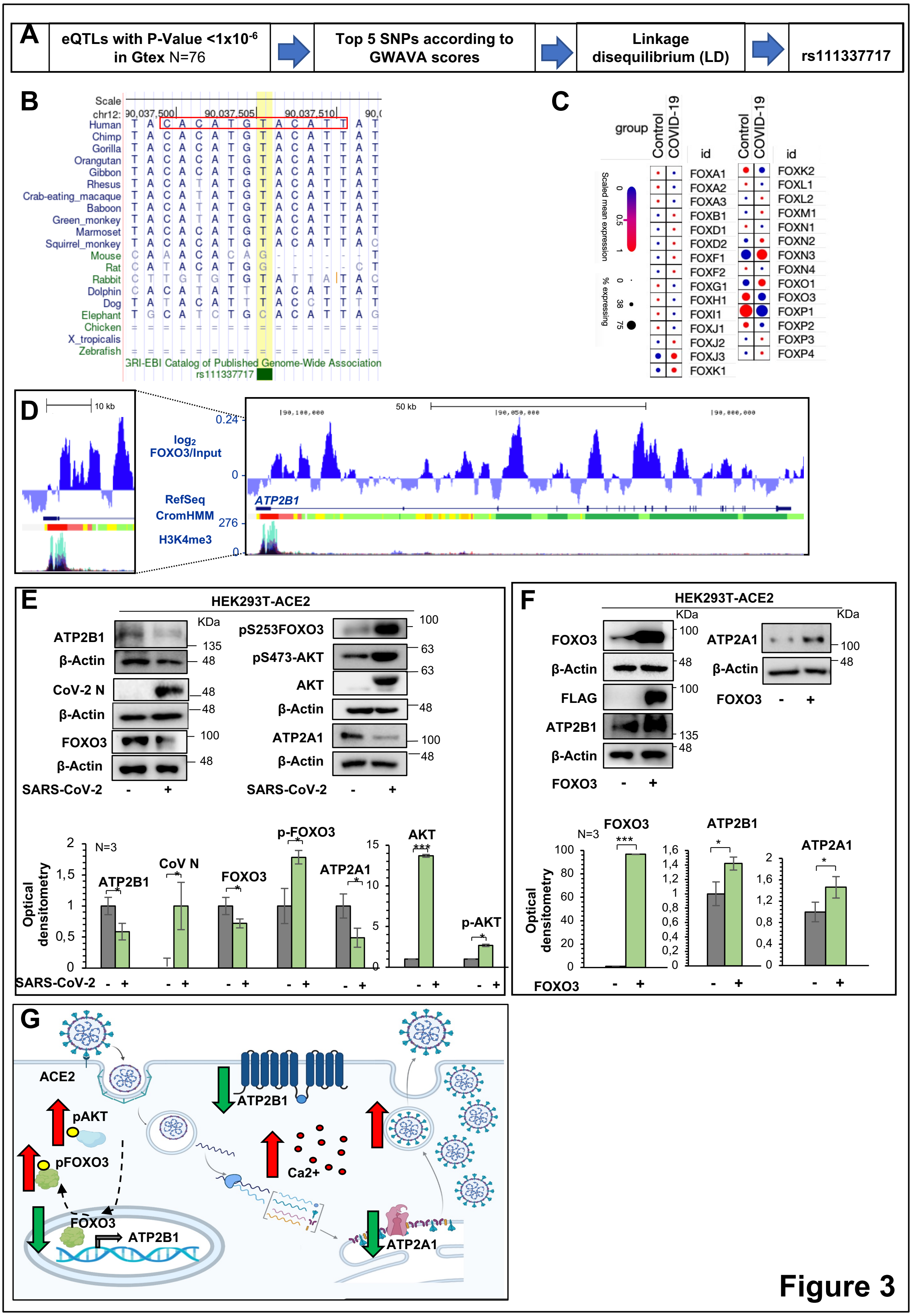
A
eQTLs with P-Value <1x10-6 in Gtex N=76
Top 5 SNPs according to GWAVA scores
Linkage disequilibrium (LD)
rs111337717
B
Scale
chr12:
90,037,500
90,037,505
90,037,510
Human
Chimp
Gorilla
Orangutan
Gibbon
Rhesus
Crab-eating_macaque
Baboon
Green_monkey
Marmoset
Squirrel_monkey
Mouse
Rat
Rabbit
Dolphin
Dog
Elephant
Chicken
X_tropicalis
Zebrafish
GRI-EBI Catalog of Published Genome-Wide Association
rs111337717
C
group
Control
COVID-19
id
Scaled mean expression
0
0.5
1
% expressing
0
38
75
FOXA1
FOXA2
FOXA3
FOXB1
FOXD1
FOXD2
FOXF1
FOXF2
FOXG1
FOXH1
FOXI1
FOXJ1
FOXJ2
FOXJ3
FOXK1
FOXK2
FOXL1
FOXL2
FOXM1
FOXN1
FOXN2
FOXN3
FOXN4
FOXO1
FOXO3
FOXP1
FOXP2
FOXP3
FOXP4
D
10 kb
50 kb
90,100,000
90,050,000
90,000,000
0.24
log2 FOXO3/Input
0
RefSeq
CromHMM
276
H3K4me3
0
ATP2B1
E
HEK293T-ACE2
KDa
ATP2B1
135
β-Actin
48
CoV-2 N
48
β-Actin
48
FOXO3
100
β-Actin
48
SARS-CoV-2
-
+
pS253FOXO3
100
pS473-AKT
63
AKT
63
β-Actin
48
ATP2A1
100
β-Actin
48
SARS-CoV-2
-
+
N=3
Optical densitometry
2
1,5
1
0,5
0
ATP2B1
CoV N
FOXO3
p-FOXO3
ATP2A1
AKT
p-AKT
15
10
5
0
*
***
SARS-CoV-2
- +
F
HEK293T-ACE2
KDa
FOXO3
100
β-Actin
48
FLAG
100
ATP2B1
135
β-Actin
48
FOXO3
- +
KDa
ATP2A1
100
β-Actin
48
FOXO3
- +
N=3
FOXO3
***
ATP2B1
*
ATP2A1
*
Optical densitometry
100
80
60
40
20
0
1,6
1,4
1,2
1
0,8
0,6
0,4
0,2
0
2
1,6
1,2
0,8
0,4
0
FOXO3
- +
G
ACE2
pAKT
pFOXO3
FOXO3
ATP2B1
ATP2B1
Ca2+
ATP2A1
Figure 3

Figure 3. The homozygous intronic variant rs11337717 in the *ATP2B1* locus is responsible for SARS-CoV-2 increased replication in COVID patients.

(A) *In-silico* analysis for the presence of noncoding variants in the genomic region of the *ATP2B1* locus acting as expression quantitative traits (eQTLs) located in putative elements responsible for transcriptional regulation. Here, 77 SNPs were selected that were eQTLs for the *ATP2B1* gene ($P<1 \times 10^{-6}$) using the GTex database. These SNPs were then annotated with prediction functional scores calculated by the GWAVA tool. The top five SNPs were selected to verify their linkage disequilibrium (LD). The rs111337717 SNP was not in linkage disequilibrium. **(B)** Alignment of the sequence genomic region flanking rs111337717 SNP (NC_000012.12:g.89643729T>C) SNP [(CACATG(T/C)ACATTAT)] shows the conservation through evolution across different species, with a degree of sequence identity and homology. **(C)** Literature search of publically available datasets obtained from single-nuclei RNA-seq on >116,000 nuclei from 19 COVID19 autopsy lungs and 7 pre-pandemic controls (https://singlecell.broadinstitute.org/single_cell/study/SCP1052/covid-19-lung-autopsy-samples [Melms *et al.*, 2021]) to determine whether FOXOs transcriptional factors showed distinct fractional and dysfunctional changes across the lungs from the COVID19 decedents. **(D)** Genome browser screenshots showing accumulation of normalized FOXO3 signal, together with CromHMM state segmentation and the H3K4me3 signal (ENCODE), along the *ATP2B1* gene in human cells. For the CromHMM state segmentation: bright red, promoter; orange and yellow, enhancer; green, transcriptional transition; red arrow, polymorphism-containing region. The expanded view of the highlighted region (left) shows FOXO3 peaks over the *ATP2B1* promoter and enhancer regions, as marked by H3K4me3 and CromHMM (red and orange regions) respectively. **(E)** Representative immunoblotting analysis using antibodies against the indicated proteins on total protein lysates obtained from HEK293T-ACE2 cells infected with SARS-CoV-2 VOC Delta at 0.026 MOI for 72 h. Noninfected cells were used as negative control. All experiments were performed in triplicate. Densitometry analysis of the indicated band intensities in blots from three independent experiments. Data are means ±SD. * $p < 0.05$, *** $p < 0.001$ (unpaired two-tailed student's *t*-tests; N = 3 independent experiments per group). **(F)** Representative immunoblotting analysis using antibodies against the indicated proteins on total protein lysates obtained from HEK293T-ACE2 cells transiently transfected with the human FOXO3 encoding plasmid for 48 h. Empty vector transfected cells were used as negative control. All experiments were performed in triplicate. Densitometry analysis of the indicated band intensities in blots from three independent experiments. Data are means ±SD. * $p < 0.05$, *** $p < 0.001$ (unpaired two-tailed student's *t*-tests; N = 3 independent experiments per group). **(G)** Cartoon representation to illustrate our hypothesis for downregulation of ATP2B1 during SARS-CoV-2 infection via the FOXO3 transcriptional factor. During SARS-CoV-2 infection, the PI3K/Akt pathway is activated and enhances the phosphorylation of FOXO3, thus excluding it from the nucleus. As a consequence, the expression of the FOXO3 targets, including ATP2B1, are also reduced, thus increasing the intracellular Ca^{2+} levels and further promoting SARS-CoV-2 replication.

Figure 4

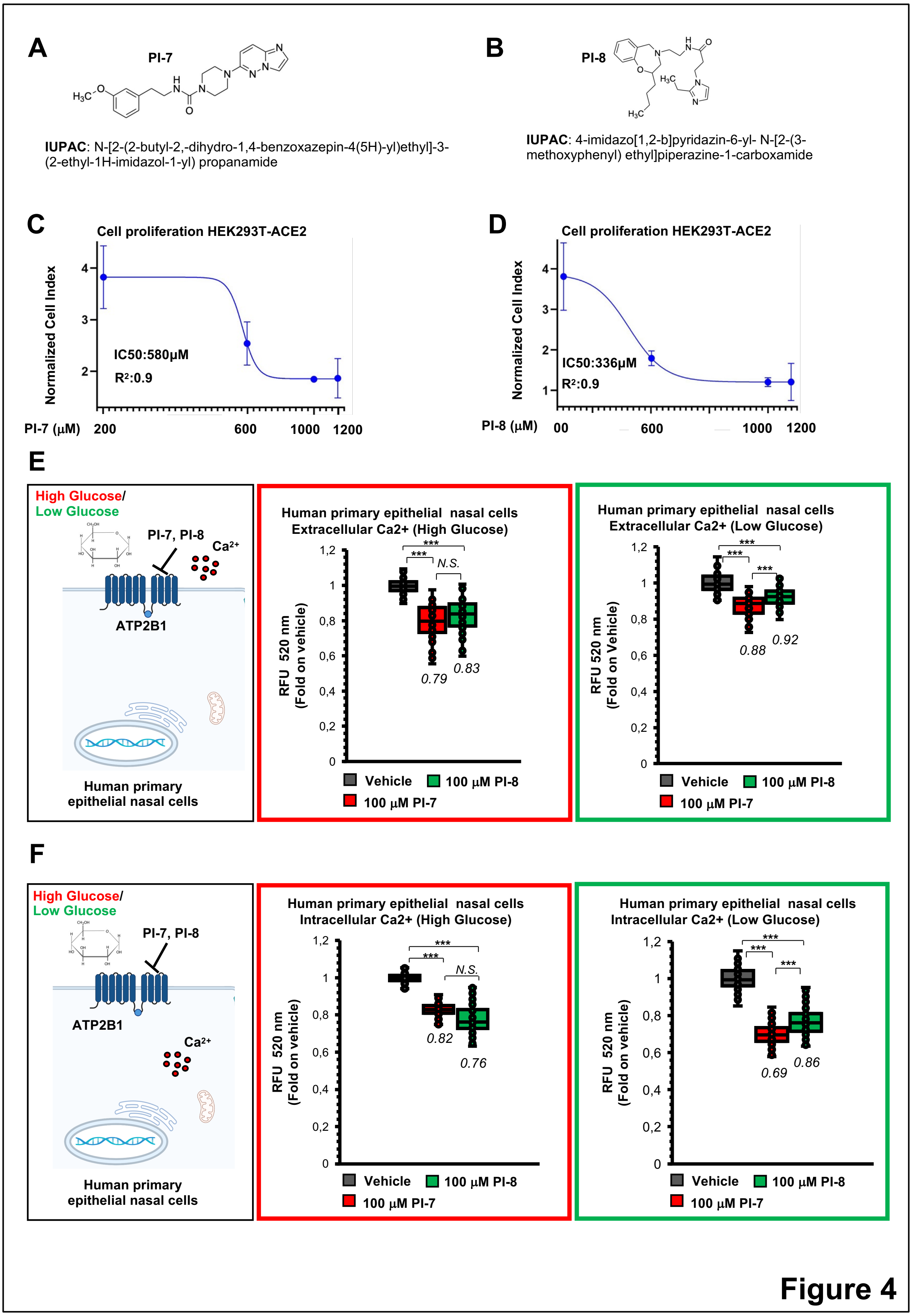
A
PI-7
IUPAC: N-[2-(2-butyl-2,-dihydro-1,4-benzoxazepin-4(5H)-yl)ethyl]-3-(2-ethyl-1H-imidazol-1-yl) propanamide
B
PI-8
IUPAC: 4-imidazo[1,2-b]pyridazin-6-yl- N-[2-(3-methoxyphenyl) ethyl]piperazine-1-carboxamide
C
Cell proliferation HEK293T-ACE2
Normalized Cell Index
IC50:580μM
R²:0.9
PI-7 (μM) 200 600 1000 1200
D
Cell proliferation HEK293T-ACE2
Normalized Cell Index
IC50:336μM
R²:0.9
PI-8 (μM) 00 600 1000 1200
E
High Glucose/
Low Glucose
PI-7, PI-8
Ca²⁺
ATP2B1
Human primary epithelial nasal cells
Human primary epithelial nasal cells
Extracellular Ca2+ (High Glucose)
RFU 520 nm (Fold on vehicle)
*** *** N.S.
0.79 0.83
Vehicle
100 μM PI-8
100 μM PI-7
Human primary epithelial nasal cells
Extracellular Ca2+ (Low Glucose)
RFU 520 nm (Fold on Vehicle)
*** *** ***
0.88 0.92
Vehicle
100 μM PI-8
100 μM PI-7
F
High Glucose/
Low Glucose
PI-7, PI-8
ATP2B1
Ca²⁺
Human primary epithelial nasal cells
Human primary epithelial nasal cells
Intracellular Ca2+ (High Glucose)
RFU 520 nm (Fold on vehicle)
*** *** N.S.
0.82 0.76
Vehicle
100 μM PI-8
100 μM PI-7
Human primary epithelial nasal cells
Intracellular Ca2+ (Low Glucose)
RFU 520 nm (Fold on vehicle)
*** *** ***
0.69 0.86
Vehicle
100 μM PI-8
100 μM PI-7
Figure 4

Figure 4. ATP2B1 impairment using the caloxin derivative (compounds PI-7 and PI-8) diminishes extra- and intra-cellular Ca^{2+} levels.

(A, B) Molecular structures and IUPAC names of compounds PI-7 **(a)** and PI-8 **(b)** selected from the screening. **(C, D)** Real-time cell proliferation analyses in HEK293T-ACE2 cells (Cell Index; i.e., cell-sensor impedance expressed every 2 min). IC_{50} values calculated through nonlinear regression analysis performed with Graph Pad Prism 9 ([inhibitor] vs. response [three parameters]) for PI-7 **(C)** and PI-8 **(D)**. Briefly, HEK293T-ACE2 were plated and, after 2 h they were treated with the indicated concentrations of PI-7 and PI-8; with vehicle-treated cells (0.001% DMSO) as the negative control. Impedance was measured every 2 min over 48 h. The graphs were generated using Graph Pad Prism 9, with the IC50 values given (PI-7: 580 μM, R^2 0.9; PI-8: 336 μM, R^2 0.9). Data are means ±SD of three independent experiments. **(E)** Extracellular Ca^{2+} as measured using Fluo3-AM over 30 min in human primary epithelial nasal cells (1.2×10^4 cells/well) plated in DMEM High Glucose or DMEM Low glucose and treated with 100 μM compounds PI-7 and PI-8, or with 0.001% DMSO as vehicle. After 24 hours from the treatment started, the cell media supernatant was used for the extracellular Ca^{2+} measurement. The graph shows quantification of relative fluorescence changes of Fluo3 as a measure of extracellular Ca^{2+} levels by showing the relative fluorescent units (RFUs) (excitation, 506 nm; emission, 526 nm) recorded every two minutes for 30 min by using a multimode plate reader (Enspire 2300, PerkinElmer). Data are means ±SD. *** $p < 0.001$; N.S., not significant. (unpaired two-tailed student's *t*-tests; N = 3 independent experiments per group). The fold values on vehicle controls are indicated within the graph. Red box: High Glucose; Green Box: Low glucose. Data are means ± SD of three independent experiments. **(F)** Intracellular Ca^{2+} as measured using Fluo3-AM over 90 min in human primary epithelial nasal cells (1.2×10^4 cells/well) plated in DMEM High Glucose or DMEM Low glucose and treated with 100 μM compounds PI-7 and PI-8, or with 0.001% DMSO as the vehicle. After 24 hours from the treatment started, the cells were used for the intracellular Ca^{2+} measurement. The graph shows quantification of relative fluorescence changes of Fluo3 as a measure of intracellular Ca^{2+} levels by showing the relative fluorescent units (RFUs) (excitation, 506 nm; emission, 526 nm) recorded every two minutes for 90 min by using a multimode plate reader (Enspire 2300, PerkinElmer). Data are means ±SD. *** $p < 0.001$; N.S., not significant. (unpaired two-tailed student's *t*-tests; N = 3 independent experiments per group). The fold values on vehicle control are shown within the graph. Red box: High Glucose; Green Box: Low glucose. Data are means ±SD of three independent experiments.

Figure 5

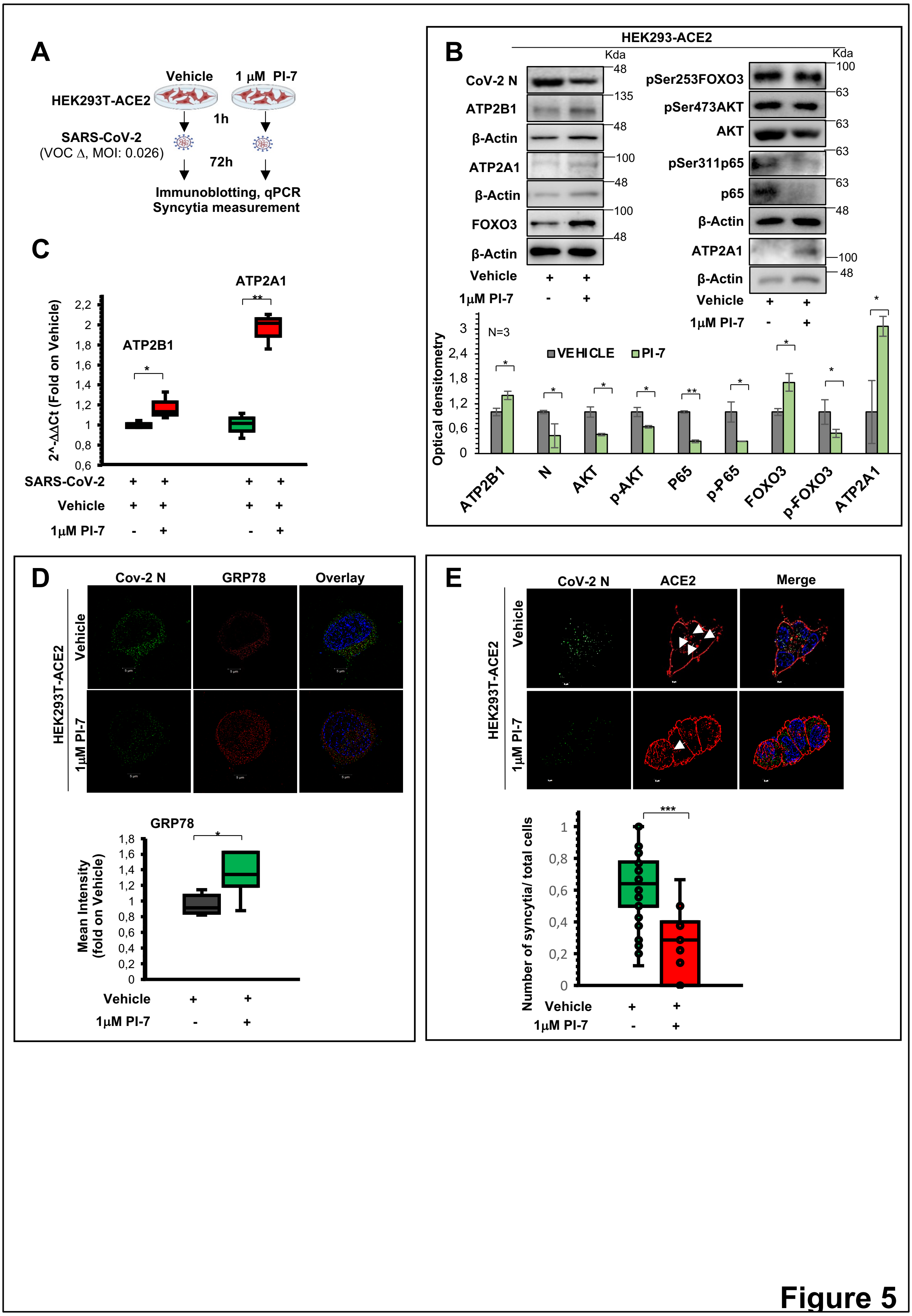
A
Vehicle
1 µM PI-7
HEK293T-ACE2
1h
SARS-CoV-2
(VOC Δ, MOI: 0.026)
72h
Immunoblotting, qPCR
Syncytia measurement
B
HEK293-ACE2
Kda
CoV-2 N
ATP2B1
β-Actin
ATP2A1
β-Actin
FOXO3
β-Actin
Vehicle + +
1µM PI-7 - +
pSer253FOXO3
pSer473AKT
AKT
pSer311p65
p65
β-Actin
ATP2A1
β-Actin
Vehicle + +
1µM PI-7 - +
48
135
48
100
48
100
48
100
63
63
63
63
48
100
48
N=3
VEHICLE
PI-7
Optical densitometry
3
2,4
1,8
1,2
0,6
0
ATP2B1
N
AKT
p-AKT
P65
p-P65
FOXO3
p-FOXO3
ATP2A1
*
**
C
2^-ΔΔCt (Fold on Vehicle)
2,2
2
1,8
1,6
1,4
1,2
1
0,8
0,6
ATP2B1
ATP2A1
SARS-CoV-2 + + + +
Vehicle + + + +
1µM PI-7 - + - +
D
Cov-2 N
GRP78
Overlay
HEK293T-ACE2
Vehicle
1µM PI-7
GRP78
Mean Intensity (fold on Vehicle)
1,8
1,6
1,4
1,2
1
0,8
0,6
0,4
0,2
0
Vehicle + +
1µM PI-7 - +
E
CoV-2 N
ACE2
Merge
HEK293T-ACE2
Vehicle
1µM PI-7
Number of syncytia/ total cells
1
0,8
0,6
0,4
0,2
0
***
Vehicle + +
1µM PI-7 - +
Figure 5

Figure 5. ATP2B1 impairment using the caloxin derivative (compound PI-7) diminishes SARS-CoV-2 propagation and syncytia formation.

(A) Experimental plan for HEK293T-ACE2 cells treated with 1 μM PI-7, or 0.001% DMSO as vehicle control. After 1 h, the cells were infected with SARS-CoV-2 viral particles of VOC Delta at 0.026 MOI for 72 h. The cells were then fixed or lysed for immunofluorescence or qPCR and immunoblotting, respectively. **(B)** Representative immunoblotting analysis using antibodies against the indicated proteins on total protein lysates obtained from HEK293T-ACE2 treated as in (**b**). All experiments were performed in triplicate. Densitometry analysis of the indicated band intensities in blots from three independent experiments. Data are means ±SD. * $p < 0.05$, ** $p < 0.01$; (unpaired two-tailed student's *t*-tests; N = 3 independent experiments per group). **(C)** Quantification of mRNA abundance relative to that in control (CTR) cells ($2^{-\Delta\Delta Ct}$) for the human *ATP2B1* and *ATP2A1s* genes, from RT-PCR analysis of RNA extracted from HEK293T-ACE2 cells treated as in (**A**). Data are means ±SD. * $p < 0.05$, ** $p < 0.01$ (unpaired two-tailed student's *t*-test; N = 3 independent experiments per group). **(D)** Immunofluorescence staining with an antibody against viral CoV-2 N (green) and human GRP78 (red) proteins in HEK293T-ACE2 cells treated with PI-7 molecules and infected with SARS-CoV-2 for 72 hours (i.e., treated as in **A**). The graph showing the intensity of fluorescence was shown on the left. Data are means ± SD. P-value was determined by unpaired two-tailed Student's *t* test; N = three independent experiments per group. The SIM^2 image was acquired with Elyra 7 and processed with Zeiss ZEN software (blue edition). Magnification, ×63. Scale bar, 5 μm. **(E)** Representative immunofluorescence staining with an antibody against the CoV-2 viral N protein (green) and human ACE2 (red) in HEK293T-ACE2 cells treated as in (**A**). The SIM^2 image was acquired with Elyra 7 and processed with Zeiss ZEN software (blue edition). Magnification, ×63. Quantification of the relative proportions of syncytia in >300 cells per condition. Data are means ±SD, with the P-value determined by unpaired two-tailed Student's *t*-test (N = three independent experiments per group). Scale bar, 5 μm.

Figure 6

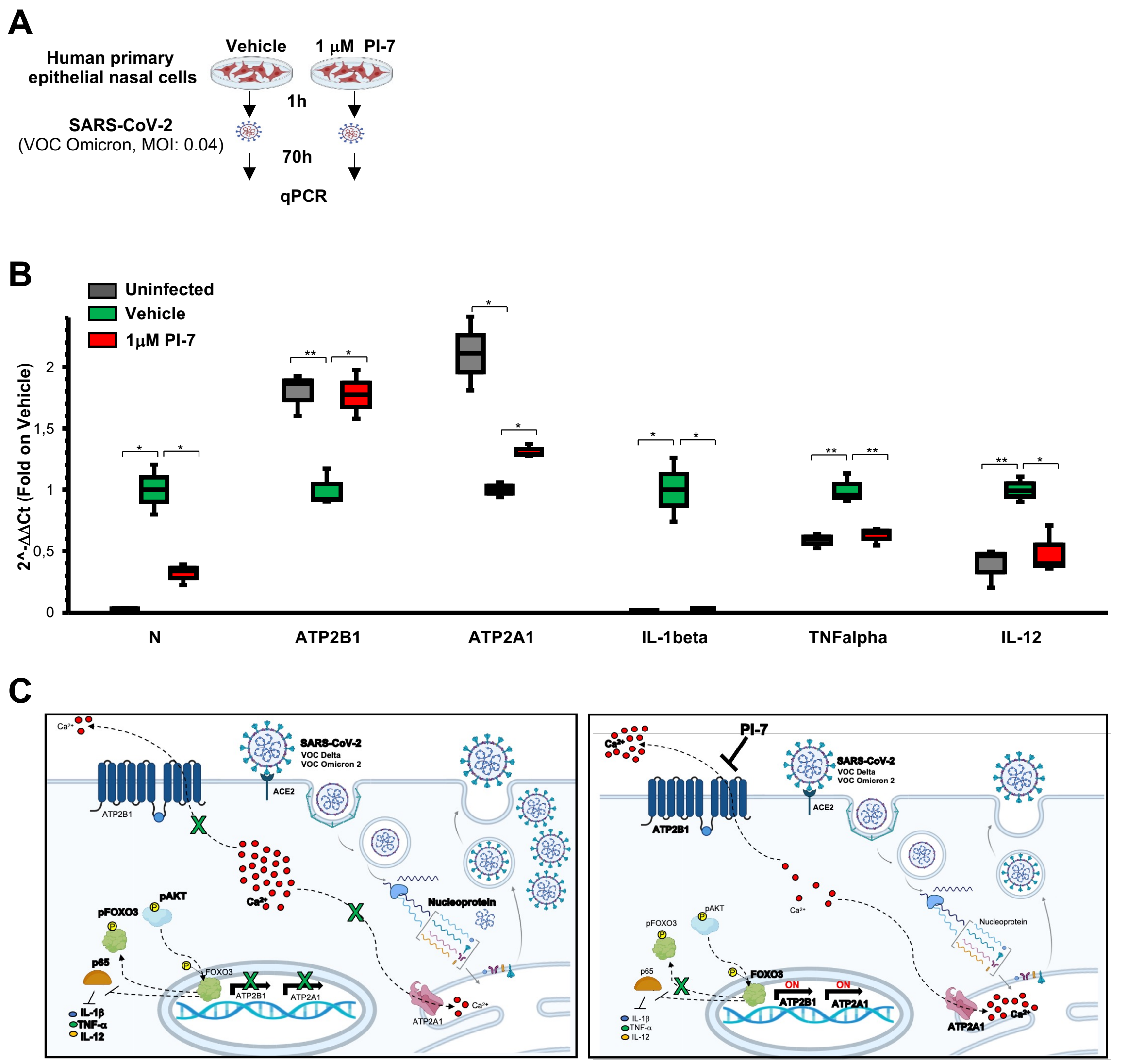

Figure 6

Figure 6. Antiviral activity of caloxin-derivative (compound PI-7) is also shown via inhibition of the cytokine storm against Omicron 2 variant.

(A) Experimental plan for human primary epithelial cells treated with 1 μM PI-7 or 0.001% DMSO as vehicle control. After 1 h, the cells were infected with SARS-CoV-2 viral particles of VOC Omicron 2 at 0.04 MOI for 70 h. The cells were then used for qPCR analysis.

(B) Quantification of mRNA abundance relative to that in control (Vehicle) cells ($2^{-\Delta\Delta Ct}$) for the indicated cytokines in HEK293T-ACE2 cells treated as in (**A**). Data are means ±SD. **P* <0.05, ** P <0.01 (as determined by unpaired two-tailed Student's *t*-tests; n = three independent experiments per group). Uninfected cells are used as negative control. **(C)** Cartoon representation to illustrate our hypothesis for the role of *ATP2B1* during SARS-CoV-2 infection upon treatment with compound PI-7. **On the left:** during SARS-CoV-2 infection, the PI3K/Akt pathway is activated via Akt phosphorylation, thus enhancing the phosphorylation of FOXO3 to exclude it from the nucleus (Manning and Cantley, 2007, Stefanetti et al., 2018). As a consequence, the expression of the FOXO3 targets, including ATP2B1 and ATP2A1, are reduced, thus increasing the intracellular Ca^{2+} levels and further promoting SARS-CoV-2 replication. Furthermore, SARS-CoV-2 infection also leads to NF-κB activation (also due to reduction of active FOXO3; Thompson et al., 2015) and, as a consequence, the expression of the inflammatory cytokines (e.g., IL-1β, TNF-α and IL-12) belonging to the cytokine storm resulted increased. **On the right:** Treatment with the caloxin-derivative (compound PI-7) inhibits the viral propagation of SARS-CoV-2 (VOC: Delta and Omicron 2) by blocking ATP2B1 pump activity, thus reducing both the extra- and intracellular Ca^{2+} levels that are necessary for SARS-CoV-2 replication. Compound PI-7 also increases *ATP2B1* and *ATP2A1* levels, thus further reducing the intracellular Ca^{2+} levels because of its extracellular export via *ATP2B1* (on the plasma membrane), and potentially the endoplasmic reticulum import through *ATP2A1*. These increased levels of *ATP2B1* and *ATP2A1* occurred because of the enhancement of transcriptionally active FOXO3. The levels of active unphosphorylated-FOXO3 are increased due to the inactivation of PI3K/AKT pathway (due to decreased viral infection upon compound PI-7). As a consequence, the levels of nuclear active FOXO3 results increased, thus enhancing the transcriptional activation of *ATP2B1* and *ATP2A1.* Treatment with PI-7 also reduces NF-κB activation (due to enhancement of FOXO3) and as a consequence, the expression of the inflammatory cytokines belonging to the cytokine storm resulted decreased IL-1β, TNF-α and IL-12. All the gene names whose expression resulted upregulated are depicted in bold.

References

Acheampong, K.K., Schaff, D.L., Emert, B.L., Lake, J., Reffsin, S., Shea, E.K., Comar, C.E., Litzky, L.A., Khurram, N.A., Linn, R.L., et al. (2022). Subcellular Detection of SARS-CoV-2 RNA in Human Tissue Reveals Distinct Localization in Alveolar Type 2 Pneumocytes and Alveolar Macrophages. mBio, e0375121. 10.1128/mbio.03751-21.

Andersen, K.G., Rambaut, A., Lipkin, W.I., Holmes, E.C., and Garry, R.F. (2020). The proximal origin of SARS-CoV-2. Nat Med *26*, 450-452. 10.1038/s41591-020-0820-9.

Andolfo, I., Russo, R., Lasorsa, V.A., Cantalupo, S., Rosato, B.E., Bonfiglio, F., Frisso, G., Abete, P., Cassese, G.M., Servillo, G., et al. (2021). Common variants at 21q22.3 locus influence MX1 and TMPRSS2 gene expression and susceptibility to severe COVID-19. iScience *24*, 102322. 10.1016/j.isci.2021.102322.

Baggen, J., Vanstreels, E., Jansen, S., and Daelemans, D. (2021). Cellular host factors for SARS-CoV-2 infection. Nat Microbiol *6*, 1219-1232. 10.1038/s41564-021-00958-0.

Berlansky, S., Sallinger, M., Grabmayr, H., Humer, C., Bernhard, A., Fahrner, M., and Frischauf, I. (2022). Calcium Signals during SARS-CoV-2 Infection: Assessing the Potential of Emerging Therapies. Cells *11*. 10.3390/cells11020253.

Bolger, A.M., Lohse, M., and Usadel, B. (2014). Trimmomatic: a flexible trimmer for Illumina sequence data. Bioinformatics *30*, 2114-2120. 10.1093/bioinformatics/btu170.

Boyle, A.P., Hong, E.L., Hariharan, M., Cheng, Y., Schaub, M.A., Kasowski, M., Karczewski, K.J., Park, J., Hitz, B.C., Weng, S., et al. (2012). Annotation of functional variation in personal genomes using RegulomeDB. Genome Res *22*, 1790-1797. 10.1101/gr.137323.112.

Braga, L., Ali, H., Secco, I., Chiavacci, E., Neves, G., Goldhill, D., Penn, R., Jimenez-Guardeno, J.M., Ortega-Prieto, A.M., Bussani, R., et al. (2021). Drugs that inhibit TMEM16 proteins block SARS-CoV-2 spike-induced syncytia. Nature *594*, 88-93. 10.1038/s41586-021-03491-6.

Brini, M., Cali, T., Ottolini, D., and Carafoli, E. (2013). The plasma membrane calcium pump in health and disease. FEBS J *280*, 5385-5397. 10.1111/febs.12193.

Bruce, J.I.E. (2018). Metabolic regulation of the PMCA: Role in cell death and survival. Cell Calcium *69*, 28-36. 10.1016/j.ceca.2017.06.001.

Brunet, A., Bonni, A., Zigmond, M.J., Lin, M.Z., Juo, P., Hu, L.S., Anderson, M.J., Arden, K.C., Blenis, J., and Greenberg, M.E. (1999). Akt promotes cell survival by phosphorylating and inhibiting a Forkhead transcription factor. Cell *96*, 857-868. 10.1016/s0092-8674(00)80595-4.

Caride, A.J., Penheiter, A.R., Filoteo, A.G., Bajzer, Z., Enyedi, A., and Penniston, J.T. (2001). The plasma membrane calcium pump displays memory of past calcium spikes. Differences between isoforms 2b and 4b. J Biol Chem *276*, 39797-39804. 10.1074/jbc.M104380200.

Chaudhary, J., Walia, M., Matharu, J., Escher, E., and Grover, A.K. (2001). Caloxin: a novel plasma membrane Ca2+ pump inhibitor. Am J Physiol Cell Physiol *280*, C1027-1030. 10.1152/ajpcell.2001.280.4.C1027.

Cheema, P.S., Nandi, D., and Nag, A. (2021). Exploring the therapeutic potential of forkhead box O for outfoxing COVID-19. Open Biol *11*, 210069. 10.1098/rsob.210069.

Chen, X., Cao, R., and Zhong, W. (2019). Host Calcium Channels and Pumps in Viral Infections. Cells *9*. 10.3390/cells9010094.

Cheshenko, N., Trepanier, J.B., Stefanidou, M., Buckley, N., Gonzalez, P., Jacobs, W., and Herold, B.C. (2013). HSV activates Akt to trigger calcium release and promote viral entry: novel candidate target for treatment and suppression. FASEB J *27*, 2584-2599. 10.1096/fj.12-220285.

Chlamydas, S., Papavassiliou, A.G., and Piperi, C. (2021). Epigenetic mechanisms regulating COVID-19 infection. Epigenetics *16*, 263-270. 10.1080/15592294.2020.1796896.

Collazos, J., Domingo, P., Fernandez-Araujo, N., Asensi-Diaz, E., Vilchez-Rueda, H., Lalueza, A., Roy-Vallejo, E., Blanes, R., Raya-Cruz, M., Sanz-Canovas, J., et al. (2022). Exposure to valproic acid is associated with less pulmonary infiltrates and improvements in diverse clinical outcomes and laboratory parameters in patients hospitalized with COVID-19. PLoS One *17*, e0262777. 10.1371/journal.pone.0262777.

Consortium, G.T. (2020). The GTEx Consortium atlas of genetic regulatory effects across human tissues. Science *369*, 1318-1330. 10.1126/science.aaz1776.

Crespi, B., and Alcock, J. (2021). Conflicts over calcium and the treatment of COVID-19. Evol Med Public Health *9*, 149-156. 10.1093/emph/eoaa046.

D'Alterio, G., Lasorsa, V.A., Bonfiglio, F., Cantalupo, S., Rosato, B.E., Andolfo, I., Russo, R., Esposito, U., Frisso, G., Abete, P., et al. (2022). Germline rare variants of lectin pathway genes predispose to asymptomatic SARS-CoV-2 infection in elderly individuals. Genet Med. 10.1016/j.gim.2022.04.007.

Dejos, C., Gkika, D., and Cantelmo, A.R. (2020). The Two-Way Relationship Between Calcium and Metabolism in Cancer. Front Cell Dev Biol *8*, 573747. 10.3389/fcell.2020.573747.

Deniaud, A., Sharaf el dein, O., Maillier, E., Poncet, D., Kroemer, G., Lemaire, C., and Brenner, C. (2008). Endoplasmic reticulum stress induces calcium-dependent permeability transition, mitochondrial outer membrane permeabilization and apoptosis. Oncogene *27*, 285-299. 10.1038/sj.onc.1210638.

Diaz, A., Park, K., Lim, D.A., and Song, J.S. (2012). Normalization, bias correction, and peak calling for ChIP-seq. Stat Appl Genet Mol Biol *11*, Article 9. 10.1515/1544-6115.1750.

Dube, M., Rey, F.A., and Kielian, M. (2014). Rubella virus: first calcium-requiring viral fusion protein. PLoS Pathog *10*, e1004530. 10.1371/journal.ppat.1004530.

Ferrucci, V., de Antonellis, P., Quarantelli, F., Asadzadeh, F., Bibbo, F., Siciliano, R., Sorice, C., Pisano, I., Izzo, B., Di Domenico, C., et al. (2022). Loss of Detection of sgN Precedes Viral Abridged Replication in COVID-19-Affected Patients-A Target for SARS-CoV-2 Propagation. Int J Mol Sci *23*. 10.3390/ijms23041941.

Ferrucci, V., Kong, D.Y., Asadzadeh, F., Marrone, L., Boccia, A., Siciliano, R., Criscuolo, G., Anastasio, C., Quarantelli, F., Comegna, M., et al. (2021). Long-chain polyphosphates impair SARS-CoV-2 infection and replication. Sci Signal *14*. 10.1126/scisignal.abe5040.

Hoffmann, M., Kleine-Weber, H., and Pohlmann, S. (2020). A Multibasic Cleavage Site in the Spike Protein of SARS-CoV-2 Is Essential for Infection of Human Lung Cells. Mol Cell *78*, 779-784 e775. 10.1016/j.molcel.2020.04.022.

Hosseini, A., Hashemi, V., Shomali, N., Asghari, F., Gharibi, T., Akbari, M., Gholizadeh, S., and Jafari, A. (2020). Innate and adaptive immune responses against coronavirus. Biomed Pharmacother *132*, 110859. 10.1016/j.biopha.2020.110859.

Hu, B., Huang, S., and Yin, L. (2021). The cytokine storm and COVID-19. J Med Virol *93*, 250-256. 10.1002/jmv.26232.

Huang, C., Wang, Y., Li, X., Ren, L., Zhao, J., Hu, Y., Zhang, L., Fan, G., Xu, J., Gu, X., et al. (2020). Clinical features of patients infected with 2019 novel coronavirus in Wuhan, China. Lancet *395*, 497-506. 10.1016/S0140-6736(20)30183-5.

Jackson, C.B., Farzan, M., Chen, B., and Choe, H. (2022). Mechanisms of SARS-CoV-2 entry into cells. Nat Rev Mol Cell Biol *23*, 3-20. 10.1038/s41580-021-00418-x.

Khezri, M.R., Varzandeh, R., and Ghasemnejad-Berenji, M. (2022). The probable role and therapeutic potential of the PI3K/AKT signaling pathway in SARS-CoV-2 induced coagulopathy. Cell Mol Biol Lett *27*, 6. 10.1186/s11658-022-00308-w.

Kim, D., Lee, J.Y., Yang, J.S., Kim, J.W., Kim, V.N., and Chang, H. (2020). The Architecture of SARS-CoV-2 Transcriptome. Cell *181*, 914-921 e910. 10.1016/j.cell.2020.04.011.

Krebs, J. (2015). The plethora of PMCA isoforms: Alternative splicing and differential expression. Biochim Biophys Acta *1853*, 2018-2024. 10.1016/j.bbamcr.2014.12.020.

Lai, A.L., Millet, J.K., Daniel, S., Freed, J.H., and Whittaker, G.R. (2017). The SARS-CoV Fusion Peptide Forms an Extended Bipartite Fusion Platform that Perturbs Membrane Order in a Calcium-Dependent Manner. J Mol Biol *429*, 3875-3892. 10.1016/j.jmb.2017.10.017.

Lan, J., Ge, J., Yu, J., Shan, S., Zhou, H., Fan, S., Zhang, Q., Shi, X., Wang, Q., Zhang, L., and Wang, X. (2020). Structure of the SARS-CoV-2 spike receptor-binding domain bound to the ACE2 receptor. Nature *581*, 215-220. 10.1038/s41586-020-2180-5.

Lavezzo, E., Franchin, E., Ciavarella, C., Cuomo-Dannenburg, G., Barzon, L., Del Vecchio, C., Rossi, L., Manganelli, R., Loregian, A., Navarin, N., et al. (2020). Suppression of a SARS-CoV-2 outbreak in the Italian municipality of Vo'. Nature *584*, 425-429. 10.1038/s41586-020-2488-1.

Lee, G.S., Subramanian, N., Kim, A.I., Aksentijevich, I., Goldbach-Mansky, R., Sacks, D.B., Germain, R.N., Kastner, D.L., and Chae, J.J. (2012). The calcium-sensing receptor regulates the NLRP3 inflammasome through Ca2+ and cAMP. Nature *492*, 123-127. 10.1038/nature11588.

Li, H., and Durbin, R. (2010). Fast and accurate long-read alignment with Burrows-Wheeler transform. Bioinformatics *26*, 589-595. 10.1093/bioinformatics/btp698.

Li, H., Handsaker, B., Wysoker, A., Fennell, T., Ruan, J., Homer, N., Marth, G., Abecasis, G., Durbin, R., and Genome Project Data Processing, S. (2009). The Sequence Alignment/Map format and SAMtools. Bioinformatics *25*, 2078-2079. 10.1093/bioinformatics/btp352.

Lukassen, S., Chua, R.L., Trefzer, T., Kahn, N.C., Schneider, M.A., Muley, T., Winter, H., Meister, M., Veith, C., Boots, A.W., et al. (2020). SARS-CoV-2 receptor ACE2 and TMPRSS2 are primarily expressed in bronchial transient secretory cells. EMBO J *39*, e105114. 10.15252/embj.20105114.

Manning, B.D., and Cantley, L.C. (2007). AKT/PKB signaling: navigating downstream. Cell *129*, 1261-1274. 10.1016/j.cell.2007.06.009.

Melms, J.C., Biermann, J., Huang, H., Wang, Y., Nair, A., Tagore, S., Katsyv, I., Rendeiro, A.F., Amin, A.D., Schapiro, D., et al. (2021). A molecular single-cell lung atlas of lethal COVID-19. Nature *595*, 114-119. 10.1038/s41586-021-03569-1.

Minton, K. (2014). Cell migration: Coordinating calcium signalling. Nat Rev Mol Cell Biol *15*, 152. 10.1038/nrm3761.

Muallem, S., Beeker, T., and Pandol, S.J. (1988). Role of Na+/Ca2+ exchange and the plasma membrane Ca2+ pump in hormone-mediated Ca2+ efflux from pancreatic acini. J Membr Biol *102*, 153-162. 10.1007/BF01870453.

Nathan, L., Lai, A.L., Millet, J.K., Straus, M.R., Freed, J.H., Whittaker, G.R., and Daniel, S. (2020). Calcium Ions Directly Interact with the Ebola Virus Fusion Peptide To Promote Structure-Function Changes That Enhance Infection. ACS Infect Dis *6*, 250-260. 10.1021/acsinfecdis.9b00296.

Nieto-Torres, J.L., Verdia-Baguena, C., Jimenez-Guardeno, J.M., Regla-Nava, J.A., Castano-Rodriguez, C., Fernandez-Delgado, R., Torres, J., Aguilella, V.M., and Enjuanes, L. (2015). Severe acute respiratory syndrome coronavirus E protein transports calcium ions and activates the NLRP3 inflammasome. Virology *485*, 330-339. 10.1016/j.virol.2015.08.010.

Okunade, G.W., Miller, M.L., Pyne, G.J., Sutliff, R.L., O'Connor, K.T., Neumann, J.C., Andringa, A., Miller, D.A., Prasad, V., Doetschman, T., et al. (2004). Targeted ablation of plasma membrane Ca2+-ATPase (PMCA) 1 and 4 indicates a major housekeeping function for PMCA1 and a critical role in hyperactivated sperm motility and male fertility for PMCA4. J Biol Chem *279*, 33742-33750. 10.1074/jbc.M404628200.

Pande, J., Szewczyk, M.M., and Grover, A.K. (2011). Allosteric inhibitors of plasma membrane Ca pumps: Invention and applications of caloxins. World J Biol Chem *2*, 39-47. 10.4331/wjbc.v2.i3.39.

Pitt, B., Sutton, N.R., Wang, Z., Goonewardena, S.N., and Holinstat, M. (2021). Potential repurposing of the HDAC inhibitor valproic acid for patients with COVID-19. Eur J Pharmacol *898*, 173988. 10.1016/j.ejphar.2021.173988.

Rabaan, A.A., Al-Ahmed, S.H., Muhammad, J., Khan, A., Sule, A.A., Tirupathi, R., Mutair, A.A., Alhumaid, S., Al-Omari, A., Dhawan, M., et al. (2021). Role of Inflammatory Cytokines in COVID-19 Patients: A Review on Molecular Mechanisms, Immune Functions, Immunopathology and Immunomodulatory Drugs to Counter Cytokine Storm. Vaccines (Basel) *9*. 10.3390/vaccines9050436.

Ritchie, G.R., Dunham, I., Zeggini, E., and Flicek, P. (2014). Functional annotation of noncoding sequence variants. Nat Methods *11*, 294-296. 10.1038/nmeth.2832.

Russo, R., Andolfo, I., Lasorsa, V.A., Cantalupo, S., Marra, R., Frisso, G., Abete, P., Cassese, G.M., Servillo, G., Esposito, G., et al. (2021). The TNFRSF13C H159Y Variant Is Associated with Severe COVID-19: A Retrospective Study of 500 Patients from Southern Italy. Genes (Basel) *12*. 10.3390/genes12060881.

Schultze, J.L., and Aschenbrenner, A.C. (2021). COVID-19 and the human innate immune system. Cell *184*, 1671-1692. 10.1016/j.cell.2021.02.029.

Serebrovska, Z.O., Chong, E.Y., Serebrovska, T.V., Tumanovska, L.V., and Xi, L. (2020). Hypoxia, HIF-1alpha, and COVID-19: from pathogenic factors to potential therapeutic targets. Acta Pharmacol Sin *41*, 1539-1546. 10.1038/s41401-020-00554-8.

Sette, A., and Crotty, S. (2021). Adaptive immunity to SARS-CoV-2 and COVID-19. Cell *184*, 861-880. 10.1016/j.cell.2021.01.007.

Shang, J., Wan, Y., Luo, C., Ye, G., Geng, Q., Auerbach, A., and Li, F. (2020). Cell entry mechanisms of SARS-CoV-2. Proc Natl Acad Sci U S A *117*, 11727-11734. 10.1073/pnas.2003138117.

Shihab, H.A., Gough, J., Cooper, D.N., Stenson, P.D., Barker, G.L., Edwards, K.J., Day, I.N., and Gaunt, T.R. (2013). Predicting the functional, molecular, and phenotypic consequences of amino acid substitutions using hidden Markov models. Hum Mutat *34*, 57-65. 10.1002/humu.22225.

Stefanetti, R.J., Voisin, S., Russell, A., and Lamon, S. (2018). Recent advances in understanding the role of FOXO3. F1000Res *7*. 10.12688/f1000research.15258.1.

Tay, M.Z., Poh, C.M., Renia, L., MacAry, P.A., and Ng, L.F.P. (2020). The trinity of COVID-19: immunity, inflammation and intervention. Nat Rev Immunol *20*, 363-374. 10.1038/s41577-020-0311-8.

Thompson, M.G., Larson, M., Vidrine, A., Barrios, K., Navarro, F., Meyers, K., Simms, P., Prajapati, K., Chitsike, L., Hellman, L.M., et al. (2015). FOXO3-NF-kappaB RelA Protein Complexes Reduce Proinflammatory Cell Signaling and Function. J Immunol *195*, 5637-5647. 10.4049/jimmunol.1501758.

V'Kovski, P., Kratzel, A., Steiner, S., Stalder, H., and Thiel, V. (2021). Coronavirus biology and replication: implications for SARS-CoV-2. Nat Rev Microbiol *19*, 155-170. 10.1038/s41579-020-00468-6.

Walls, A.C., Park, Y.J., Tortorici, M.A., Wall, A., McGuire, A.T., and Veesler, D. (2020). Structure, Function, and Antigenicity of the SARS-CoV-2 Spike Glycoprotein. Cell *183*, 1735. 10.1016/j.cell.2020.11.032.

Wrapp, D., Wang, N., Corbett, K.S., Goldsmith, J.A., Hsieh, C.L., Abiona, O., Graham, B.S., and McLellan, J.S. (2020). Cryo-EM Structure of the 2019-nCoV Spike in the Prefusion Conformation. bioRxiv. 10.1101/2020.02.11.944462.

Xie, M., and Chen, Q. (2020). Insight into 2019 novel coronavirus - An updated interim review and lessons from SARS-CoV and MERS-CoV. Int J Infect Dis *94*, 119-124. 10.1016/j.ijid.2020.03.071.

Xin, Z., Ma, Z., Hu, W., Jiang, S., Yang, Z., Li, T., Chen, F., Jia, G., and Yang, Y. (2018). FOXO1/3: Potential suppressors of fibrosis. Ageing Res Rev *41*, 42-52. 10.1016/j.arr.2017.11.002.

Zhang, Z., Convertini, P., Shen, M., Xu, X., Lemoine, F., de la Grange, P., Andres, D.A., and Stamm, S. (2013). Valproic acid causes proteasomal degradation of DICER and influences miRNA expression. PLoS One *8*, e82895. 10.1371/journal.pone.0082895.

Zhou, Y., Frey, T.K., and Yang, J.J. (2009). Viral calciomics: interplays between Ca2+ and virus. Cell Calcium *46*, 1-17. 10.1016/j.ceca.2009.05.005.

Supplemental Informations

Targeting ATP2B1 impairs PI3K/Akt/Fox-O3 signaling and reduces SARS-COV-2 replication *in vivo*.

Pasqualino de Antonellis[1,2*], Veronica Ferrucci [1,2*], Francesca Bibbo [1,2$], Fathemeh Asadzadeh[1-2$], Francesca Gorini[2], Angelo Boccia[1,2], Carmen Sorice[1,2], Roberto Siciliano[1], Roberta Russo[1,2], Immacolata Andolfo[1,2], Vito Alessandro Lasorsa[1,2], Sueva Cantalupo[1,2], Giovanni Paolella[1,2], Giovanna Fusco[3], Maurizio Viscardi[3], Sergio Brandi[3], Bianca Maria Pierri[3], Pellegrino Cerino[3], Vittoria Monaco[1,4], Dong-Rac choi[5,6], Jae-Ho Cheong[6], Maria Monti[1,4], Achille Iolascon[1,2], Stefano Amente[2], Mario Capasso[1,2], Hong-Yeoul Kim[6#] and Massimo Zollo[1,2,7,8#]

1 CEINGE Biotecnologie Avanzate, Naples, 80145, Italy

2 Dipartimento di Medicina Molecolare e Biotecnologie Mediche (DMMBM), 'Federico II' University of Naples, Naples, 80131, Italy

3 Istituto Zooprofilattico Sperimentale del Mezzogiorno, Naples, 80055, Italy

4 Department of Chemical Sciences, University 'Federico II' University of Naples, Naples 80125, Italy.

5 Department of Surgery, Yonsei University College of Medicine, Seoul, Korea

6 HAIM BIO Co. Ltd, Industrial Park, Korea University, Seoul, South Korea

7 DAI Medicina di Laboratorio e Trasfusionale, 'Federico II' University of Naples, 80131 Naples, Italy

8 Lead contact

(*) co-first

($) co-second

(#) corresponding authors

Correspondence:
massimo.zollo@unina.it (M.Z.)
hykim@haimbio.com (H.Y.K.)

Supplementary Figure S1

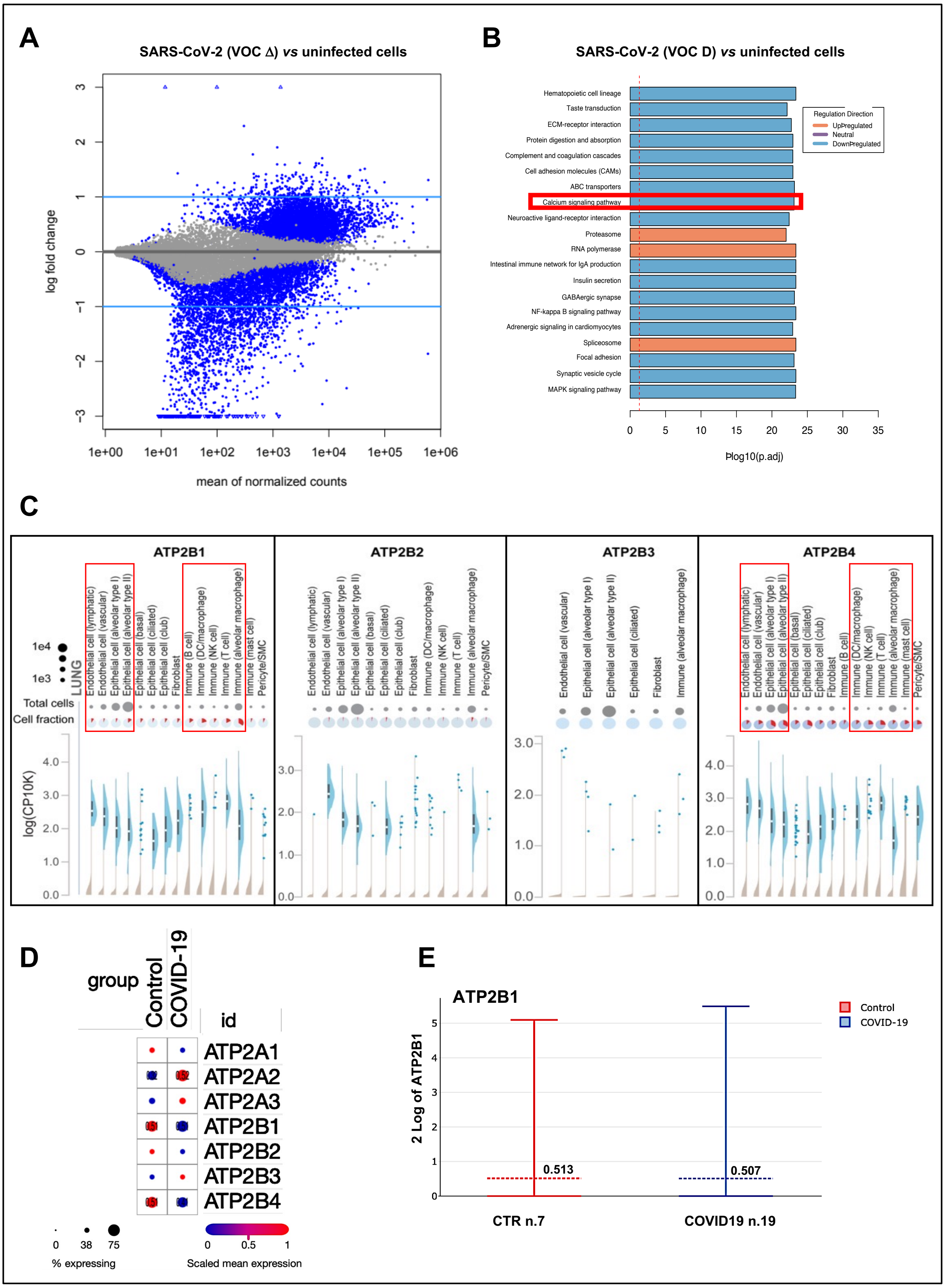

Figure S1. Ca2+ pumps, including ATP2B1, expression are deregulated during SARS-CoV-2 infection. Related to Figure 1.

(A) RNA Sequencing (RNA-seq) analyses was performed in HEK293T-ACE2 cells infected by SARS-CoV-2 (VOC Delta, 0.026 MOI for 24 hours). The mean of normalized cound here shown to get an overview over similarities and dissimilarities between SARS-CoV-2-infected non infected cells. The analysis of the transcriptional changes in gene transcripts identified 234 up-regulated and 1742 down-regulated genes in SARS-CoV-2-infected cells compared to not-infected cells as differentially expressed (i.e., DEG). **(B)** The Gene Set Enrichment Analysis (GSEA) was then applied for the identification of deregulated key genes and pathways. In total, 234 up-regulated and 1742 down-regulated genes in SARS-CoV-2-infected cells compared to not-infected cells were mapped to KEGG pathways ($P < 0.05$). The sorted terms by P-value ($P < 0.05$) are shown. KEGG pathway enrichment analysis indicate those significant deregulated genes were highly clustered in calcium signaling pathway (red box). P adj: adjusted P-values. **(C)** In silico analysis of publicly available data sets of single-cell RNA sequencing (https://singlecell.broadinstitute.org) for the expression of the plasma membrane calcium ATPases members of the large family of type Calcium ion pumps (PMCAs or ATP2B1-4) in multiple cell type in the lung parenchyma (including alveolar macrophages and in the alveolar epithelial cells type I and type II). **(D)** Literature public search on available datasets obtained from a single-nuclei RNA-seq (snRNA-seq) on >116,000 nuclei from n.19 COVID-19 autopsy lungs and n.7 pre-pandemic controls (Melms et al., 2021); https://singlecell.broadinstitute.org/single_cell/study/SCP1052/covid-19-lung-autopsy-samples) to verify if PMCAs and SERCAs pumps (ATP2B1-4 and ATP2A1-3 genes, respectively) showed distinct fractional and dysfunctional changes across the lungs from COVID-19 decedents. **(e)** Expression levels of ATP2B1 in single-nuclei RNA-seq (snRNA-seq) analyses performed on >116,000 nuclei from n.19 COVID-19 autopsy lungs and n.7 pre-pandemic controls (Melms *et al.*, 2021); https://singlecell.broadinstitute.org/single_cell/study/SCP1052/covid-19-lung-autopsy-samples).

Supplementary Figure S2

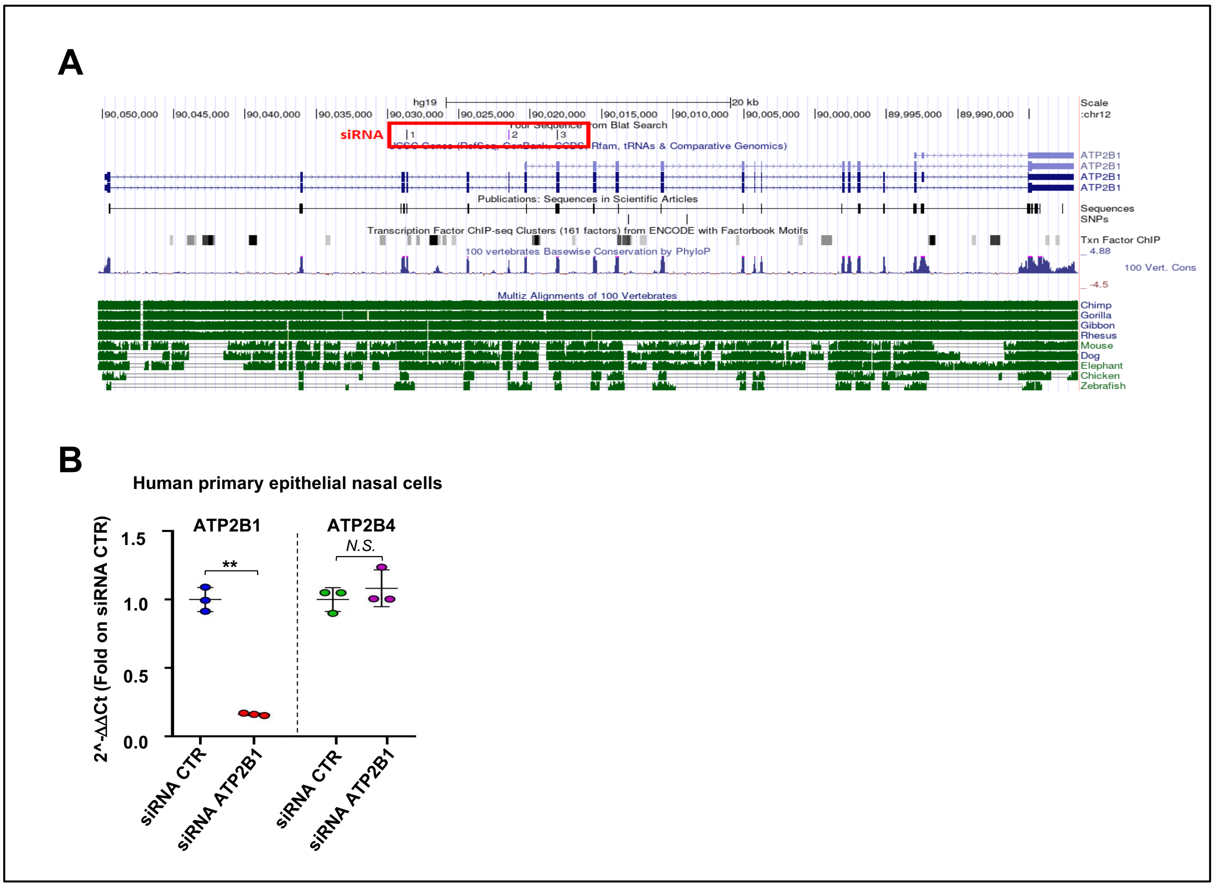

Figure S2. ATP2B1 reduced protein amount promotes SARS-CoV-2 replication. Related to Figure 2.

(A) Representation of human ATP2B1 region recognized by siRNA as reported in the UCSC Genome Browser on Human Dec. 2013 (GRCh38/hg38) Assembly (https://genome.ucsc.edu/). At the bottom, the alignment of this genomic region among different species is shown. **(B)** Quantification of mRNA abundance relative to that in control (CTR) cells ($2^{-\Delta\Delta Ct}$) for ATP2B1 and ATP2B4. RT-PCR analysis of RNA extracted from human primary epithelial nasal cells downregulating PMCA (after 48 hours from transfection with the ATP2B1 siRNA). Cells overexpressing a pool of three siRNA control were used as negative control of the experiment. Data are means ± SD. ** $p < 0.01$,; NS, not statistic (unpaired two-tailed student's t test; N = 3 independent experiments per group

Supplementary Figure S3

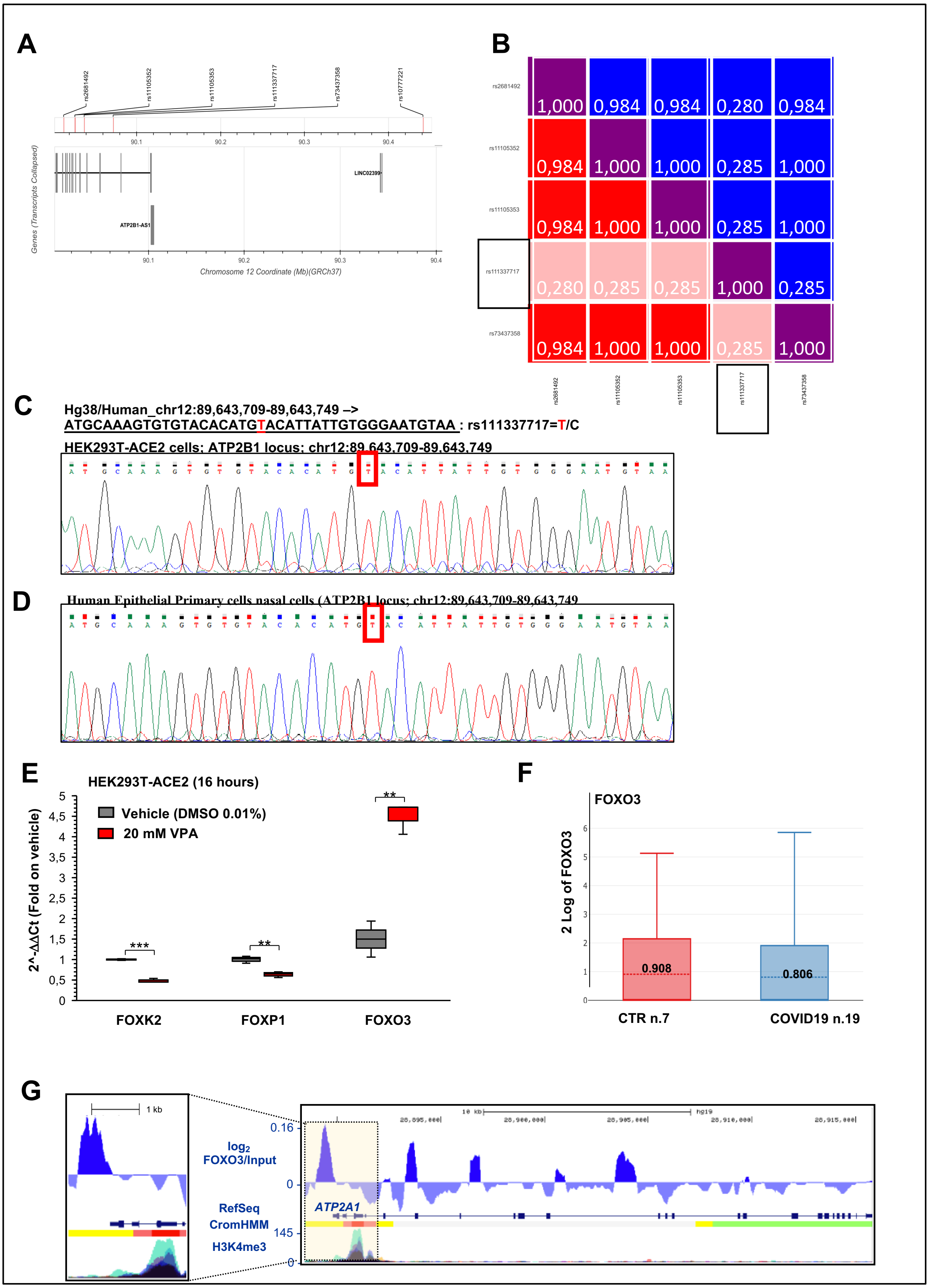

Figure S3. The homozygous intronic variant rs11337717 in ATP2B1 locus is responsible for SARS-CoV-2 increased replication in COVID19 patients. Related to Figure 3.

(A, B) Linkage disequilibrium (LD) analyses on the top 5 SNPs (rs11105352; rs11105353; rs73437358; rs111337717; rs2681492) in order to select those independent. The SNP rs10777221 was excluded from this analyses because located at most 5' region in extragenic ATP2B1 locus region (**A**). The graph in (**B**) shows the only SNP not in LD is rs111337717 (black boxes). **(C)** Sanger sequencing of the genomic region of ATP2B1 locus (chr12:89,643,709-89,643,749) in HEK293T-ACE2 cells to exclude the presence of intronc variance potentially responsible for alterated transcriptional levels of ATP2B1 gene. The red box indicate the nucleotide wild type allele for the SNP here studied. **(D)** Sanger sequencing of the genomic region of ATP2B1 locus (chr12:89,643,709-89,643,749) in human primary epithelial nasal cells to exclude the presence of intronic variants potentially responsible for alterated transcriptional levels of ATP2B1 gene. **(E)** Quantification of mRNA abundance relative to that in control (CTR) cells ($2^{-\Delta\Delta Ct}$) for FOXK2, FOXP1 and FOXO3 genes. RT-PCR analysis of RNA extracted from HEK293T-ACE2 cells treated with 20 mM valproc acid (VPA) for 16 hours or 0.01% DMSO as vehicle control. Data are means ± SD. ** $p<0.01$, ***$P<0.001$ (unpaired two-tailed student's t test; N = 3 independent experiments per group). **(F)** Expression levels of FOXO3 in single-nuclei RNA-seq (snRNA-seq) analyses performed on >116,000 nuclei from n.19 COVID-19 autopsy lungs and n.7 pre-pandemic controls (Melms *et al.*, 2021). **(G)** Genome browser screenshots showing accumulation of normalized FOXO3 signal, together with CromHMM state segmentation and H3K4me3 signal (ENCODE), along the ATP2A1 gene in human cells. ForCromHMM state segmentation colors indicate: Bright Red – Promoter; Orange and yellow - enhancer; Green - Transcriptional transition. The expanded view of the highlighted region, on the left, shows FOXO3 peaks over ATP2A1 enhancer regions, as marked by yellow region of CromHMM.

Supplementary Figure S4

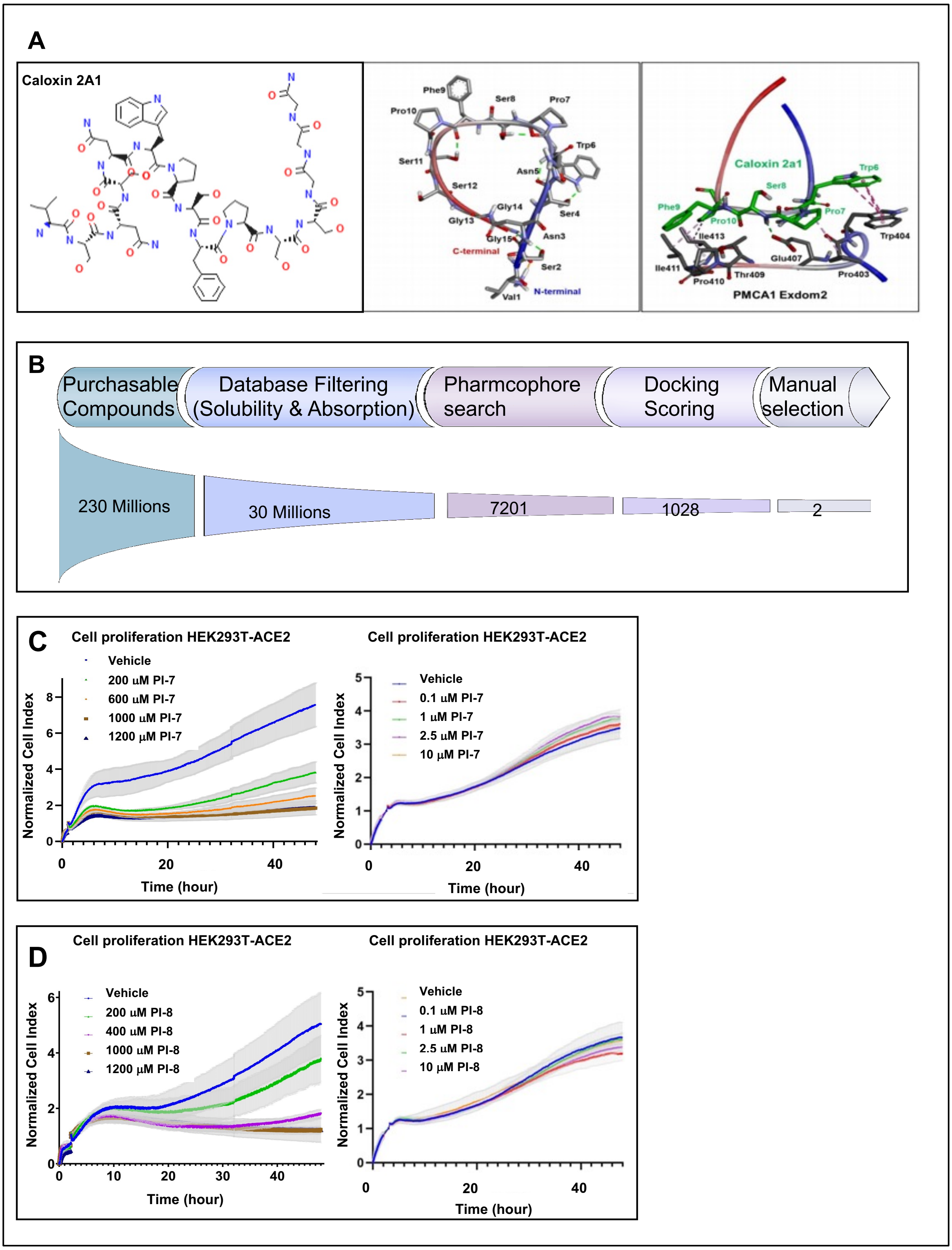

Figure S4. ATP2B1 impairment via Caloxin-derivative (PI-7) molecule. Related to Figure 4.

(A) On the left: The sequence of caloxin2a1 sequence, as peptide, is shown. **On the right:** The molecular modeling of ATP2B1-caloxin2a1 structure by docking and energy minimization modeling via artificial intelligence as a drug design computational tool is shown. The pharmacophore model by using the structures ATP2B1-exodom-2 and caloxin 2a1 is also shown. Five pharmacophore features were produced. **(B)** The scheme of the pipeline of drug discovery are shown. Among 230 million purchasable compounds, 30 million molecules were selected by considering database filtering for solubility and absorption, 7,201 molecules by pharmacophore search, and 1028 molecules by docking scoring. The top 22 molecules were manually selected. Finally, two molecules were chosen. **(C, D)** Real-time cell proliferation analyses for the Cell Index (i.e., the cell-sensor impedance was expressed every two minutes as a unit called "Cell Index"). HEK293T-ACE2 were plated and, after two hours, treated with the indicated concentrations (escalating doses) of PI-7 **(C)** or PI-8 **(D)**; with vehicle-treated cells were the negative control. Impedance was measured every 2 min over 48 hours. The graphs showing "normalized cell index" were generated using Graph Pad Prism 9.

Supplementary Figure S5

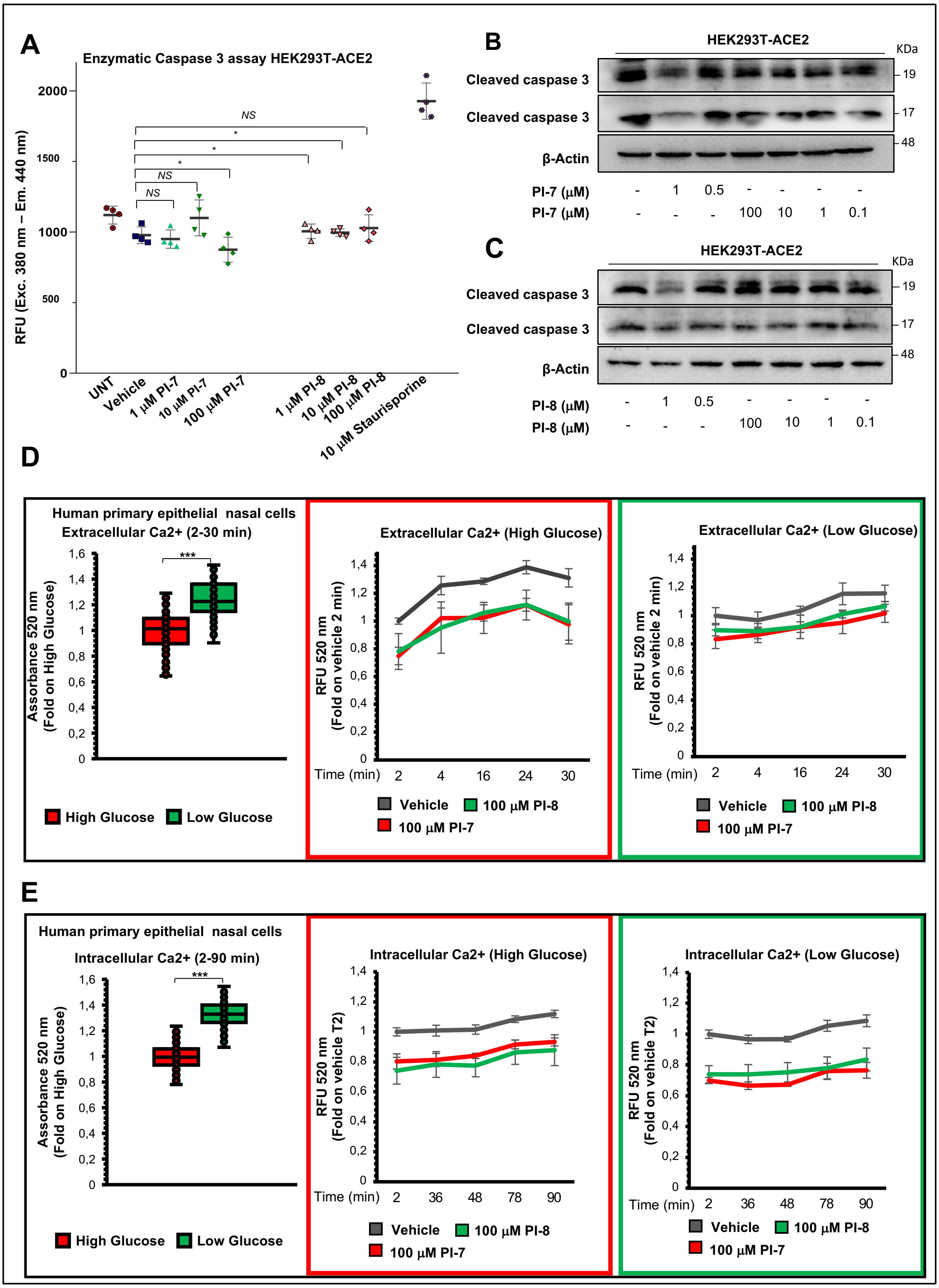

Figure S5. ATP2B1 impairment via Caloxin-derivative (PI-7) molecule diminishes extracellular and intracellular Ca^{2+} levels. Related to Figure 4.

(A) Caspase 3 activity measured in HEK293T-ACE2 cells ($5x10^5$ cells/well in a 24-well plate and incubated overnight) treated with increasing concentrations of compound PI-7 and PI-8 for 18 hours. Vehicle-treated cells and cells treated with 10 μM staurosporine were used as negative and positive controls, respectively. Data are presented as relative fluorescent units (RFUs; excitation: 380 nm; emission: 460 nm) measured after 1 hour of incubation (T1h). Data are means ± SD. $*P < 0.05$; N.S., nonsignificant (as determined by unpaired two-tailed Student's *t* test; n = three independent experiments per group). **(B, C)** Representative immunoblotting analyses on total protein lysates obtained from HEK293T-ACE2 treated with escalating doses of PI-7 **(B)** and PI-8 **(C)** molecules using antibodies against the indicated proteins. β-Actin was used as the loading control. Vehicle-treated cells (i.e., 0.001% DMSO) are used as negative control of the experiment. All experiments were performed in triplicate. **(D) On the left:** Extracellular Ca^{2+} as measured using Fluo3-AM over 30 min in human primary epithelial nasal cells (1.2×10^4 cells/well) plated in DMEM High Glucose or DMEM Low glucose for 24 hours. Data are means ± SD. ***P<0.001 (unpaired two-tailed student's t test; N = 3 independent experiments per group). **On the right:** Extracellular Ca^{2+} as measured using Fluo3-AM over 30 min in human primary epithelial nasal cells (1.2×10^4 cells/well) plated in DMEM High Glucose or DMEM Low glucose and treated with 100 μM compounds PI-7 and PI-8, or with 0.001% DMSO as vehicle. After 24 hours from the treatment started, the cell media supernatant was used for the extracellular Ca^{2+} measurement. The graph shows quantification of relative fluorescence changes of Fluo3 as a measure of extracellular Ca^{2+} levels by showing the relative fluorescent units (RFUs) (excitation, 506 nm; emission, 526 nm) recorded for 30 min by using a multimode plate reader (Enspire 2300, PerkinElmer). Red box: High Glucose; Green Box: Low glucose. Data are means ±SD of three independent experiments. **(E) On the left:** Intracellular Ca^{2+} as measured using Fluo3-AM over 90 min in human primary epithelial nasal cells (1.2×10^4 cells/well) plated in DMEM High Glucose or DMEM Low glucose for 24 hours. Data are means ± SD. ***P<0.001 (unpaired two-tailed student's t test; N = 3 independent experiments per group). **On the right:** Intracellular Ca^{2+} as measured using Fluo3-AM over 90 min in human primary epithelial nasal cells (1.2×10^4 cells/well) plated in DMEM High Glucose or DMEM Low glucose and treated with 100 μM compounds PI-7 and PI-8, or with 0.001% DMSO as vehicle. After 24 hours from the treatment started, the cells were used for the intracellular Ca^{2+} measurement. The graph shows quantification of relative fluorescence changes of Fluo3 as a measure of intracellular Ca^{2+} levels by showing the relative fluorescent units (RFUs) (excitation, 506 nm; emission, 526 nm) recorded for 90 min by using a multimode plate reader (Enspire 2300, PerkinElmer). Red box: High Glucose; Green Box: Low glucose. Data are means ±SD of three independent experiments.

Supplementary Figure S6

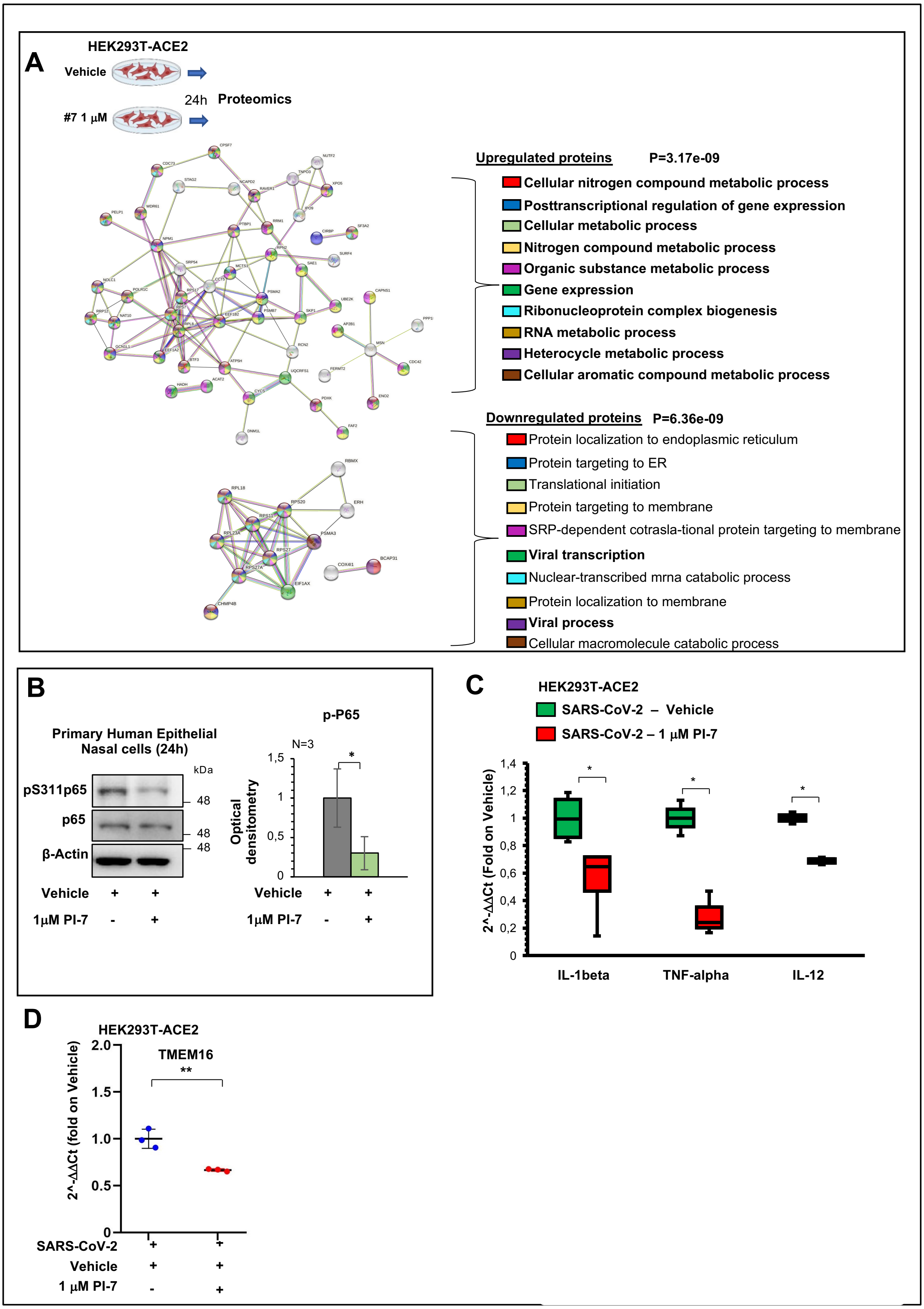

Figure S6. ATP2B1 impairment via Caloxin-derivative (PI-7) molecole diminishes SARS-CoV-2 propagation and syncytia formation. Related to Figures 5.

(A) Proteomic assay based on LC-MS/MS approach performed on HEK-293T-ACE2 cells treated with PI-7 molecule (1 μM) for 24 hours. **On the top:** A protein interaction network was generated using the Search Tool for the Retrieval of Interacting Genes/ Proteins (STRING) database (https://string-db.org) by using only those proteins found upregulated in PI-7-treated cells (i.e., n.66 upregulated protein). **On the bottom:** A protein interaction network was generated using the Search Tool for the Retrieval of Interacting Genes/ Proteins (STRING) database (https://string-db.org), using only those proteins that were downregulated in PI-7-treated cells (i.e., 18 downregulated proteins). Among the pathways in which these downregulated proteins are involved, there were "viral process" and "viral transcription" (in bold). **(B)** Representative immunoblotting analysis using antibodies against the indicated proteins on total protein lysates obtained from HEK293T-ACE2 treated with compound PI-7 (1 μM) for 24 hours. All experiments were performed in triplicate. Densitometry analysis of the indicated band intensities in blots from three independent experiments. Data are means ±SD. * $p < 0.05$ (unpaired two-tailed student's t-tests; N = 3 independent experiments per group). **(C)** Quantification of mRNA abundance relative to that in control (CTR) cells (2−ΔΔCt) for IL-1beta, TNF-alpha and IL-12 genes. RT-PCR analysis of RNA extracted from HEK293T-ACE2 cells infected with SARS-CoV-2 (VOC Delta, 0.026 MOI for 72 hours) and treated with 1 μM PI-7 molecule or 0.001% DMSO as vehicle control. Data are means ± SD. * $p<0.01$ (unpaired two-tailed student's t test; N = 3 independent experiments per group). **(D)** Quantification of mRNA abundance relative to that in control (CTR) cells ($2^{-\Delta\Delta Ct}$) for human TMEM16 gene. RT-PCR analysis of RNA extracted from HEK293T-ACE2 cells treated as in (A). Data are means ± SD. * $p < 0.05$ (unpaired two-tailed student's t test; N = 3 independent experiments per group).

Supplementary Tables

Table S1: Differentially expressed genes (DEGs) upon SARS-CoV-2 early infection in HEK-293T-ACE2 taking part to Calcium Signalling.

The genes taking part to "Calcium signalling" in REACTOME pathway enrichment analysis of those differentially expressed genes (DEGs) from RNAseq analyses performed in HEK293T-ACE2 cells infected with SARS-CoV-2 (VOC Delta, 24hours) vs untreated cells. N.157 genes statistically deregulated by SARS-CoV-2 after 24 hours involved in Calcium signalling were found. The gene name, the baseMean (the average of the normalized count values), the log2FoldChange, the lfcSE (standard error value), the pValue and the adjusted p values (i.e., padj) are listed. In red, the membrane and endoplasmic reticulum Ca2+ pumps (i.e., ATP2Bs and ATP2As).

Gene name	BaseMean	Log2FoldChange	lfcSE	pValue	pAdj
EGF	470.066.492.265.217	-40.619.336.960.114	0.664028018529976	7,08E+03	1,05E+05
CAMK1G	364.858.544.902.485	-340.754.771.922.581	0.913198249232395	8,34E+08	5,08E+09
TNNC2	201.384.809.825.337	-316.776.580.773.799	125.621.979.502.456	0.000426075476689886	0.00177089604329882
KDR	447.921.773.022.525	-291.789.785.352.181	0.690679824706131	1,20E+08	8,54E+08
PTGER3	2.631.393.772.017	-259.177.710.593.284	0.807666047432124	6,24E+09	0.000316375821514552
CACNA1I	869.350.624.213.802	-245.646.245.246.643	0.413068357989845	1,64E+04	2,27E+05
FGF19	595.183.107.293.085	-24.348.301.365.875	0.498409657835589	6,06E+06	5,46E+07
ATP2B2	270.270.787.313.473	-22.332.018.924.914	0.766386590862842	0.000168310855505058	0.000771084907017115
MYLK4	359.196.817.041.812	-218.249.512.123.712	0.653358723896032	4,44E+09	0.000231472468385037
CACNA1G	945.542.009.013.953	-193.464.303.503.756	0.183028207937104	2,77E-13	3,38E-12
NTRK3	280.665.734.128.966	-191.862.731.213.666	0.798849668970072	0.000742655141446291	0.00289573206235725
AVPR1A	486.965.123.732.544	-18.995.518.921.901	0.577352080972861	5,66E+09	0.00028951664775388
RYR2	163.422.835.354.659	-189.620.200.301.431	0.315137422842955	1,23E+04	1,74E+05
PRKCG	549.075.446.715.279	-177.755.730.324.405	0.188372347832613	3,09E-09	2,15E-06
RYR1	809.194.404.057.114	-169.311.919.230.691	0.486468803564657	3,24E+08	0.000174489336118528
PDGFRB	324.832.730.647.174	-166.275.196.192.471	0.771626078491638	0.00147511758120898	0.00532287697789966
NGF	301.570.589.660.459	-15.325.074.691.358	0.745790834556926	0.0020175651560619	0.00702354442142255
FGF18	298.564.044.685.259	-148.439.847.088.366	0.828292832261265	0.00337210418608626	0.0110347633464023
CALML6	490.099.528.433.961	-131.370.510.943.569	0.825860210839343	0.00533449786994513	0.0164946648727855
GRIN1	157.108.717.534.577	-128.763.563.304.787	0.323378819942514	6,46E+08	4,02E+09

NTRK2	262.623.726.884.291	-128.054.971.330.727	0.243831076403219	1,58E+06	1,58E+07
NTRK1	578.235.945.050.576	-12.596.871.921.419	0.551982314520049	0.00162927852165569	0.00581799505388285
GDNF	558.396.367.605.257	-125.541.837.244.765	0.531587287153423	0.00137309343890679	0.00500164697395093
PHKG1	399.138.091.587.535	-122.304.443.526.309	0.632694503323343	0.00358227204856374	0.0116168708830677
PTGFR	276.774.110.594.092	-116.245.612.041.348	0.826887731548613	0.00858417601832968	0.0248084910809525
ADRB2	103.466.364.639.335	-115.829.451.291.408	0.424783537150509	0.000598915194250 65	0.0023882746914971
ATP2A1	203.108.013.385.034	-107.280.686.165.945	0.262329863906071	5,49E+08	3,46E+09
ERBB4	170.776.039.723.201	-104.381.160.003.265	0.300596363974115	6,48E+09	0.00032742177194106
CACNA1C	393.319.540.235.024	-102.106.063.979.435	0.192751646909679	1,72E+06	1,71E+07
ADRA1B	591.447.672.206.431	-101.281.999.512.882	0.511038582291448	0.00457889299727663	0.0144293335681128
SLC8A3	95.692.745.140.642	-0.998473384007727	0.410221783240345	0.00169667248287767	0.00602970050421849
PLCB4	853.137.293.137.909	-0.980318301180731	0.140257942056366	4,46E+01	9,22E+02
HRH1	274.954.013.122.704	-0.960466468918194	0.835252217871031	0.0151214999321587	0.0400493571921168
P2RX2	210.012.518.949.649	-0.906096933837229	0.255316025097521	6,31E+09	0.000319747150885531
CACNA1B	420.417.802.824.201	-0.887883543343921	0.188611910026867	4,54E+07	3,47E+07
GRIN2C	134.980.629.604.766	-0.861218744558696	0.31162870962008	0.000932072365025747	0.00354992600479506
SLC8A2	273.654.190.588.128	-0.858567119679333	0.237358375185696	5,37E+08	0.000275901884465897
MST1	588.954.201.846.589	-0.829615004504173	0.243875246591338	0.000125608272597485	0.000592232918411347
MCOLN3	165.355.435.122.002	-0.827337601316473	0.128096033644867	2,26E+03	3,64E+04
PDGFB	116.038.571.818.564	-0.802905099711672	0.413428970321733	0.00785763338500944	0.0230062180714721
PLCD1	606.706.213.146.116	-0.73419217381745	0.211338432292575	0.000128480351249161	0.000604624576401611
PTAFR	148.429.292.120.027	-0.718467868052912	0.305326705403937	0.00398084691805461	0.0127481951469379
SPHK1	425.399.369.213.307	-0.707202397121825	0.201780650419755	0.000116061152317301	0.000552590774509452
ADRB1	655.653.614.469.463	-0.679205605810754	0.472803117372689	0.025791562973466	0.0629923986317459
FLT1	700.355.766.267.359	-0.669898202668207	0.185104262705454	8,28E+09	0.000409305590749802
AGTR1	114.530.552.323.422	-0.656048536313823	0.390155781513432	0.0194109134979577	0.049664781084052
TPCN1	252.604.797.979.172	-0.600289817556319	0.132545750778705	2,04E+07	1,39E+09
PHKA2	175.224.737.675.515	-0.561183955695007	0.120614441069424	1,27E+08	8,99E+08
FGF2	107.171.213.660.927	-0.52864644155335	0.131546499596881	2,52E+09	0.000138420306528569
ERBB3	120.866.178.420.076	-0.526562320203576	0.13331201305227	3,35E+09	0.000179921804431245
CACNA1D	336.171.601.170.013	-0.513843498616443	0.231116856688361	0.0101629928909175	0.0285960922734542
FGF9	481.838.217.511.183	-0.440316618339933	0.201003686986393	0.0138044691557052	0.0370226603357302
ITPR3	544.035.684.154.367	-0.436844916967323	0.0858936274580685	2,85E+07	2,25E+07
BDKRB2	432.395.097.685.611	-0.433653663001909	0.497631594097063	0.0986511036863904	0.187638940694549
SLC8A1	522.452.995.997.531	-0.425640845179831	0.209128356637808	0.0207771460712456	0.0526173559586334
PDE1B	289.070.207.499.701	-0.410559888941243	0.206926593742145	0.0245441014890181	0.0604941914017028

VEGFA	297.506.769.867.281	-0.405780412554488	0.142594980006681	0.00247420124223248	0.00837757964418323
FGF5	79.709.394.383.223	-0.399984899482115	0.356896301574514	0.108219512397703	0.201880061965315
ATP2B4	283.800.562.649.639	-0.394169016228452	0.126855884293042	0.00112236419580121	0.00418746949373256
RET	577.232.271.862.126	-0.353170332880125	0.170689077431222	0.0239340673097788	0.0592338298112563
PDGFA	579.364.106.716.877	-0.322941855478592	0.173196187829469	0.0411391142990746	0.0926751594433211
CCKBR	126.784.008.566.849	-0.320952603632085	0.304055604871576	0.161838087141715	0.276984470866739
LTB4R2	189.584.854.807.253	-0.313758791468503	0.26937952269752	0.146164169708267	0.255529602755143
MCOLN2	113.978.857.145.436	-0.301788122475556	0.137806208277608	0.0203855557780396	0.0517490197933601
PRKCB	25.235.847.386.427	-0.29501851474154	0.109946339948008	0.00539312477447984	0.0166518138449238
CAMK2B	772.906.926.209.551	-0.283029002203993	0.145730810888778	0.0383029245794291	0.0874986769446822
PDGFRA	109.866.805.847.052	-0.282309320967817	0.2972729826783	0.211044616859362	0.340490350351324
CHRM3	560.839.356.409.002	-0.251888870437173	0.160119800958921	0.088376618755959	0.1719817480213
FGF17	16.496.815.745.705	-0.248096374729555	0.249482103006665	0.227384140460309	0.359420066595756
ADCY7	599.531.283.129.749	-0.242677303099414	0.155103300744442	0.0923579071335468	0.178067513485704
HTR6	354.992.109.224.363	-0.236382187781594	0.198583734709514	0.179234191122456	0.300143455269253
NOS2	382.743.199.985.029	-0.216942472653685	0.216414799478264	0.246028914267307	0.382173021389535
CAMK1D	115.738.679.551.248	-0.20243741585522	0.144915532772324	0.1364996988295	0.242143975557365
PTK2B	3.347.654.773.982	-0.198541912471893	0.198825455813247	0.259322322212717	0.397481473680127
PLCG2	128.718.181.153.958	-0.146004446908614	0.133411235660135	0.248733561997342	0.385274541913544
CALML4	720.412.591.192.242	-0.142650941830901	0.163982197735486	0.344385374689041	0.489805705022451
OXTR	148.277.035.788.061	-0.141149910723466	0.274436307642278	0.508031589930453	0.648622564287605
CHRNA7	489.354.993.796.243	-0.137351331277486	0.16799105529875	0.373336159701828	0.519360460101477
ITPR1	194.448.959.208.382	-0.130765692109194	0.135837801130851	0.309257090522638	0.45335357342098
PHKA1	179.591.123.826.724	-0.125547564416148	0.103400902226699	0.210340488576319	0.339696463309899
ADORA2A	223.762.626.919.609	-0.106559430507992	0.419538375673638	0.476481309897874	0.620376663464722
PLCG1	699.101.491.751.449	-0.104642450208333	0.0865004261930556	0.215520564598944	0.345427330349358
FGFR4	208.232.993.177.581	-0.101715568146048	0.102865746174184	0.308028355572787	0.452073453570876
FGFR1	499.106.216.692.943	-0.0923093100011115	0.0949481980581863	0.304396825481386	0.448217896866103
PHKG2	314.206.921.479.836	-0.0911508288462413	0.124077121364634	0.44208383855371	0.587814337568264
ADCY9	235.254.942.195.309	-0.0837295765189726	0.0974106513943221	0.376355915316127	0.522388753677872
FGF8	464.562.300.432.542	-0.0761848939011496	0.353716413037013	0.713462371093803	0.813931531496335
ATP2B3	587.586.125.763.348	-0.0626210328757565	0.439048123471953	0.0738189363850452	0.14885884758557
CXCR4	122.446.292.826.757	-0.0603388356624955	0.143329518789903	0.655120311029227	0.76759630744944
PLCB1	994.674.848.651.785	-0.0589275381309039	0.14056687275296	0.656669719144886	0.768689888118064
MST1R	165.032.670.287.062	-0.0494471966447024	0.245291459692777	0.802995262899111	0.878339556478466
CAMK4	891.013.810.454.115	-0.0452814478563072	0.177434779926719	0.778334345320621	0.861379840200812

STIM2	95.701.248.136.539	-0.0390808211180951	0.140900346772734	0.76820715039287	0.854282496755984
PLCE1	107.195.402.497.356	-0.0341801457720718	0.145079723037892	0.801377847150615	0.87713678071911
ITPKC	70.396.087.492.243	-0.0284050996316445	0.143515642077651	0.835382348472484	0.901049822420575
ADCY1	190.640.441.243.435	-0.0234347315901111	0.129135611085778	0.848319232392113	0.909983793161546
PPP3CC	594.164.875.490.275	-0.0217191364607527	0.151752406462586	0.877965754946522	0.929456415592496
ATP2A3	57.861.264.377.674	-0.0129319930116038	0.154240920271403	0.926149963731589	0.958988807760499
CACNA1H	345.963.329.850.669	-0.0119216426741543	0.105863576682641	0.924981441177746	0.958205598411089
GRIN2D	787.806.074.900.388	-0.00313600612645953	0.165848797099175	0.982047635092185	0.988873258407805
ORAI3	669.964.822.841.849	-0.0029585841913774	0.154784193674808	0.980434132269063	0.987886621158221
PRKACA	511.052.546.711.711	8,08E+09	0.0944525021842156	0.992207464272	0.995423498362367
MYLK	499.839.296.301.556	0.00232286697512634	0.18351714058263	0.990738415795618	0.99448260200729
FLT4	409.216.446.721.523	0.0279541004301016	0.0953640134258976	0.785110815522244	0.865849292306412
ITPR2	185.378.863.744.044	0.02851082365659	0.141313453931377	0.830830585455922	0.898094050005188
MYLK3	403.912.378.245.326	0.037299870072606	0.345347448460966	0.861313219529031	0.918180856193811
PRKCA	370.983.476.105.691	0.0516584120737146	0.124335893152742	0.665347986001177	0.776105971436831
ASPH	570.280.921.671.974	0.0628042195081283	0.0836495719479821	0.418065723667828	0.564821627755414
MCOLN1	854.203.446.687.649	0.0870758272799398	0.128577790062911	0.478726811743744	0.622464822939255
STIM1	279.598.609.555.574	0.0889388752105342	0.0880916879107226	0.302797288672749	0.446274957562273
F2R	166.748.356.309.198	0.110639447436645	0.110393117808017	0.300908480333341	0.444224780302863
EDNRA	206.182.690.976.498	0.11977237588773	0.239855306412242	0.583076385014544	0.710293050835899
ATP2B1	461.626.628.987.639	0.138005263348501	0.104312447327456	0.173826346731307	0.29304324553352
PLCB2	489.493.216.881.739	0.148460461120645	0.357200444519728	0.498085877010279	0.64013790333965
EGFR	183.157.545.910.826	0.15414471676835	0.147426537239317	0.262530900964082	0.401076892043935
CAMK2G	308.856.140.894.947	0.161321439499772	0.0861961767053738	0.0560495627231519	0.119042800166328
TPCN2	962.925.542.934.949	0.163688229634313	0.127735585791043	0.180017322232568	0.301137783686921
MCU	232.326.143.842.897	0.221045523640019	0.0948496793645021	0.0166832275403525	0.0435548197581096
TBXA2R	2.791.255.953.813	0.221920495895446	0.210650643728027	0.22896567920061	0.361286110716458
GNAQ	335.459.683.975.552	0.224240766827919	0.119403166128341	0.0505041469254608	0.109429738958333
VEGFC	262.865.606.384.951	0.252700671951347	0.227767993537088	0.195701724209886	0.321311440786427
MET	320.453.265.120.091	0.266669221254998	0.140882757374689	0.0439163404621055	0.0976594709508658
GNAL	167.298.061.304.345	0.276532654299546	0.114951656898321	0.012100979045169	0.0331554640153218
PDGFC	851.803.632.271.765	0.277270899831492	0.134986267423683	0.0305866358113616	0.0727059910065298
PLCD3	169.699.382.882.478	0.281311858492587	0.120781708407388	0.0150483628998168	0.0398840609001914
ITPKA	31.922.290.961.536	0.299758123828119	0.236373895471205	0.133703915861153	0.238283254794966
ORAI2	198.370.882.017.582	0.307664239516031	0.120832479310531	0.00778793820930639	0.0228296793309466
ATP2A2	153.064.511.889.483	0.315242341768931	0.0910620865403779	0.000357803271130382	0.00151709402930254

P2RX4	670.723.664.696.776	0.319126310522452	0.166028279387448	0.03684946883754	0.0846902290966677
CAMK2D	277.091.778.625.274	0.349630625956543	0.110798494640924	0.00106991166438658	0.00401189901582001
PLCB3	30.578.336.330.819	0.369227730401235	0.0885761252993303	1,91E+09	0.000108029201407511
PPP3CA	256.585.595.024.188	0.373235392209162	0.12771848546183	0.00217807704361912	0.00749461396054691
PRKACB	155.479.632.445.332	0.382557095457931	0.152796328493714	0.0077530204829596	0.0227452518074045
ADCY3	35.157.160.555.465	0.384570165506337	0.10318861828844	0.00011816572969351	0.000561384634799467
SLC25A4	222.886.070.310.512	0.426581089118532	0.129454666583038	0.000538905641752702	0.00217817459658416
ORAI1	109.532.355.302.949	0.430951303438528	0.149874442423144	0.00215782305621755	0.00743753904020853
ERBB2	466.302.801.935.591	0.453000747759762	0.0859070335582125	7,17E+06	6,35E+07
PHKB	335.349.384.106.186	0.459366904885841	0.110460336516651	1,67E+07	9,52E+09
CALM1	120.000.433.254.103	0.473988326599753	0.0822585983329827	4,03E+05	4,40E+06
FGFR3	412.173.682.384.824	0.478844958517372	0.0926416266480472	1,18E+07	1,01E+08
GNAS	432.993.639.253.567	0.505876338060198	0.0933872474831993	2,81E+06	2,69E+07
ADORA2B	662.365.757.868.432	0.555313439236578	0.153468486520173	0.000115645342097655	0.000550846120311868
PPP3R1	311.618.175.694.851	0.55631882811167	0.11382605476247	4,12E+07	3,18E+08
GNA11	419.075.116.639.903	0.557660312687605	0.114087597573777	4,22E+07	3,24E+08
SLC25A5	31.554.050.213.949	0.591996841533849	0.0944225412316923	1,38E+03	1,94E+05
VDAC2	128.821.388.697.325	0.59427964544448	0.105051143244051	5,78E+04	6,16E+06
FGFR2	282.071.577.743.889	0.614594852851092	0.10179451505322	5,45E+04	6,90E+05
SPHK2	990.013.366.279.113	0.617877886815798	0.16358013542891	5,28E+08	0.00027165538890307
CALM2	139.947.481.397.403	0.658786203542567	0.0878843057258299	1,66E+00	4,31E+01
VDAC3	615.721.313.965.366	0.659604486969271	0.0792079673505408	2,75E-03	1,01E-01
VEGFB	182.794.381.075.822	0.66583541826766	0.128523584142247	6,82E+06	6,07E+07
SLC25A6	110.045.490.085.772	0.697750300545649	0.132019257663235	2,62E+06	2,52E+07
PPP3CB	282.723.784.431.472	0.737736854234094	0.1037294597725	3,04E+01	6,49E+02
CALM3	237.389.641.209.479	0.740184385222163	0.070241951160023	3,98E-12	4,23E-10
VDAC1	127.948.228.767.543	0.798029346731346	0.0882435705879339	2,97E-06	1,58E-04
CAMK1	302.929.731.805.388	0.832051455658237	0.114559291649818	8,35E+00	1,95E+02

Table S2: Rare coding pathogenic variants in ATP2B1 locus.

Among the n.351 coding variants of ATP2B1 from "The Genome Aggregation Database" (GnomAD v2.1), n.13 are reported as "pathogenic" according to "Functional Analysis through Hidden Markov Models" (FATHMM) prediction score. These variants are extremely rare and are thus excluded from further investigations. The chromosomal locus, position, rsID, dbSNP ID, the protein consequence, the fathmm prediction, the reference and alternative alleles, the transcript consequence, the variant annotation and the allele frequency are listed.

Chr	Position	rsID	dbSNP	ID	Protein	FATHMM prediction	Ref	Alt	Transcript consequence	Annotation	Allele frequency
12	89984832	rs115449702	rs115449702	NP_001673.2	I1198V	DAMAGING	T	C	c.3592A>G	missense_variant	7,96096E-06
12	89984882	rs142404163	rs142404163	NP_001673.2	P1181H	DAMAGING	G	T	c.3542C>A	missense_variant	0,000453695
12	89995138	rs79015625	rs79015625	NP_001001323.1	I1045V	DAMAGING	T	C	c.3133A>G	missense_variant	0,000900653
12	89997018	rs189003061	rs189003061	NP_001673.2	F954L	DAMAGING	A	T	c.2862T>A	missense_variant	4,24257E-06
12	90005121	rs182212584	rs182212584	NP_001001323.1	R699T	DAMAGING	C	G	c.2096G>C	missense_variant	3,00153E-05
12	90010584	rs145288143	rs145288143	NP_001001323.1	P688T	DAMAGING	G	T	c.2062C>A	missense_variant	1,99351E-05
12	90013932	rs199582675	rs199582675	NP_001673.2	R558Q	DAMAGING	C	T	c.1673G>A	missense_variant	3,98137E-06
12	90018046	rs184588664	rs184588664	NP_001673.2	F420L	DAMAGING	A	G	c.1258T>C	missense_variant	3,98096E-06
12	90018088	rs116585190	rs116585190	NP_001001323.1	A406S	DAMAGING	C	A	c.1216G>T	missense_variant	0,000159293
12	90028654	rs149203241	rs149203241	NP_001001323.1	L230F	DAMAGING	G	C	c.688C>G	missense_variant	4,00208E-06
12	90036125	rs200832650	rs200832650	NP_001001323.1	S72R	DAMAGING	A	T	c.216T>A	missense_variant	8,22788E-06
12	90049575	rs116694524	rs116694524	NP_001001323.1	T30M	DAMAGING	G	A	c.89C>T	missense_variant	0,000767591
12	90049584	rs201371800	rs201371800	NP_001001323.1	F27Y	DAMAGING	A	T	c.80T>A	missense_variant	3,97712E-06

Table S3: Non coding variants in the genomic region of the ATP2B1 locus acting as "expression quantitative traits loci" (eQTLs).

The genecode ID, gene symbol, Variant ID (chromosomal position, alternative and reference alleles), the SNP ID, P-Value, normalized enrichment score (NES) and tissue (by using "Genotype-Tissue Expression" GTex database) are listed.

Gencode Id	Gene symbol	Variant Id	SNP Id	P-value	NES	Tissue
ENSG00000070961.15	ATP2B1	chr12_89615182_A_G_b38	rs2681472	1,60E-18	0,35	Artery - Tibial
ENSG00000070961.15	ATP2B1	chr12_89619312_T_C_b38	rs2681492	3,40E-18	0,35	Artery - Tibial
ENSG00000070961.15	ATP2B1	chr12_89632685_G_A_b38	rs11105352	3,60E-18	0,35	Artery - Tibial
ENSG00000070961.15	ATP2B1	chr12_89632686_C_A_b38	rs11105353	3,60E-18	0,35	Artery - Tibial
ENSG00000070961.15	ATP2B1	chr12_89632746_A_G_b38	rs11105354	3,60E-18	0,35	Artery - Tibial
ENSG00000070961.15	ATP2B1	chr12_89656726_A_G_b38	rs12579302	3,60E-18	0,35	Artery - Tibial
ENSG00000070961.15	ATP2B1	chr12_89665065_G_A_b38	rs111478946	3,60E-18	0,35	Artery - Tibial
ENSG00000070961.15	ATP2B1	chr12_89675499_T_G_b38	rs11105364	3,60E-18	0,35	Artery - Tibial
ENSG00000070961.15	ATP2B1	chr12_89680664_G_C_b38	rs11105368	7,40E-18	0,34	Artery - Tibial
ENSG00000070961.15	ATP2B1	chr12_89681466_C_T_b38	rs4842675	7,40E-18	0,34	Artery - Tibial
ENSG00000070961.15	ATP2B1	chr12_89591515_AAAGT_A_b38	rs10580742	1,20E-17	0,35	Artery - Tibial
ENSG00000070961.15	ATP2B1	chr12_89696964_C_T_b38	rs11105378	1,30E-17	0,34	Artery - Tibial
ENSG00000070961.15	ATP2B1	chr12_89666809_G_A_b38	rs17249754	1,50E-17	0,34	Artery - Tibial
ENSG00000070961.15	ATP2B1	chr12_89668599_G_A_b38	rs6538195	1,50E-17	0,34	Artery - Tibial
ENSG00000070961.15	ATP2B1	chr12_89678299_G_A_b38	rs73437358	1,50E-17	0,34	Artery - Tibial
ENSG00000070961.15	ATP2B1	chr12_89625401_C_G_b38	rs57481061	1,50E-17	0,34	Artery - Tibial
ENSG00000070961.15	ATP2B1	chr12_89548613_A_G_b38	rs11105328	1,70E-17	0,34	Artery - Tibial
ENSG00000070961.15	ATP2B1	chr12_89547772_T_C_b38	rs4842666	2,10E-17	0,34	Artery - Tibial
ENSG00000070961.15	ATP2B1	chr12_89694803_T_A_b38	rs11105375	5,70E-17	0,34	Artery - Tibial
ENSG00000070961.15	ATP2B1	chr12_89697090_A_G_b38	rs12230074	8,10E-17	0,33	Artery - Tibial
ENSG00000070961.15	ATP2B1	chr12_89660842_T_C_b38	rs73437338	1,50E-16	0,33	Artery - Tibial
ENSG00000070961.15	ATP2B1	chr12_89597536_C_T_b38	rs117742247	4,20E-16	0,34	Artery - Tibial
ENSG00000070961.15	ATP2B1	chr12_89599730_A_T_b38	rs11105337	4,60E-16	0,33	Artery - Tibial
ENSG00000070961.15	ATP2B1	chr12_89694991_G_A_b38	rs11105376	7,80E-16	0,33	Artery - Tibial
ENSG00000070961.15	ATP2B1	chr12_89709925_C_G_b38	rs2280715	4,30E-14	0,31	Artery - Tibial
ENSG00000070961.15	ATP2B1	chr12_89713495_T_C_b38	rs11105382	4,30E-14	0,31	Artery - Tibial
ENSG00000070961.15	ATP2B1	chr12_89713529_T_C_b38	rs11105383	4,30E-14	0,31	Artery - Tibial
ENSG00000070961.15	ATP2B1	chr12_89719293_T_G_b38	rs7299436	4,30E-14	0,31	Artery - Tibial
ENSG00000070961.15	ATP2B1	chr12_89709168_C_G_b38	rs73437382	8,00E-14	0,3	Artery - Tibial
ENSG00000070961.15	ATP2B1	chr12_89698005_G_C_b38	rs4842676	6,10E-13	-0,27	Artery - Tibial
ENSG00000070961.15	ATP2B1	chr12_89701396_T_C_b38	rs11105379	1,40E-12	0,3	Artery - Tibial
ENSG00000070961.15	ATP2B1	chr12_89695013_G_A_b38	rs10858917	2,50E-12	-0,26	Artery - Tibial
ENSG00000070961.15	ATP2B1	chr12_89556543_A_C_b38	rs7302816	4,50E-12	0,25	Artery - Tibial
ENSG00000070961.15	ATP2B1	chr12_89713058_A_G_b38	rs11105381	2,90E-11	-0,25	Artery - Tibial
ENSG00000070961.15	ATP2B1	chr12_89715560_T_C_b38	rs2408046	5,50E-11	-0,24	Artery - Tibial
ENSG00000070961.15	ATP2B1	chr12_89703890_G_C_b38	rs10745511	5,70E-11	-0,25	Artery - Tibial
ENSG00000070961.15	ATP2B1	chr12_89705620_T_A_b38	rs2113894	5,70E-11	-0,25	Artery - Tibial
ENSG00000070961.15	ATP2B1	chr12_89696509_CAA_C_b38	rs10550903	7,60E-11	-0,23	Artery - Tibial
ENSG00000070961.15	ATP2B1	chr12_89738370_G_A_b38	rs12579052	5,40E-10	0,28	Artery - Tibial
ENSG00000070961.15	ATP2B1	chr12_90001084_A_T_b38	rs4408360	3,40E-08	-0,18	Esophagus - Mucosa
ENSG00000070961.15	ATP2B1	chr12_90024395_T_G_b38	rs149193253	4,40E-08	1	Brain - Anterior cingulate cortex (BA24)
ENSG00000070961.15	ATP2B1	chr12_90049701_T_C_b38	rs150184539	4,40E-08	1	Brain - Anterior cingulate cortex (BA24)
ENSG00000070961.15	ATP2B1	chr12_90137707_G_A_b38	rs77187603	4,40E-08	1	Brain - Anterior cingulate cortex (BA24)
ENSG00000070961.15	ATP2B1	chr12_90143905_A_G_b38	rs150119566	4,40E-08	1	Brain - Anterior cingulate cortex (BA24)
ENSG00000070961.15	ATP2B1	chr12_89677042_CAAAG_C_b38	rs143087380	5,00E-08	-0,17	Artery - Tibial
ENSG00000070961.15	ATP2B1	chr12_90006794_TA_T_b38	rs67882152	8,80E-08	-0,18	Esophagus - Mucosa
ENSG00000070961.15	ATP2B1	chr12_90006796_A_T_b38	rs114744356	8,80E-08	-0,18	Esophagus - Mucosa
ENSG00000070961.15	ATP2B1	chr12_90010274_T_C_b38	rs7488223	1,10E-07	-0,17	Esophagus - Mucosa
ENSG00000070961.15	ATP2B1	chr12_89973923_G_C_b38	rs4842701	1,30E-07	-0,17	Esophagus - Mucosa
ENSG00000070961.15	ATP2B1	chr12_89997003_T_C_b38	rs7968803	1,30E-07	-0,18	Esophagus - Mucosa
ENSG00000070961.15	ATP2B1	chr12_89991517_A_G_b38	rs10777217	1,60E-07	-0,17	Esophagus - Mucosa
ENSG00000070961.15	ATP2B1	chr12_89595822_G_A_b38	rs1401982	2,30E-07	-0,16	Artery - Tibial
ENSG00000070961.15	ATP2B1	chr12_89576142_A_AACTC_b38	rs10689649	2,50E-07	0,16	Artery - Tibial

ENSG00000070961.15	ATP2B1	chr12_89968275_A_G_b38	rs4466894	2,70E-07	-0,17	Esophagus - Mucosa
ENSG00000070961.15	ATP2B1	chr12_89584456_C_T_b38	rs1689040	2,80E-07	0,16	Artery - Tibial
ENSG00000070961.15	ATP2B1	chr12_89951830_C_T_b38	rs4842699	3,00E-07	-0,17	Esophagus - Mucosa
ENSG00000070961.15	ATP2B1	chr12_89631845_G_A_b38	rs2681485	3,30E-07	-0,16	Artery - Tibial
ENSG00000070961.15	ATP2B1	chr12_90140138_C_T_b38	rs55849728	3,80E-07	-0,18	Esophagus - Mucosa
ENSG00000070961.15	ATP2B1	chr12_89571272_C_T_b38	rs7313874	3,90E-07	0,16	Artery - Tibial
ENSG00000070961.15	ATP2B1	chr12_89434814_A_G_b38	rs8181784	4,20E-07	0,17	Artery - Tibial
ENSG00000070961.15	ATP2B1	chr12_89435693_C_T_b38	rs11105287	4,20E-07	0,17	Artery - Tibial
ENSG00000070961.15	ATP2B1	chr12_89569762_G_GAGA_b38	rs35533953	4,20E-07	0,16	Artery - Tibial
ENSG00000070961.15	ATP2B1	chr12_89687411_T_C_b38	rs7136259	5,00E-07	-0,16	Artery - Tibial
ENSG00000070961.15	ATP2B1	chr12_89702568_T_C_b38	rs10858918	5,00E-07	-0,17	Artery - Tibial
ENSG00000070961.15	ATP2B1	chr12_89943269_A_C_b38	rs4842697	5,20E-07	-0,17	Esophagus - Mucosa
ENSG00000070961.15	ATP2B1	chr12_89436943_T_C_b38	rs10777163	6,60E-07	0,17	Artery - Tibial
ENSG00000070961.15	ATP2B1	chr12_89643729_T_C_b38	rs111337717	7,20E-07	0,35	Artery - Tibial
ENSG00000070961.15	ATP2B1	chr12_89713948_C_T_b38	rs1590008	7,20E-07	-0,16	Artery - Tibial
ENSG00000070961.15	ATP2B1	chr12_89717005_G_A_b38	rs1980235	7,20E-07	-0,16	Artery - Tibial
ENSG00000070961.15	ATP2B1	chr12_90156621_AG_A_b38	rs369917221	7,60E-07	0,75	Artery - Tibial
ENSG00000070961.15	ATP2B1	chr12_90025415_G_A_b38	rs10858944	8,30E-07	-0,16	Esophagus - Mucosa
ENSG00000070961.15	ATP2B1	chr12_90034251_A_G_b38	rs73208536	8,40E-07	-0,16	Esophagus - Mucosa
ENSG00000070961.15	ATP2B1	chr12_90385245_G_A_b38	rs1594565	8,60E-07	0,38	Brain - Spinal cord (cervical c-1)
ENSG00000070961.15	ATP2B1	chr12_90047438_T_C_b38	rs10777221	8,70E-07	-0,16	Esophagus - Mucosa
ENSG00000070961.15	ATP2B1	chr12_90048224_G_A_b38	rs7488974	8,70E-07	-0,16	Esophagus - Mucosa
ENSG00000070961.15	ATP2B1	chr12_89987295_A_ATGTT_b38	rs10625779	9,80E-07	-0,16	Esophagus - Mucosa
ENSG00000070961.15	ATP2B1	chr12_89708115_T_A_b38	rs1358350	9,90E-07	-0,16	Artery - Tibial
ENSG00000070961.15	ATP2B1	chr12_89640625_G_GC_b38	rs66786558	0,0000011	-0,16	Artery - Tibial
ENSG00000070961.15	ATP2B1	chr12_89640630_T_C_b38	rs78409878	0,0000011	-0,16	Artery - Tibial
ENSG00000070961.15	ATP2B1	chr12_89648365_C_G_b38	rs11105358	0,0000011	-0,16	Artery - Tibial
ENSG00000070961.15	ATP2B1	chr12_90398938_C_T_b38	rs7955801	0,0000012	0,38	Brain - Spinal cord (cervical c-1)
ENSG00000070961.15	ATP2B1	chr12_90392860_A_C_b38	rs2116497	0,0000012	0,37	Brain - Spinal cord (cervical c-1)
ENSG00000070961.15	ATP2B1	chr12_89437093_C_T_b38	rs10858851	0,0000012	0,17	Artery - Tibial
ENSG00000070961.15	ATP2B1	chr12_90072266_A_G_b38	rs6538223	0,0000012	-0,16	Esophagus - Mucosa
ENSG00000070961.15	ATP2B1	chr12_90168240_C_T_b38	rs4842509	0,0000012	-0,17	Esophagus - Mucosa
ENSG00000070961.15	ATP2B1	chr12_90170518_A_G_b38	rs17836934	0,0000014	-0,17	Esophagus - Mucosa
ENSG00000070961.15	ATP2B1	chr12_89482366_T_C_b38	rs11105298	0,0000015	0,17	Artery - Tibial
ENSG00000070961.15	ATP2B1	chr12_90391772_A_C_b38	rs7976895	0,0000016	0,37	Brain - Spinal cord (cervical c-1)
ENSG00000070961.15	ATP2B1	chr12_90393455_G_A_b38	rs12580873	0,0000016	0,37	Brain - Spinal cord (cervical c-1)
ENSG00000070961.15	ATP2B1	chr12_90084874_G_A_b38	rs10858948	0,0000016	-0,15	Esophagus - Mucosa
ENSG00000070961.15	ATP2B1	chr12_90079719_A_G_b38	rs6538224	0,0000017	-0,16	Esophagus - Mucosa
ENSG00000070961.15	ATP2B1	chr12_90376827_T_C_b38	rs11105589	0,0000018	0,37	Brain - Spinal cord (cervical c-1)
ENSG00000070961.15	ATP2B1	chr12_90386667_C_T_b38	rs6538234	0,0000018	0,37	Brain - Spinal cord (cervical c-1)
ENSG00000070961.15	ATP2B1	chr12_90388244_T_A_b38	rs7979392	0,0000018	0,37	Brain - Spinal cord (cervical c-1)
ENSG00000070961.15	ATP2B1	chr12_90390285_G_C_b38	rs2043213	0,0000018	0,37	Brain - Spinal cord (cervical c-1)
ENSG00000070961.15	ATP2B1	chr12_89526956_C_T_b38	rs11105312	0,0000018	0,16	Artery - Tibial
ENSG00000070961.15	ATP2B1	chr12_89527498_C_T_b38	rs10777185	0,0000018	0,16	Artery - Tibial
ENSG00000070961.15	ATP2B1	chr12_89625452_C_T_b38	rs7297206	0,0000018	-0,15	Artery - Tibial
ENSG00000070961.15	ATP2B1	chr12_90059201_T_C_b38	rs7959983	0,0000021	-0,16	Esophagus - Mucosa
ENSG00000070961.15	ATP2B1	chr12_90080698_G_A_b38	rs7485419	0,0000021	-0,16	Esophagus - Mucosa
ENSG00000070961.15	ATP2B1	chr12_90376071_T_C_b38	rs12582977	0,0000023	0,37	Brain - Spinal cord (cervical c-1)
ENSG00000070961.15	ATP2B1	chr12_89533400_G_A_b38	rs11105319	0,0000024	0,16	Artery - Tibial
ENSG00000070961.15	ATP2B1	chr12_89534012_A_G_b38	rs10858902	0,0000024	0,16	Artery - Tibial
ENSG00000070961.15	ATP2B1	chr12_89534195_G_A_b38	rs10858903	0,0000024	0,16	Artery - Tibial
ENSG00000070961.15	ATP2B1	chr12_89539669_T_C_b38	rs4842662	0,0000024	0,16	Artery - Tibial
ENSG00000070961.15	ATP2B1	chr12_89539986_G_C_b38	rs3741898	0,0000024	0,16	Artery - Tibial
ENSG00000070961.15	ATP2B1	chr12_89540697_C_T_b38	rs10858906	0,0000024	0,16	Artery - Tibial
ENSG00000070961.15	ATP2B1	chr12_89541074_CAGAG_C_b38	rs71897440	0,0000024	0,16	Artery - Tibial
ENSG00000070961.15	ATP2B1	chr12_89541195_G_C_b38	rs12369195	0,0000024	0,16	Artery - Tibial
ENSG00000070961.15	ATP2B1	chr12_89528255_C_A_b38	rs10858897	0,0000025	0,16	Artery - Tibial
ENSG00000070961.15	ATP2B1	chr12_89535128_A_G_b38	rs12369685	0,0000026	0,17	Artery - Tibial
ENSG00000070961.15	ATP2B1	chr12_90068229_T_C_b38	rs7310135	0,0000026	-0,15	Esophagus - Mucosa
ENSG00000070961.15	ATP2B1	chr12_90079906_G_A_b38	rs6419356	0,0000026	-0,15	Esophagus - Mucosa
ENSG00000070961.15	ATP2B1	chr12_90081169_G_A_b38	rs7962435	0,0000026	-0,15	Esophagus - Mucosa
ENSG00000070961.15	ATP2B1	chr12_90084513_C_T_b38	rs7132441	0,0000026	-0,15	Esophagus - Mucosa

ENSG00000070961.15	ATP2B1	chr12_89530034_G_C_b38	rs10858899	0,0000027	0,16	Artery - Tibial
ENSG00000070961.15	ATP2B1	chr12_89530596_A_ATCT_b38	rs112698976	0,0000027	0,16	Artery - Tibial
ENSG00000070961.15	ATP2B1	chr12_89530782_C_T_b38	rs11105314	0,0000027	0,16	Artery - Tibial
ENSG00000070961.15	ATP2B1	chr12_89531423_T_G_b38	rs11105316	0,0000027	0,16	Artery - Tibial
ENSG00000070961.15	ATP2B1	chr12_89933142_G_A_b38	rs11105466	0,0000028	-0,16	Esophagus - Mucosa
ENSG00000070961.15	ATP2B1	chr12_89432148_T_C_b38	rs10858848	0,0000029	0,16	Artery - Tibial
ENSG00000070961.15	ATP2B1	chr12_89497589_G_A_b38	rs11105302	0,000003	0,16	Artery - Tibial
ENSG00000070961.15	ATP2B1	chr12_89497697_T_G_b38	rs10858881	0,000003	0,16	Artery - Tibial
ENSG00000070961.15	ATP2B1	chr12_89441951_C_A_b38	rs10858854	0,0000032	0,17	Artery - Tibial
ENSG00000070961.15	ATP2B1	chr12_89445295_C_T_b38	rs11105291	0,0000032	0,17	Artery - Tibial
ENSG00000070961.15	ATP2B1	chr12_89445926_A_G_b38	rs10858860	0,0000032	0,17	Artery - Tibial
ENSG00000070961.15	ATP2B1	chr12_90049705_A_G_b38	rs10858945	0,0000032	-0,15	Esophagus - Mucosa
ENSG00000070961.15	ATP2B1	chr12_90050234_G_T_b38	rs7958749	0,0000032	-0,15	Esophagus - Mucosa
ENSG00000070961.15	ATP2B1	chr12_89481583_G_A_b38	rs75615848	0,0000035	0,32	Artery - Tibial
ENSG00000070961.15	ATP2B1	chr12_89439561_T_C_b38	rs10858852	0,0000036	0,16	Artery - Tibial
ENSG00000070961.15	ATP2B1	chr12_89440336_C_T_b38	rs4842653	0,0000036	0,16	Artery - Tibial
ENSG00000070961.15	ATP2B1	chr12_89440651_T_A_b38	rs4842654	0,0000036	0,16	Artery - Tibial
ENSG00000070961.15	ATP2B1	chr12_89442082_C_G_b38	rs10858855	0,0000036	0,16	Artery - Tibial
ENSG00000070961.15	ATP2B1	chr12_89442149_G_A_b38	rs9795772	0,0000036	0,16	Artery - Tibial
ENSG00000070961.15	ATP2B1	chr12_89442895_G_C_b38	rs11513812	0,0000036	0,16	Artery - Tibial
ENSG00000070961.15	ATP2B1	chr12_89443404_T_C_b38	rs11105289	0,0000036	0,16	Artery - Tibial
ENSG00000070961.15	ATP2B1	chr12_89445026_A_T_b38	rs11105290	0,0000036	0,16	Artery - Tibial
ENSG00000070961.15	ATP2B1	chr12_89445465_C_T_b38	rs10858859	0,0000036	0,16	Artery - Tibial
ENSG00000070961.15	ATP2B1	chr12_89445949_A_G_b38	rs10858861	0,0000036	0,16	Artery - Tibial
ENSG00000070961.15	ATP2B1	chr12_89448276_T_C_b38	rs10858862	0,0000036	0,16	Artery - Tibial
ENSG00000070961.15	ATP2B1	chr12_89451080_T_TG_b38	rs11461256	0,0000036	0,16	Artery - Tibial
ENSG00000070961.15	ATP2B1	chr12_89452453_C_T_b38	rs10858864	0,0000036	0,16	Artery - Tibial
ENSG00000070961.15	ATP2B1	chr12_89452699_G_A_b38	rs10858865	0,0000036	0,16	Artery - Tibial
ENSG00000070961.15	ATP2B1	chr12_89457389_C_T_b38	rs10858867	0,0000036	0,16	Artery - Tibial
ENSG00000070961.15	ATP2B1	chr12_89463834_C_T_b38	rs10858869	0,0000036	0,16	Artery - Tibial
ENSG00000070961.15	ATP2B1	chr12_89466542_C_A_b38	rs3803128	0,0000036	0,16	Artery - Tibial
ENSG00000070961.15	ATP2B1	chr12_89467752_T_C_b38	rs10506972	0,0000036	0,16	Artery - Tibial
ENSG00000070961.15	ATP2B1	chr12_89468253_G_T_b38	rs12228177	0,0000036	0,16	Artery - Tibial
ENSG00000070961.15	ATP2B1	chr12_89477836_G_A_b38	rs10858871	0,0000036	0,16	Artery - Tibial
ENSG00000070961.15	ATP2B1	chr12_89479155_C_T_b38	rs10858872	0,0000036	0,16	Artery - Tibial
ENSG00000070961.15	ATP2B1	chr12_89483146_C_T_b38	rs112511312	0,0000036	0,16	Artery - Tibial
ENSG00000070961.15	ATP2B1	chr12_89484166_A_G_b38	rs11105299	0,0000036	0,16	Artery - Tibial
ENSG00000070961.15	ATP2B1	chr12_89487787_C_G_b38	rs4842488	0,0000036	0,16	Artery - Tibial
ENSG00000070961.15	ATP2B1	chr12_89490501_C_T_b38	rs10858877	0,0000036	0,16	Artery - Tibial
ENSG00000070961.15	ATP2B1	chr12_89490517_G_A_b38	rs10858878	0,0000036	0,16	Artery - Tibial
ENSG00000070961.15	ATP2B1	chr12_89492146_C_A_b38	rs6538189	0,0000036	0,16	Artery - Tibial
ENSG00000070961.15	ATP2B1	chr12_89492165_T_C_b38	rs6538190	0,0000036	0,16	Artery - Tibial
ENSG00000070961.15	ATP2B1	chr12_89492801_T_A_b38	rs10858879	0,0000036	0,16	Artery - Tibial
ENSG00000070961.15	ATP2B1	chr12_89493872_T_C_b38	rs1008764	0,0000036	0,16	Artery - Tibial
ENSG00000070961.15	ATP2B1	chr12_89503120_C_T_b38	rs10858885	0,0000036	0,16	Artery - Tibial
ENSG00000070961.15	ATP2B1	chr12_89503384_C_G_b38	rs10858886	0,0000036	0,16	Artery - Tibial
ENSG00000070961.15	ATP2B1	chr12_89503557_C_T_b38	rs11105305	0,0000036	0,16	Artery - Tibial
ENSG00000070961.15	ATP2B1	chr12_89503611_C_T_b38	rs11105306	0,0000036	0,16	Artery - Tibial
ENSG00000070961.15	ATP2B1	chr12_89508827_G_A_b38	rs10858889	0,0000036	0,16	Artery - Tibial
ENSG00000070961.15	ATP2B1	chr12_89513389_T_C_b38	rs10858890	0,0000036	0,16	Artery - Tibial
ENSG00000070961.15	ATP2B1	chr12_89516073_T_C_b38	rs11105309	0,0000036	0,16	Artery - Tibial
ENSG00000070961.15	ATP2B1	chr12_89519642_C_T_b38	rs1054807	0,0000036	0,16	Artery - Tibial
ENSG00000070961.15	ATP2B1	chr12_89520484_T_C_b38	rs10858894	0,0000036	0,16	Artery - Tibial
ENSG00000070961.15	ATP2B1	chr12_89529599_A_T_b38	rs11105313	0,0000036	0,16	Artery - Tibial
ENSG00000070961.15	ATP2B1	chr12_90056289_A_G_b38	rs12227543	0,0000036	-0,15	Esophagus - Mucosa
ENSG00000070961.15	ATP2B1	chr12_89524900_C_A_b38	rs11105310	0,0000037	0,16	Artery - Tibial
ENSG00000070961.15	ATP2B1	chr12_89525791_C_T_b38	rs10777184	0,0000037	0,16	Artery - Tibial
ENSG00000070961.15	ATP2B1	chr12_89526407_C_T_b38	rs10858896	0,0000037	0,16	Artery - Tibial
ENSG00000070961.15	ATP2B1	chr12_89527500_G_A_b38	rs10777186	0,0000037	0,16	Artery - Tibial
ENSG00000070961.15	ATP2B1	chr12_90052157_T_C_b38	rs4842710	0,0000037	-0,15	Esophagus - Mucosa
ENSG00000070961.15	ATP2B1	chr12_90057274_A_G_b38	rs10858947	0,0000037	-0,15	Esophagus - Mucosa
ENSG00000070961.15	ATP2B1	chr12_90068211_G_A_b38	rs7139279	0,0000037	-0,15	Esophagus - Mucosa
ENSG00000070961.15	ATP2B1	chr12_90077187_C_T_b38	rs7488228	0,0000037	-0,15	Esophagus - Mucosa
ENSG00000070961.15	ATP2B1	chr12_90083730_C_T_b38	rs4842505	0,0000037	-0,15	Esophagus - Mucosa
ENSG00000070961.15	ATP2B1	chr12_90083900_C_T_b38	rs7306280	0,0000037	-0,15	Esophagus - Mucosa
ENSG00000070961.15	ATP2B1	chr12_89996947_A_G_b38	rs7953742	0,0000038	-0,15	Esophagus - Mucosa
ENSG00000070961.15	ATP2B1	chr12_89996827_CA_C_b38	rs112780917	0,0000039	-0,15	Esophagus - Mucosa
ENSG00000070961.15	ATP2B1	chr12_90007154_C_CA_b38	rs11396475	0,0000039	-0,15	Esophagus - Mucosa
ENSG00000070961.15	ATP2B1	chr12_90018978_A_C_b38	rs4842705	0,0000039	-0,15	Esophagus - Mucosa
ENSG00000070961.15	ATP2B1	chr12_89531304_C_A_b38	rs10858900	0,0000041	0,16	Artery - Tibial
ENSG00000070961.15	ATP2B1	chr12_89536622_A_G_b38	rs4842661	0,0000047	0,17	Artery - Tibial

ENSG00000070961.15	ATP2B1	chr12_89539933_C_T_b38	rs3825330	0,000005	0,16	Artery - Tibial
ENSG00000070961.15	ATP2B1	chr12_89541610_C_T_b38	rs10858909	0,000005	0,16	Artery - Tibial
ENSG00000070961.15	ATP2B1	chr12_89544813_G_A_b38	rs11105325	0,000005	0,16	Artery - Tibial
ENSG00000070961.15	ATP2B1	chr12_90050964_A_G_b38	rs10777222	0,000005	-0,15	Esophagus - Mucosa
ENSG00000070961.15	ATP2B1	chr12_89540154_G_A_b38	rs3741899	0,0000051	0,16	Artery - Tibial
ENSG00000070961.15	ATP2B1	chr12_90389431_C_T_b38	rs1228496	0,0000052	0,49	Brain - Substantia nigra
ENSG00000070961.15	ATP2B1	chr12_89528334_A_G_b38	rs10858898	0,0000052	0,16	Artery - Tibial
ENSG00000070961.15	ATP2B1	chr12_89544253_G_A_b38	rs4842664	0,0000052	0,16	Artery - Tibial
ENSG00000070961.15	ATP2B1	chr12_90510721_G_T_b38	rs12578110	0,0000055	0,46	Brain - Substantia nigra
ENSG00000070961.15	ATP2B1	chr12_89532881_G_A_b38	rs11105318	0,0000056	0,16	Artery - Tibial
ENSG00000070961.15	ATP2B1	chr12_89931928_T_C_b38	rs7970120	0,0000063	-0,21	Artery - Tibial
ENSG00000070961.15	ATP2B1	chr12_89432335_C_G_b38	rs11105286	0,0000064	0,15	Artery - Tibial
ENSG00000070961.15	ATP2B1	chr12_90386667_C_T_b38	rs6538234	0,0000083	0,51	Brain - Substantia nigra
ENSG00000070961.15	ATP2B1	chr12_90388244_T_A_b38	rs7979392	0,0000083	0,51	Brain - Substantia nigra
ENSG00000070961.15	ATP2B1	chr12_90390285_G_C_b38	rs2043213	0,0000083	0,51	Brain - Substantia nigra
ENSG00000070961.15	ATP2B1	chr12_90398938_C_T_b38	rs7955801	0,0000083	0,51	Brain - Substantia nigra
ENSG00000070961.15	ATP2B1	chr12_90063091_G_A_b38	rs6538220	0,0000084	-0,15	Esophagus - Mucosa
ENSG00000070961.15	ATP2B1	chr12_90516738_A_G_b38	rs1347015	0,0000088	0,47	Brain - Substantia nigra
ENSG00000070961.15	ATP2B1	chr12_90523189_C_T_b38	rs1579534	0,0000088	0,47	Brain - Substantia nigra
ENSG00000070961.15	ATP2B1	chr12_90510105_C_T_b38	rs10858992	0,0000088	0,46	Brain - Substantia nigra
ENSG00000070961.15	ATP2B1	chr12_90519613_A_T_b38	rs61655253	0,0000088	0,46	Brain - Substantia nigra
ENSG00000070961.15	ATP2B1	chr12_90528232_A_G_b38	rs4274255	0,0000088	0,46	Brain - Substantia nigra
ENSG00000070961.15	ATP2B1	chr12_90528837_C_T_b38	rs11105663	0,0000088	0,46	Brain - Substantia nigra
ENSG00000070961.15	ATP2B1	chr12_90532822_TTCTTAAGGACAA_T_b38	rs6144807	0,0000088	0,46	Brain - Substantia nigra
ENSG00000070961.15	ATP2B1	chr12_90533124_TA_T_b38	rs36032096	0,0000088	0,46	Brain - Substantia nigra
ENSG00000070961.15	ATP2B1	chr12_90535560_T_C_b38	rs12580833	0,0000088	0,46	Brain - Substantia nigra
ENSG00000070961.15	ATP2B1	chr12_90543285_C_T_b38	rs11105668	0,0000088	0,46	Brain - Substantia nigra
ENSG00000070961.15	ATP2B1	chr12_89780365_G_T_b38	rs116990534	0,0000092	0,35	Artery - Tibial
ENSG00000070961.15	ATP2B1	chr12_89719404_G_A_b38	rs4842679	0,0000094	-0,15	Artery - Tibial
ENSG00000070961.15	ATP2B1	chr12_89504370_G_A_b38	rs138808993	0,0000095	0,65	Brain - Anterior cingulate cortex (BA24)
ENSG00000070961.15	ATP2B1	chr12_89538657_G_A_b38	rs143285018	0,0000095	0,65	Brain - Anterior cingulate cortex (BA24)
ENSG00000070961.15	ATP2B1	chr12_90129715_G_A_b38	rs59313167	0,0000097	-0,15	Esophagus - Mucosa
ENSG00000070961.15	ATP2B1	chr12_90134908_C_T_b38	rs7970711	0,0000097	-0,15	Esophagus - Mucosa
ENSG00000070961.15	ATP2B1	chr12_90136962_G_A_b38	rs7979050	0,0000097	-0,15	Esophagus - Mucosa
ENSG00000070961.15	ATP2B1	chr12_89959608_C_T_b38	rs11105474	0,00001	-0,14	Esophagus - Mucosa
ENSG00000070961.15	ATP2B1	chr12_89622750_A_G_b38	rs147471906	0,000011	0,59	Brain - Anterior cingulate cortex (BA24)
ENSG00000070961.15	ATP2B1	chr12_89643621_G_A_b38	rs149731397	0,000011	0,59	Brain - Anterior cingulate cortex (BA24)
ENSG00000070961.15	ATP2B1	chr12_90394122_TTTC_T_b38	rs10543504	0,000011	0,52	Brain - Substantia nigra
ENSG00000070961.15	ATP2B1	chr12_90385245_G_A_b38	rs1594565	0,000011	0,5	Brain - Substantia nigra
ENSG00000070961.15	ATP2B1	chr12_90088859_T_C_b38	rs11105501	0,000011	-0,15	Esophagus - Mucosa
ENSG00000070961.15	ATP2B1	chr12_90089663_G_A_b38	rs11105503	0,000011	-0,15	Esophagus - Mucosa
ENSG00000070961.15	ATP2B1	chr12_90089938_C_T_b38	rs11105504	0,000011	-0,15	Esophagus - Mucosa
ENSG00000070961.15	ATP2B1	chr12_89926004_G_A_b38	rs111342256	0,000012	0,65	Artery - Tibial
ENSG00000070961.15	ATP2B1	chr12_90195090_A_G_b38	rs10858967	0,000012	-0,34	Cells - EBV-transformed lymphocytes
ENSG00000070961.15	ATP2B1	chr12_90407150_G_A_b38	rs7969733	0,000013	0,34	Brain - Spinal cord (cervical c-1)
ENSG00000070961.15	ATP2B1	chr12_90411424_C_G_b38	rs10777244	0,000013	0,34	Brain - Spinal cord (cervical c-1)
ENSG00000070961.15	ATP2B1	chr12_90411690_G_A_b38	rs7958205	0,000013	0,34	Brain - Spinal cord (cervical c-1)
ENSG00000070961.15	ATP2B1	chr12_90411780_G_A_b38	rs7958308	0,000013	0,34	Brain - Spinal cord (cervical c-1)
ENSG00000070961.15	ATP2B1	chr12_90414020_G_T_b38	rs7966452	0,000013	0,34	Brain - Spinal cord (cervical c-1)
ENSG00000070961.15	ATP2B1	chr12_90414588_CT_C_b38	rs35829324	0,000013	0,34	Brain - Spinal cord (cervical c-1)
ENSG00000070961.15	ATP2B1	chr12_90416671_A_G_b38	rs2897862	0,000013	0,34	Brain - Spinal cord (cervical c-1)
ENSG00000070961.15	ATP2B1	chr12_90416672_A_T_b38	rs2408160	0,000013	0,34	Brain - Spinal cord (cervical c-1)
ENSG00000070961.15	ATP2B1	chr12_90422109_C_T_b38	rs7315821	0,000013	0,34	Brain - Spinal cord (cervical c-1)
ENSG00000070961.15	ATP2B1	chr12_90425535_T_A_b38	rs6538235	0,000013	0,34	Brain - Spinal cord (cervical c-1)
ENSG00000070961.15	ATP2B1	chr12_90427858_G_A_b38	rs10777245	0,000013	0,34	Brain - Spinal cord (cervical c-1)

ENSG00000070961.15	ATP2B1	chr12_90430064_C_G_b38	rs6538236	0,000013	0,34	Brain - Spinal cord (cervical c-1)
ENSG00000070961.15	ATP2B1	chr12_90436231_T_C_b38	rs1835768	0,000013	0,34	Brain - Spinal cord (cervical c-1)
ENSG00000070961.15	ATP2B1	chr12_90436298_G_A_b38	rs1835767	0,000013	0,34	Brain - Spinal cord (cervical c-1)
ENSG00000070961.15	ATP2B1	chr12_90439201_G_A_b38	rs34234695	0,000013	0,34	Brain - Spinal cord (cervical c-1)
ENSG00000070961.15	ATP2B1	chr12_90439855_C_T_b38	rs11105617	0,000013	0,34	Brain - Spinal cord (cervical c-1)
ENSG00000070961.15	ATP2B1	chr12_90443686_G_A_b38	rs66955893	0,000013	0,34	Brain - Spinal cord (cervical c-1)
ENSG00000070961.15	ATP2B1	chr12_90451488_G_A_b38	rs11105622	0,000013	0,34	Brain - Spinal cord (cervical c-1)
ENSG00000070961.15	ATP2B1	chr12_90452503_C_T_b38	rs7960740	0,000013	0,34	Brain - Spinal cord (cervical c-1)
ENSG00000070961.15	ATP2B1	chr12_90457546_A_T_b38	rs11105623	0,000013	0,34	Brain - Spinal cord (cervical c-1)
ENSG00000070961.15	ATP2B1	chr12_90468635_G_A_b38	rs7954409	0,000013	0,34	Brain - Spinal cord (cervical c-1)
ENSG00000070961.15	ATP2B1	chr12_90474639_G_A_b38	rs1864782	0,000013	0,34	Brain - Spinal cord (cervical c-1)
ENSG00000070961.15	ATP2B1	chr12_90476135_C_T_b38	rs7298940	0,000013	0,34	Brain - Spinal cord (cervical c-1)
ENSG00000070961.15	ATP2B1	chr12_90478226_G_A_b38	rs12818545	0,000013	0,34	Brain - Spinal cord (cervical c-1)
ENSG00000070961.15	ATP2B1	chr12_90482472_AAC_A_b38	rs67668093	0,000013	0,34	Brain - Spinal cord (cervical c-1)
ENSG00000070961.15	ATP2B1	chr12_90484858_C_T_b38	rs7311599	0,000013	0,34	Brain - Spinal cord (cervical c-1)
ENSG00000070961.15	ATP2B1	chr12_90559065_T_A_b38	rs2520561	0,000013	0,31	Brain - Spinal cord (cervical c-1)
ENSG00000070961.15	ATP2B1	chr12_90391772_A_C_b38	rs7976895	0,000014	0,48	Brain - Substantia nigra
ENSG00000070961.15	ATP2B1	chr12_90392860_A_C_b38	rs2116497	0,000014	0,48	Brain - Substantia nigra
ENSG00000070961.15	ATP2B1	chr12_90393455_G_A_b38	rs12580873	0,000014	0,48	Brain - Substantia nigra
ENSG00000070961.15	ATP2B1	chr12_90552916_G_A_b38	rs2520567	0,000014	0,44	Brain - Substantia nigra
ENSG00000070961.15	ATP2B1	chr12_90001825_T_C_b38	rs17192565	0,000014	0,43	Artery - Tibial
ENSG00000070961.15	ATP2B1	chr12_90459042_T_A_b38	rs7132660	0,000014	0,34	Brain - Spinal cord (cervical c-1)
ENSG00000070961.15	ATP2B1	chr12_90106317_C_CAT_b38	rs148143712	0,000015	-0,15	Esophagus - Mucosa
ENSG00000070961.15	ATP2B1	chr12_90112140_G_A_b38	rs7966278	0,000015	-0,15	Esophagus - Mucosa
ENSG00000070961.15	ATP2B1	chr12_89556543_A_C_b38	rs7302816	0,000016	0,19	Artery - Aorta
ENSG00000070961.15	ATP2B1	chr12_89422110_G_A_b38	rs80277599	0,000017	1,4	Brain - Hypothalamus
ENSG00000070961.15	ATP2B1	chr12_89428758_A_G_b38	rs112370308	0,000017	1,4	Brain - Hypothalamus
ENSG00000070961.15	ATP2B1	chr12_89441431_T_C_b38	rs113025676	0,000017	1,4	Brain - Hypothalamus
ENSG00000070961.15	ATP2B1	chr12_89457067_C_T_b38	rs61435009	0,000017	1,4	Brain - Hypothalamus
ENSG00000070961.15	ATP2B1	chr12_89471149_A_G_b38	rs74754458	0,000017	1,4	Brain - Hypothalamus
ENSG00000070961.15	ATP2B1	chr12_89478671_T_C_b38	rs60772618	0,000017	1,4	Brain - Hypothalamus
ENSG00000070961.15	ATP2B1	chr12_89484136_C_G_b38	rs74543833	0,000017	1,4	Brain - Hypothalamus
ENSG00000070961.15	ATP2B1	chr12_89487042_C_G_b38	rs58117070	0,000017	1,4	Brain - Hypothalamus
ENSG00000070961.15	ATP2B1	chr12_89488169_C_T_b38	rs185300284	0,000017	1,4	Brain - Hypothalamus
ENSG00000070961.15	ATP2B1	chr12_89488792_C_T_b38	rs76672752	0,000017	1,4	Brain - Hypothalamus
ENSG00000070961.15	ATP2B1	chr12_89490053_G_T_b38	rs78332000	0,000017	1,4	Brain - Hypothalamus
ENSG00000070961.15	ATP2B1	chr12_90581088_T_TA_b38	rs143922775	0,000017	1,4	Brain - Hypothalamus
ENSG00000070961.15	ATP2B1	chr12_90583461_C_T_b38	rs17018043	0,000017	1,4	Brain - Hypothalamus
ENSG00000070961.15	ATP2B1	chr12_90586839_A_G_b38	rs73358180	0,000017	1,4	Brain - Hypothalamus
ENSG00000070961.15	ATP2B1	chr12_90589431_T_C_b38	rs73358183	0,000017	1,4	Brain - Hypothalamus
ENSG00000070961.15	ATP2B1	chr12_90593192_C_T_b38	rs73358194	0,000017	1,4	Brain - Hypothalamus
ENSG00000070961.15	ATP2B1	chr12_90594592_G_A_b38	rs2106528	0,000017	1,4	Brain - Hypothalamus
ENSG00000070961.15	ATP2B1	chr12_90599502_C_T_b38	rs76134788	0,000017	1,4	Brain - Hypothalamus
ENSG00000070961.15	ATP2B1	chr12_90602009_G_C_b38	rs73360109	0,000017	1,4	Brain - Hypothalamus
ENSG00000070961.15	ATP2B1	chr12_90602975_T_C_b38	rs73360112	0,000017	1,4	Brain - Hypothalamus
ENSG00000070961.15	ATP2B1	chr12_90603192_A_G_b38	rs17018088	0,000017	1,4	Brain - Hypothalamus
ENSG00000070961.15	ATP2B1	chr12_90606864_CAG_C_b38	rs34639687	0,000017	1,4	Brain - Hypothalamus
ENSG00000070961.15	ATP2B1	chr12_90608792_A_G_b38	rs7306918	0,000017	1,4	Brain - Hypothalamus
ENSG00000070961.15	ATP2B1	chr12_90609936_C_T_b38	rs73360125	0,000017	1,4	Brain - Hypothalamus
ENSG00000070961.15	ATP2B1	chr12_90614576_G_T_b38	rs73360133	0,000017	1,4	Brain - Hypothalamus
ENSG00000070961.15	ATP2B1	chr12_90626419_G_T_b38	rs11829105	0,000017	1,4	Brain - Hypothalamus
ENSG00000070961.15	ATP2B1	chr12_90626488_A_T_b38	rs11833692	0,000017	1,4	Brain - Hypothalamus
ENSG00000070961.15	ATP2B1	chr12_90628581_A_G_b38	rs73360170	0,000017	1,4	Brain - Hypothalamus
ENSG00000070961.15	ATP2B1	chr12_90646115_A_G_b38	rs11830515	0,000017	1,4	Brain - Hypothalamus
ENSG00000070961.15	ATP2B1	chr12_90650906_T_C_b38	rs11105723	0,000017	1,4	Brain - Hypothalamus

ENSG00000070961.15	ATP2B1	chr12_90661217_T_C_b38	rs11105730	0,000017	1,4	Brain - Hypothalamus
ENSG00000070961.15	ATP2B1	chr12_89525853_ACC_A_b38	rs67346689	0,000017	0,16	Artery - Tibial
ENSG00000070961.15	ATP2B1	chr12_90637101_TTG_T_b38	rs1491580271	0,000018	1,4	Brain - Hypothalamus
ENSG00000070961.15	ATP2B1	chr12_90136354_G_A_b38	rs143689254	0,000018	0,68	Brain - Anterior cingulate cortex (BA24)
ENSG00000070961.15	ATP2B1	chr12_90241276_A_G_b38	rs73196463	0,000018	0,62	Artery - Tibial
ENSG00000070961.15	ATP2B1	chr12_90554733_G_A_b38	rs2520565	0,000018	0,44	Brain - Substantia nigra
ENSG00000070961.15	ATP2B1	chr12_90556726_A_G_b38	rs2520563	0,000018	0,44	Brain - Substantia nigra
ENSG00000070961.15	ATP2B1	chr12_90557663_C_T_b38	rs2520562	0,000018	0,44	Brain - Substantia nigra
ENSG00000070961.15	ATP2B1	chr12_90558072_T_C_b38	rs2723917	0,000018	0,44	Brain - Substantia nigra
ENSG00000070961.15	ATP2B1	chr12_89569279_G_A_b38	rs372643302	0,000018	0,17	Artery - Tibial
ENSG00000070961.15	ATP2B1	chr12_89950918_A_G_b38	rs7294671	0,000018	-0,13	Esophagus - Mucosa
ENSG00000070961.15	ATP2B1	chr12_89956338_C_G_b38	rs11105473	0,000018	-0,14	Esophagus - Mucosa
ENSG00000070961.15	ATP2B1	chr12_89957460_T_G_b38	rs7132526	0,000018	-0,14	Esophagus - Mucosa
ENSG00000070961.15	ATP2B1	chr12_89704243_G_A_b38	rs61926784	0,000019	0,19	Brain - Frontal Cortex (BA9)
ENSG00000070961.15	ATP2B1	chr12_90326873_G_T_b38	rs825954	0,000023	-0,15	Esophagus - Muscularis
ENSG00000070961.15	ATP2B1	chr12_90329398_C_T_b38	rs10858974	0,000024	-0,13	Thyroid
ENSG00000070961.15	ATP2B1	chr12_90299326_G_A_b38	rs11105563	0,000024	-0,35	Cells - EBV-transformed lymphocytes
ENSG00000070961.15	ATP2B1	chr12_89876539_G_A_b38	rs74851539	0,000025	0,41	Artery - Tibial
ENSG00000070961.15	ATP2B1	chr12_89940862_G_A_b38	rs12368259	0,000027	0,22	Esophagus - Mucosa
ENSG00000070961.15	ATP2B1	chr12_90299488_G_C_b38	rs10506984	0,000027	-0,34	Cells - EBV-transformed lymphocytes
ENSG00000070961.15	ATP2B1	chr12_90303890_G_C_b38	rs2056699	0,000027	-0,34	Cells - EBV-transformed lymphocytes
ENSG00000070961.15	ATP2B1	chr12_90306554_G_A_b38	rs1587440	0,000027	-0,34	Cells - EBV-transformed lymphocytes
ENSG00000070961.15	ATP2B1	chr12_90311197_C_T_b38	rs10858971	0,000027	-0,34	Cells - EBV-transformed lymphocytes
ENSG00000070961.15	ATP2B1	chr12_90631370_A_T_b38	rs11105706	0,000028	-0,28	Colon - Transverse
ENSG00000070961.15	ATP2B1	chr12_90631458_A_G_b38	rs11105707	0,000028	-0,28	Colon - Transverse
ENSG00000070961.15	ATP2B1	chr12_90632378_G_A_b38	rs11105709	0,000028	-0,28	Colon - Transverse
ENSG00000070961.15	ATP2B1	chr12_90636015_C_A_b38	rs11105712	0,000028	-0,28	Colon - Transverse
ENSG00000070961.15	ATP2B1	chr12_90638508_T_A_b38	rs112784216	0,000028	-0,28	Colon - Transverse
ENSG00000070961.15	ATP2B1	chr12_90451210_G_A_b38	rs1148676	0,000029	0,3	Brain - Spinal cord (cervical c-1)
ENSG00000070961.15	ATP2B1	chr12_89973104_A_G_b38	rs10777215	0,000029	-0,13	Esophagus - Mucosa
ENSG00000070961.15	ATP2B1	chr12_89999628_A_ATTC_b38	rs10671258	0,000029	-0,13	Esophagus - Mucosa
ENSG00000070961.15	ATP2B1	chr12_90000940_A_G_b38	rs4406875	0,000029	-0,13	Esophagus - Mucosa
ENSG00000070961.15	ATP2B1	chr12_90005097_T_A_b38	rs4240746	0,000029	-0,13	Esophagus - Mucosa
ENSG00000070961.15	ATP2B1	chr12_89559134_C_T_b38	rs112417857	0,000031	0,54	Artery - Tibial
ENSG00000070961.15	ATP2B1	chr12_89394010_T_C_b38	rs11105273	0,000031	0,18	Artery - Tibial
ENSG00000070961.15	ATP2B1	chr12_89975574_A_G_b38	rs7303123	0,000031	-0,13	Esophagus - Mucosa
ENSG00000070961.15	ATP2B1	chr12_89976239_C_T_b38	rs10777216	0,000031	-0,13	Esophagus - Mucosa
ENSG00000070961.15	ATP2B1	chr12_89957885_A_G_b38	rs4842700	0,000032	-0,18	Artery - Tibial
ENSG00000070961.15	ATP2B1	chr12_90287401_C_T_b38	rs11105559	0,000032	-0,34	Cells - EBV-transformed lymphocytes
ENSG00000070961.15	ATP2B1	chr12_90295570_G_A_b38	rs2165035	0,000032	-0,34	Cells - EBV-transformed lymphocytes
ENSG00000070961.15	ATP2B1	chr12_90273379_C_A_b38	rs12320693	0,000033	-0,37	Cells - EBV-transformed lymphocytes
ENSG00000070961.15	ATP2B1	chr12_89995520_A_C_b38	rs6538214	0,000034	-0,13	Esophagus - Mucosa
ENSG00000070961.15	ATP2B1	chr12_90007782_T_TATAAA_b38	rs57291885	0,000034	-0,13	Esophagus - Mucosa
ENSG00000070961.15	ATP2B1	chr12_90008924_A_C_b38	rs4842504	0,000034	-0,13	Esophagus - Mucosa
ENSG00000070961.15	ATP2B1	chr12_90018772_T_C_b38	rs10858942	0,000034	-0,13	Esophagus - Mucosa
ENSG00000070961.15	ATP2B1	chr12_90061403_T_C_b38	rs7303035	0,000037	-0,13	Esophagus - Mucosa
ENSG00000070961.15	ATP2B1	chr12_89042639_G_A_b38	rs76671707	0,000037	-0,57	Lung
ENSG00000070961.15	ATP2B1	chr12_90266564_G_A_b38	rs1347846	0,000039	-0,33	Cells - EBV-transformed lymphocytes
ENSG00000070961.15	ATP2B1	chr12_90259816_T_C_b38	rs4381424	0,000039	-0,34	Cells - EBV-transformed lymphocytes
ENSG00000070961.15	ATP2B1	chr12_90303378_AT_A_b38	rs141511768	0,000039	-0,36	Cells - EBV-transformed lymphocytes
ENSG00000070961.15	ATP2B1	chr12_90275487_CAA_C_b38	rs3042884	0,000041	-0,35	Cells - EBV-transformed lymphocytes
ENSG00000070961.15	ATP2B1	chr12_90328476_T_C_b38	rs1405527	0,000042	-0,13	Thyroid
ENSG00000070961.15	ATP2B1	chr12_90330109_G_A_b38	rs12818395	0,000042	-0,13	Thyroid
ENSG00000070961.15	ATP2B1	chr12_90150155_C_T_b38	rs7135166	0,000042	-0,14	Esophagus - Mucosa
ENSG00000070961.15	ATP2B1	chr12_89709017_C_A_b38	rs12369944	0,000044	0,18	Brain - Frontal Cortex (BA9)
ENSG00000070961.15	ATP2B1	chr12_89966286_A_G_b38	rs10745520	0,000044	-0,13	Esophagus - Mucosa

ENSG00000070961.15	ATP2B1	chr12_89702020_T_A_b38	rs11105380	0,000045	-0,14	Artery - Tibial
ENSG00000070961.15	ATP2B1	chr12_90153750_C_G_b38	rs2118803	0,000047	-0,14	Esophagus - Mucosa
ENSG00000070961.15	ATP2B1	chr12_90568565_A_G_b38	rs35520023	0,000048	0,13	Adipose - Subcutaneous
ENSG00000070961.15	ATP2B1	chr12_90629207_G_A_b38	rs11105704	0,000048	-0,27	Colon - Transverse
ENSG00000070961.15	ATP2B1	chr12_89666809_G_A_b38	rs17249754	0,000051	0,19	Artery - Aorta
ENSG00000070961.15	ATP2B1	chr12_89668599_G_A_b38	rs6538195	0,000051	0,19	Artery - Aorta
ENSG00000070961.15	ATP2B1	chr12_89678299_G_A_b38	rs73437358	0,000051	0,19	Artery - Aorta
ENSG00000070961.15	ATP2B1	chr12_89913265_C_T_b38	rs7972820	0,000053	-0,13	Esophagus - Mucosa
ENSG00000070961.15	ATP2B1	chr12_89784106_A_T_b38	rs113133867	0,000054	0,55	Artery - Tibial
ENSG00000070961.15	ATP2B1	chr12_89632685_G_A_b38	rs11105352	0,000054	0,19	Artery - Aorta
ENSG00000070961.15	ATP2B1	chr12_89632686_C_A_b38	rs11105353	0,000054	0,19	Artery - Aorta
ENSG00000070961.15	ATP2B1	chr12_89632746_A_G_b38	rs11105354	0,000054	0,19	Artery - Aorta
ENSG00000070961.15	ATP2B1	chr12_89656726_A_G_b38	rs12579302	0,000054	0,19	Artery - Aorta
ENSG00000070961.15	ATP2B1	chr12_89665065_G_A_b38	rs111478946	0,000054	0,19	Artery - Aorta
ENSG00000070961.15	ATP2B1	chr12_89675499_T_G_b38	rs11105364	0,000054	0,19	Artery - Aorta
ENSG00000070961.15	ATP2B1	chr12_90158457_G_GT_b38	rs79468373	0,000054	-0,14	Esophagus - Mucosa
ENSG00000070961.15	ATP2B1	chr12_89909790_G_C_b38	rs7957657	0,000057	-0,13	Esophagus - Mucosa
ENSG00000070961.15	ATP2B1	chr12_90328476_T_C_b38	rs1405527	0,000057	-0,15	Esophagus - Muscularis
ENSG00000070961.15	ATP2B1	chr12_90329398_C_T_b38	rs10858974	0,000057	-0,15	Esophagus - Muscularis
ENSG00000070961.15	ATP2B1	chr12_90330109_G_A_b38	rs12818395	0,000057	-0,15	Esophagus - Muscularis
ENSG00000070961.15	ATP2B1	chr12_90026116_GT_G_b38	rs11324040	0,000058	-0,13	Esophagus - Mucosa
ENSG00000070961.15	ATP2B1	chr12_89629273_T_C_b38	rs116858620	0,00006	0,43	Lung
ENSG00000070961.15	ATP2B1	chr12_90035251_A_G_b38	rs7311631	0,00006	-0,13	Esophagus - Mucosa
ENSG00000070961.15	ATP2B1	chr12_89879521_G_A_b38	rs2553100	0,00006	-0,13	Esophagus - Mucosa
ENSG00000070961.15	ATP2B1	chr12_89944741_G_A_b38	rs4842698	0,000062	-0,18	Artery - Tibial
ENSG00000070961.15	ATP2B1	chr12_89680664_G_C_b38	rs11105368	0,000063	0,19	Artery - Aorta
ENSG00000070961.15	ATP2B1	chr12_90577787_T_C_b38	rs11105685	0,000063	0,13	Adipose - Subcutaneous
ENSG00000070961.15	ATP2B1	chr12_89681466_C_T_b38	rs4842675	0,000065	0,19	Artery - Aorta
ENSG00000070961.15	ATP2B1	chr12_89619312_T_C_b38	rs2681492	0,000066	0,19	Artery - Aorta
ENSG00000070961.15	ATP2B1	chr12_89615182_A_G_b38	rs2681472	0,000066	0,19	Artery - Aorta
ENSG00000070961.15	ATP2B1	chr12_89956222_G_A_b38	rs10777213	0,000066	-0,13	Esophagus - Mucosa
ENSG00000070961.15	ATP2B1	chr12_89958659_C_T_b38	rs7306228	0,000066	-0,13	Esophagus - Mucosa
ENSG00000070961.15	ATP2B1	chr12_90039790_A_G_b38	rs6538218	0,000066	-0,13	Esophagus - Mucosa
ENSG00000070961.15	ATP2B1	chr12_89912752_T_C_b38	rs7135197	0,000067	-0,13	Esophagus - Mucosa
ENSG00000070961.15	ATP2B1	chr12_89915156_G_A_b38	rs7959788	0,000067	-0,13	Esophagus - Mucosa
ENSG00000070961.15	ATP2B1	chr12_90152680_A_G_b38	rs10745525	0,000068	-0,18	Artery - Tibial
ENSG00000070961.15	ATP2B1	chr12_89837533_A_G_b38	rs2722224	0,000079	-0,13	Esophagus - Mucosa
ENSG00000070961.15	ATP2B1	chr12_89696964_C_T_b38	rs11105378	0,00008	0,19	Artery - Aorta
ENSG00000070961.15	ATP2B1	chr12_89695013_G_A_b38	rs10858917	0,00008	-0,17	Artery - Aorta
ENSG00000070961.15	ATP2B1	chr12_90050278_C_T_b38	rs55846104	0,000081	-0,19	Esophagus - Mucosa
ENSG00000070961.15	ATP2B1	chr12_90147932_C_T_b38	rs4608145	0,000083	-0,13	Lung
ENSG00000070961.15	ATP2B1	chr12_90087601_T_C_b38	rs7316395	0,000087	-0,13	Lung
ENSG00000070961.15	ATP2B1	chr12_90087981_A_G_b38	rs7300611	0,000087	-0,13	Lung
ENSG00000070961.15	ATP2B1	chr12_90089145_A_G_b38	rs10735278	0,000087	-0,13	Lung
ENSG00000070961.15	ATP2B1	chr12_90089249_A_T_b38	rs10735279	0,000087	-0,13	Lung
ENSG00000070961.15	ATP2B1	chr12_90089939_T_G_b38	rs10858950	0,000087	-0,13	Lung
ENSG00000070961.15	ATP2B1	chr12_90090107_T_C_b38	rs11105505	0,000087	-0,13	Lung
ENSG00000070961.15	ATP2B1	chr12_89966684_C_T_b38	rs4584633	0,00009	-0,17	Artery - Tibial
ENSG00000070961.15	ATP2B1	chr12_89921101_C_G_b38	rs4842693	0,000093	-0,13	Esophagus - Mucosa
ENSG00000070961.15	ATP2B1	chr12_90133970_C_T_b38	rs11105516	0,000094	-0,13	Lung
ENSG00000070961.15	ATP2B1	chr12_90022580_A_C_b38	rs10777219	0,000094	-0,14	Artery - Tibial
ENSG00000070961.15	ATP2B1	chr12_90024345_G_A_b38	rs10858943	0,000094	-0,14	Artery - Tibial
ENSG00000070961.15	ATP2B1	chr12_90157130_AT_A_b38	rs34734819	0,000099	-0,13	Esophagus - Mucosa
ENSG00000070961.15	ATP2B1	chr12_89694803_T_A_b38	rs11105375	0,0001	0,18	Artery - Aorta
ENSG00000070961.15	ATP2B1	chr12_89697090_A_G_b38	rs12230074	0,0001	0,18	Artery - Aorta
ENSG00000070961.15	ATP2B1	chr12_90148406_A_C_b38	rs1438984	0,0001	-0,13	Lung
ENSG00000070961.15	ATP2B1	chr12_90148426_G_A_b38	rs1438983	0,0001	-0,13	Lung
ENSG00000070961.15	ATP2B1	chr12_90042305_C_T_b38	rs7975953	0,0001	-0,14	Artery - Tibial
ENSG00000070961.15	ATP2B1	chr12_90042794_T_C_b38	rs7963304	0,0001	-0,14	Artery - Tibial
ENSG00000070961.15	ATP2B1	chr12_90110385_A_C_b38	rs10858955	0,00011	-0,13	Lung
ENSG00000070961.15	ATP2B1	chr12_90111572_G_A_b38	rs10745523	0,00011	-0,13	Lung
ENSG00000070961.15	ATP2B1	chr12_90114532_G_T_b38	rs10777224	0,00011	-0,13	Lung
ENSG00000070961.15	ATP2B1	chr12_90120301_C_G_b38	rs10858956	0,00011	-0,13	Lung
ENSG00000070961.15	ATP2B1	chr12_89336143_A_C_b38	rs10161308	0,00012	0,22	Artery - Tibial
ENSG00000070961.15	ATP2B1	chr12_89660842_T_C_b38	rs73437338	0,00012	0,19	Artery - Aorta
ENSG00000070961.15	ATP2B1	chr12_89591515_AAAGT_A_b38	rs10580742	0,00012	0,19	Artery - Aorta
ENSG00000070961.15	ATP2B1	chr12_89677042_CAAAG_C_b38	rs143087380	0,00012	-0,11	Thyroid
ENSG00000070961.15	ATP2B1	chr12_90099780_G_A_b38	rs7486390	0,00012	-0,13	Lung
ENSG00000070961.15	ATP2B1	chr12_90100728_G_C_b38	rs7303398	0,00012	-0,13	Lung
ENSG00000070961.15	ATP2B1	chr12_89694991_G_A_b38	rs11105376	0,00013	0,19	Artery - Aorta
ENSG00000070961.15	ATP2B1	chr12_90117803_G_C_b38	rs7486630	0,00013	-0,13	Lung

ENSG00000070961.15	ATP2B1	chr12_90119438_T_A_b38	rs7139353	0,00013	-0,13	Lung
ENSG00000070961.15	ATP2B1	chr12_90121102_T_C_b38	rs10777226	0,00013	-0,13	Lung
ENSG00000070961.15	ATP2B1	chr12_90122191_G_C_b38	rs6538227	0,00013	-0,13	Lung
ENSG00000070961.15	ATP2B1	chr12_90123327_G_T_b38	rs10858957	0,00013	-0,13	Lung
ENSG00000070961.15	ATP2B1	chr12_90123338_T_C_b38	rs10858958	0,00013	-0,13	Lung
ENSG00000070961.15	ATP2B1	chr12_90124075_G_A_b38	rs7315166	0,00013	-0,13	Lung
ENSG00000070961.15	ATP2B1	chr12_90124724_G_A_b38	rs4842713	0,00013	-0,13	Lung
ENSG00000070961.15	ATP2B1	chr12_90126369_C_T_b38	rs7138547	0,00013	-0,13	Lung
ENSG00000070961.15	ATP2B1	chr12_90127423_A_G_b38	rs10777227	0,00013	-0,13	Lung
ENSG00000070961.15	ATP2B1	chr12_90127443_A_G_b38	rs10777228	0,00013	-0,13	Lung
ENSG00000070961.15	ATP2B1	chr12_90128789_G_A_b38	rs12303180	0,00013	-0,13	Lung
ENSG00000070961.15	ATP2B1	chr12_90129235_T_C_b38	rs4842714	0,00013	-0,13	Lung
ENSG00000070961.15	ATP2B1	chr12_90130357_GCTC_G_b38	rs35647353	0,00013	-0,13	Lung
ENSG00000070961.15	ATP2B1	chr12_90132074_G_T_b38	rs10858961	0,00013	-0,13	Lung
ENSG00000070961.15	ATP2B1	chr12_90133198_A_AG_b38	rs79553876	0,00013	-0,13	Lung
ENSG00000070961.15	ATP2B1	chr12_90134620_G_C_b38	rs6538228	0,00013	-0,13	Lung
ENSG00000070961.15	ATP2B1	chr12_90137321_T_C_b38	rs1595599	0,00013	-0,13	Lung
ENSG00000070961.15	ATP2B1	chr12_90137388_G_A_b38	rs1595598	0,00013	-0,13	Lung
ENSG00000070961.15	ATP2B1	chr12_90137720_T_G_b38	rs7304226	0,00013	-0,13	Lung
ENSG00000070961.15	ATP2B1	chr12_90139086_C_T_b38	rs7295818	0,00013	-0,13	Lung
ENSG00000070961.15	ATP2B1	chr12_90141861_G_T_b38	rs1438986	0,00013	-0,13	Lung
ENSG00000070961.15	ATP2B1	chr12_90142076_T_G_b38	rs1438985	0,00013	-0,13	Lung
ENSG00000070961.15	ATP2B1	chr12_90142537_C_A_b38	rs1470031	0,00013	-0,13	Lung
ENSG00000070961.15	ATP2B1	chr12_90142786_G_A_b38	rs1470030	0,00013	-0,13	Lung
ENSG00000070961.15	ATP2B1	chr12_90144066_A_C_b38	rs10745524	0,00013	-0,13	Lung
ENSG00000070961.15	ATP2B1	chr12_90144234_A_G_b38	rs1470029	0,00013	-0,13	Lung
ENSG00000070961.15	ATP2B1	chr12_90144899_A_T_b38	rs4842715	0,00013	-0,13	Lung
ENSG00000070961.15	ATP2B1	chr12_90145400_C_A_b38	rs4842716	0,00013	-0,13	Lung
ENSG00000070961.15	ATP2B1	chr12_90145401_C_T_b38	rs4842717	0,00013	-0,13	Lung
ENSG00000070961.15	ATP2B1	chr12_90145987_C_A_b38	rs1344962	0,00013	-0,13	Lung
ENSG00000070961.15	ATP2B1	chr12_90146644_T_C_b38	rs11105517	0,00013	-0,13	Lung
ENSG00000070961.15	ATP2B1	chr12_90147279_C_G_b38	rs1344961	0,00013	-0,13	Lung
ENSG00000070961.15	ATP2B1	chr12_90147385_C_G_b38	rs2218085	0,00013	-0,13	Lung
ENSG00000070961.15	ATP2B1	chr12_90147644_A_C_b38	rs2196783	0,00013	-0,13	Lung
ENSG00000070961.15	ATP2B1	chr12_90002703_T_C_b38	rs7964216	0,00013	-0,14	Artery - Tibial
ENSG00000070961.15	ATP2B1	chr12_90004485_T_C_b38	rs10777218	0,00013	-0,14	Artery - Tibial
ENSG00000070961.15	ATP2B1	chr12_90005574_C_T_b38	rs11105483	0,00013	-0,14	Artery - Tibial
ENSG00000070961.15	ATP2B1	chr12_90015717_C_T_b38	rs61926987	0,00013	-0,14	Artery - Tibial
ENSG00000070961.15	ATP2B1	chr12_90159905_G_A_b38	rs6538230	0,00014	-0,16	Artery - Tibial
ENSG00000070961.15	ATP2B1	chr12_89547597_G_A_b38	rs4842665	0,00015	0,12	Artery - Tibial
ENSG00000070961.15	ATP2B1	chr12_89865713_T_C_b38	rs2722213	0,00015	-0,12	Esophagus - Mucosa
ENSG00000070961.15	ATP2B1	chr12_89866278_G_A_b38	rs2553097	0,00015	-0,12	Esophagus - Mucosa
ENSG00000070961.15	ATP2B1	chr12_89875126_G_A_b38	rs2553104	0,00015	-0,12	Esophagus - Mucosa
ENSG00000070961.15	ATP2B1	chr12_90071866_G_A_b38	rs6538222	0,00015	-0,13	Lung
ENSG00000070961.15	ATP2B1	chr12_89851601_T_C_b38	rs2553101	0,00015	-0,13	Esophagus - Mucosa
ENSG00000070961.15	ATP2B1	chr12_89637618_C_T_b38	rs10858914	0,00017	-0,12	Artery - Tibial
ENSG00000070961.15	ATP2B1	chr12_90010069_T_C_b38	rs4393376	0,00017	-0,15	Artery - Tibial
ENSG00000070961.15	ATP2B1	chr12_90016872_A_C_b38	rs6538217	0,00017	-0,15	Artery - Tibial
ENSG00000070961.15	ATP2B1	chr12_89904501_A_C_b38	rs7965284	0,00017	-0,18	Artery - Tibial
ENSG00000070961.15	ATP2B1	chr12_90128372_C_T_b38	rs10858959	0,00019	-0,13	Artery - Tibial
ENSG00000070961.15	ATP2B1	chr12_90129926_G_A_b38	rs10858960	0,00019	-0,13	Artery - Tibial
ENSG00000070961.15	ATP2B1	chr12_89943230_A_C_b38	rs4842696	0,0002	-0,14	Esophagus - Mucosa
ENSG00000070961.15	ATP2B1	chr12_89345678_C_G_b38	rs11105262	0,00022	0,21	Artery - Tibial
ENSG00000070961.15	ATP2B1	chr12_89861997_C_A_b38	rs1946327	0,00023	-0,12	Esophagus - Mucosa
ENSG00000070961.15	ATP2B1	chr12_90003409_T_C_b38	rs4453292	0,00023	-0,15	Artery - Tibial
ENSG00000070961.15	ATP2B1	chr12_90162353_T_C_b38	rs2731241	0,00023	-0,16	Artery - Tibial
ENSG00000070961.15	ATP2B1	chr12_90164205_A_G_b38	rs1438980	0,00023	-0,16	Artery - Tibial
ENSG00000070961.15	ATP2B1	chr12_89434120_G_A_b38	rs118130015	0,00027	0,33	Artery - Tibial
ENSG00000070961.15	ATP2B1	chr12_90173201_C_T_b38	rs1347851	0,00027	-0,15	Artery - Tibial
ENSG00000070961.15	ATP2B1	chr12_89623959_G_T_b38	rs2070759	0,00028	-0,11	Artery - Tibial
ENSG00000070961.15	ATP2B1	chr12_89646107_G_A_b38	rs939329	0,00028	-0,11	Artery - Tibial
ENSG00000070961.15	ATP2B1	chr12_90149730_G_A_b38	rs10777230	0,00028	-0,12	Artery - Tibial
ENSG00000070961.15	ATP2B1	chr12_89857319_C_T_b38	rs12371308	0,00028	-0,13	Artery - Tibial
ENSG00000070961.15	ATP2B1	chr12_89857983_T_C_b38	rs11105439	0,00028	-0,13	Artery - Tibial

Table S4: eQTLs SNPs for ATP2B1 gene by using "Genotype-Tissue Expression" GTex database ($P<1x10^{-6}$).

N.77 SNPs acting as eQTLs for ATP2B1 gene annotated with prediction functional scores calculated by the "Genome-Wide Annotation of Variants" GWAVA tool are shown. N.8 SNPs are not reported in GWAVA are thus excluded. The ID, the chromosome, the position and the region score are listed. In bold, the top six are selected (rs11105352, rs11105353, rs10777221, rs73437358, rs111337717 and rs2681492).

ID	Chr.	Position	Region score
rs11105352	**12**	**90.026.462**	**0,63**
rs11105353	**12**	**90.026.463**	**0,61**
rs10777221	**12**	**90.441.215**	**0,52**
rs73437358	**12**	**90.072.076**	**0,48**
rs111337717	**12**	**90.037.506**	**0,47**
rs2681492	**12**	**90.013.089**	**0,47**
rs7136259	12	90.081.188	0,46
rs17249754	12	90.060.586	0,43
rs11105382	12	90.107.272	0,43
rs73437338	12	90.054.619	0,42
rs2280715	12	90.103.702	0,42
rs149193253	12	90.418.172	0,42
rs4842699	12	90.345.607	0,41
rs114744356	12	90.400.573	0,41
rs7488223	12	90.404.051	0,41
rs11105354	12	90.026.523	0,4
rs11105337	12	89.993.507	0,39
rs2681472	12	90.008.959	0,39
rs11105364	12	90.069.276	0,39
rs10777217	12	90.385.294	0,39
rs10745511	12	90.097.667	0,38
rs2408046	12	90.109.337	0,38
rs1401982	12	89.989.599	0,37
rs12579302	12	90.050.503	0,37
rs4842675	12	90.075.243	0,37
rs11105379	12	90.095.173	0,37
rs7299436	12	90.113.070	0,37
rs73208536	12	90.428.028	0,37
rs8181784	12	89.828.591	0,36
rs10777163	12	89.830.720	0,36
rs6538195	12	90.062.376	0,35
rs4842676	12	90.091.782	0,35
rs2113894	12	90.099.397	0,35
rs1980235	12	90.110.782	0,35
rs7488974	12	90.442.001	0,35
rs150184539	12	90.443.478	0,35
rs150119566	12	90.537.682	0,35
rs12230074	12	90.090.867	0,34
rs1358350	12	90.101.892	0,34
rs73437382	12	90.102.945	0,34
rs11105381	12	90.106.835	0,34
rs2681485	12	90.025.622	0,33
rs11105368	12	90.074.441	0,33

rs11105378	12	90.090.741	0,33
rs7313874	12	89.965.049	0,32
rs1689040	12	89.978.233	0,32
rs111478946	12	90.058.842	0,32
rs11105383	12	90.107.306	0,32
rs12579052	12	90.132.147	0,32
rs1594565	12	90.779.022	0,32
rs10858918	12	90.096.345	0,31
rs4408360	12	90.394.861	0,31
rs11105287	12	89.829.470	0,3
rs7968803	12	90.390.780	0,3
rs4842666	12	89.941.549	0,29
rs11105328	12	89.942.390	0,29
rs10858917	12	90.088.790	0,29
rs7302816	12	89.950.320	0,28
rs1590008	12	90.107.725	0,28
rs4466894	12	90.362.052	0,27
rs55849728	12	90.533.915	0,27
rs11105375	12	90.088.580	0,26
rs4842697	12	90.337.046	0,26
rs77187603	12	90.531.484	0,25
rs10858944	12	90.419.192	0,24
rs11105376	12	90.088.768	0,23
rs4842701	12	90.367.700	0,19
rs117742247	12	89.991.313	0,16
rs57481061	12	90.019.178	0,14

Table S5: Differentially expressed proteins in HEK293T-ACE2 upon treatment with 1 μM PI-7 molecule for 24 hours.

Proteomic analysis in HEK293T-ACE2 upon treatment with 1 μM PI-7 molecule for 24 hours In the treated cells we found n.17 downregulated and n.66 upregulated proteins. The protein entry, the protein names, the gene names, the log2 fold changes (log2FC), the fold change (FC), the Student's T-test FDR, the number of pepdides (Razor + unique peptides) and the percentage of the sequence coverage (Unique + razon sequence coverage) are shown.

Entry	Protein name	Gene name	log2FC	FC	Student's *t*-test FDR	Razor + unique peptides	Unique + razor sequence coverage (%)
Q6FI81	Anamorsin	CIAPIN1	-0,92	0,53	3,71E-02	4	24,4
P55145	Mesencephalic astrocyte-derived neurotrophic factor	MANF	-0,87	0,55	4,88E-02	6	33
P10412	Histone H1.4	HIST1H1E	-0,73	0,60	5,44E-04	12	32,4
P51572	B-cell receptor-associated protein 31	BCAP31	-0,72	0,61	6,31E-03	7	26
P62280	40S ribosomal protein S11	RPS11	-0,70	0,61	5,76E-03	8	41,1
P47813	Eukaryotic translation initiation factor 1A, X-chromosomal	EIF1AX	-0,70	0,62	3,17E-03	6	34
P62750	60S ribosomal protein L23a	RPL23A	-0,62	0,65	3,54E-03	9	37,2
P62979	Ubiquitin-40S ribosomal protein S27a	RPS27A	-0,62	0,65	5,82E-05	12	55,8
P84090	Enhancer of rudimentary homolog	ERH	-0,58	0,67	1,32E-02	4	37,5
P60866	40S ribosomal protein S20	RPS20	-0,58	0,67	2,10E-03	4	28,6
P35613	Basigin	BSG	-0,57	0,67	2,79E-03	6	22,9
Q9H444	Charged multivesicular body protein 4b	CHMP4B	-0,57	0,67	5,54E-04	6	27,7
Q07020	60S ribosomal protein L18	RPL18	-0,56	0,68	9,09E-03	7	35,6
P42677	40S ribosomal protein S27	RPS27	-0,55	0,68	2,24E-04	5	40,5
P25788	Proteasome subunit alpha type-3	PSMA3	-0,52	0,70	5,44E-04	6	22,4
P13073	Cytochrome c oxidase subunit 4 isoform 1, mitochondrial	COX4I1	-0,50	0,71	7,07E-03	6	31,4
Q9BRA2	Thioredoxin domain-containing protein 17	TXNDC17	-0,50	0,71	3,68E-03	4	46,3
P38159	RNA-binding motif protein, X chromosome	RBMX	-0,50	0,71	2,35E-04	10	26,1
P48643	T-complex protein 1 subunit epsilon	CCT5	0,50	1,41	6,28E-04	28	68,6
P12532	Creatine kinase U-type, mitochondrial	CKMT1A	0,50	1,41	6,28E-04	7	35,5
P04844	Dolichyl-diphosphooligosaccharide--protein glycosyltransferase subunit 2	RPN2	0,50	1,41	1,71E-04	16	39,9
Q9Y5L0	Transportin-3	TNPO3	0,50	1,41	4,25E-02	6	11,1
P63208	S-phase kinase-associated protein 1	SKP1	0,50	1,41	7,76E-03	5	33,7
P06748	Nucleophosmin	NPM1	0,51	1,42	3,58E-03	11	36,4
O15160	DNA-directed RNA polymerases I and III subunit RPAC1	POLR1C	0,52	1,43	3,37E-03	5	21,7
Q9Y285	Phenylalanine--tRNA ligase alpha subunit	FARSA	0,52	1,44	1,69E-02	6	19,5
P23921	Ribonucleoside-diphosphate reductase large subunit	RRM1	0,53	1,44	8,05E-03	8	19,4

Q13126	S-methyl-5-thioadenosine phosphorylase	MTAP	0,55	1,46	3,11E-03	8	48,1
Q9BSJ8	Extended synaptotagmin-1	ESYT1	0,55	1,47	1,37E-02	5	6,4
Q15435	Protein phosphatase 1 regulatory subunit 7	PPP1R7	0,55	1,47	4,65E-03	6	23,9
Q92616	eIF-2-alpha kinase activator GCN1	GCN1	0,55	1,47	1,74E-04	35	21
P24534	Elongation factor 1-beta	EEF1B2	0,56	1,47	2,75E-03	5	37,3
P09104	Gamma-enolase	ENO2	0,56	1,47	2,35E-04	13	48,6
Q14257	Reticulocalbin-2	RCN2	0,57	1,49	6,68E-03	4	20,8
P62917	60S ribosomal protein L8	RPL8	0,58	1,50	9,79E-03	7	33,9
Q8IY67	Ribonucleoprotein PTB-binding 1	RAVER1	0,58	1,50	2,35E-04	5	17,3
Q8IZL8	Proline-, glutamic acid- and leucine-rich protein 1	PELP1	0,59	1,51	3,75E-03	6	9,4
P61011	Signal recognition particle 54 kDa protein	SRP54	0,60	1,51	2,37E-02	7	21
Q9UBE0	SUMO-activating enzyme subunit 1	SAE1	0,60	1,52	4,37E-04	11	47,1
Q6P1J9	Parafibromin	CDC73	0,60	1,52	2,70E-02	4	9,6
Q9ULC4	Malignant T-cell-amplified sequence 1	MCTS1	0,62	1,54	3,58E-03	7	57,5
P47985	Cytochrome b-c1 complex subunit Rieske, mitochondrial	UQCRFS1	0,62	1,54	3,37E-03	4	22,6
Q8N3U4	Cohesin subunit SA-2	STAG2	0,63	1,55	1,48E-02	7	8,1
P26038	Moesin	MSN	0,63	1,55	5,64E-03	7	15,8
P60953	Cell division control protein 42 homolog	CDC42	0,63	1,55	7,15E-03	8	48,2
Q15021	Condensin complex subunit 1	NCAPD2	0,64	1,55	3,53E-03	14	16,2
Q96P70	Importin-9	IPO9	0,66	1,58	1,03E-02	5	9,1
P26599	Polypyrimidine tract-binding protein 1	PTBP1	0,66	1,59	2,24E-04	16	52
Q9C0B1	Alpha-ketoglutarate-dependent dioxygenase FTO	FTO	0,67	1,59	6,56E-03	7	20,4
Q92896	Golgi apparatus protein 1	GLG1	0,69	1,61	2,52E-02	4	4,8
Q96CS3	FAS-associated factor 2	FAF2	0,69	1,62	2,35E-04	4	16,2
P61970	Nuclear transport factor 2	NUTF2	0,70	1,62	3,58E-03	5	69,3
P63010	AP-2 complex subunit beta	AP2B1	0,70	1,63	2,39E-04	10	20,4
P04632	Calpain small subunit 1	CAPNS1	0,71	1,63	3,81E-02	5	31
Q9Y6G9	Cytoplasmic dynein 1 light intermediate chain 1	DYNC1LI1	0,73	1,65	2,07E-03	5	18,4
Q9HAV4	Exportin-5	XPO5	0,73	1,65	2,21E-03	13	15,9
O75947	ATP synthase subunit d, mitochondrial	ATP5PD	0,73	1,66	1,71E-03	8	64
P08708	40S ribosomal protein S17	RPS17	0,74	1,67	9,90E-04	8	60
P20290	Transcription factor BTF3	BTF3	0,75	1,68	1,20E-03	6	48,1
Q96AC1	Fermitin family homolog 2	FERMT2	0,75	1,68	1,48E-02	8	18,4
Q5JTH9	RRP12-like protein	RRP12	0,79	1,72	4,43E-02	11	12,8
Q9H0A0	RNA cytidine acetyltransferase	NAT10	0,79	1,73	5,44E-04	12	17,2
Q96T76	MMS19 nucleotide excision repair protein homolog	MMS19	0,80	1,75	5,44E-04	6	10,2
P62081	40S ribosomal protein S7	RPS7	0,82	1,76	2,31E-03	12	55,7
O00429	Dynamin-1-like protein	DNM1L	0,82	1,77	1,42E-03	12	27,3
P35270	Sepiapterin reductase	SPR	0,87	1,83	1,81E-02	4	24,5
O00764	Pyridoxal kinase	PDXK	0,87	1,83	1,97E-02	4	21,2
O15260	Surfeit locus protein 4	SURF4	0,88	1,83	1,82E-03	4	18,2
Q9BXW7	Haloacid dehalogenase-like hydrolase domain-containing 5	HDHD5	0,92	1,89	2,99E-03	6	25,1
P61086	Ubiquitin-conjugating enzyme E2 K	UBE2K	0,92	1,90	3,36E-02	4	33
P99999	Cytochrome c	CYCS	0,97	1,95	6,59E-04	4	41
Q14978	Nucleolar and coiled-body phosphoprotein 1	NOLC1	1,01	2,01	2,14E-02	8	15,2
Q99436	Proteasome subunit beta type-7	PSMB7	1,01	2,02	7,16E-03	6	34,3
Q9GZS3	WD repeat-containing protein 61	WDR61	1,02	2,02	2,21E-03	4	26,9
Q9BWD1	Acetyl-CoA acetyltransferase, cytosolic	ACAT2	1,03	2,04	2,07E-04	5	35
Q05639	Elongation factor 1-alpha 2	EEF1A2	1,04	2,05	8,77E-04	8	38,2
Q14011	Cold-inducible RNA-binding protein	CIRBP	1,06	2,09	4,55E-04	4	32
Q16836	Hydroxyacyl-coenzyme A dehydrogenase, mitochondrial	HADH	1,07	2,09	4,26E-04	8	42,4

Q8N684	Cleavage and polyadenylation specificity factor subunit 7	CPSF7	1,08	2,11	2,71E-02	4	13,4
Q99598	Translin-associated protein X	TSNAX	1,11	2,16	7,56E-03	4	22,8
Q15428	Splicing factor 3A subunit 2	SF3A2	1,11	2,17	4,19E-02	7	24,4
P25787	Proteasome subunit alpha type-2	PSMA2	1,12	2,17	1,71E-04	7	45,7
P07602	Prosaposin	PSAP	1,31	2,47	2,35E-02	4	9,2
Q7L1Q6	Basic leucine zipper and W2 domain-containing protein 1	BZW1	2,10	4,28	1,76E-03	8	23,4

Table S6: List of the proteins taking part in the interaction network by using those proteins upregulated by PI-7 compound in HEK293T-ACE2 cells.

The proteins taking part to the neural network generated through the "Search Tool for Retrieval of Interacting Genes/Proteins" (STRING) database by using as input those proteins upregulated by PI-7 molecule in HEK293T-ACE2 cells after 24 hours treatment are shown. The Term ID, the term description, the observed gene count in the network, the background gene count, the strength, the false discovery rate (FDR) and the protein names are listed.

Term ID	**Term description**	**Observed gene count**	**Background gene count**	**Strength**	**FDR**	**Matching proteins in the network**
GO:0034641	Cellular nitrogen compound metabolic process	32	3282	0.46	3.69e-05	EEF1A2,SF3A2,SPR,NAT10,RPL8,XPO5,WDR61,PDXK,RAVER1,NPM1,GCN1L1,RRM1,PELP1,ATP5H,FARSA,RPS7,CPSF7,RPS17,PTBP1,TSNAX,CDC73,MCTS1,POLR1C,MTAP,BTF3,EEF1B2,PSAP,NOLC1,MMS19,FTO,ENO2,RRP12
GO:0010608	Posttranscriptional regulation of gene expression	14	574	0.86	4.75e-05	EEF1A2,PSMA2,NAT10,PSMB7,XPO5,NPM1,GCN1L1,PTBP1,TSNAX,MCTS1,EEF1B2,NOLC1,FTO,CIRBP
GO:0044237	Cellular metabolic process	48	7513	0.28	7.28e-05	EEF1A2,SF3A2,PSMA2,SKP1,SPR,RPN2,NAT10,PSMB7,UBE2K,FAF2,RPL8,XPO5,ESYT1,WDR61,SAE1,PDXK,RAVER1,NPM1,GCN1L1,RRM1,PELP1,ATP5H,UQCRFS1,CYCS,FARSA,CECR5,RPS7,CPSF7,RPS17,PTBP1,TSNAX,ACAT2,CDC73,MCTS1,POLR1C,MTAP,BTF3,EEF1B2,PSAP,CDC42,NOLC1,CKMT1A,MMS19,FTO,ENO2,RRP12,HADH,AP2B1
GO:0006807	Nitrogen compound metabolic process	45	6852	0.29	0.00015	EEF1A2,SF3A2,PSMA2,SKP1,SPR,RPN2,CAPNS1,NAT10,PSMB7,UBE2K,FAF2,RPL8,XPO5,ESYT1,WDR61,SAE1,PDXK,RAVER1,NPM1,GCN1L1,RRM1,PELP1,ATP5H,CYCS,FARSA,RPS7,CPSF7,RPS17,PTBP1,TSNAX,CDC73,MCTS1,POLR1C,MTAP,BTF3,EEF1B2,PSAP,CDC42,NOLC1,CKMT1A,MMS19,FTO,ENO2,RRP12,AP2B1
GO:0071704	Organic substance metabolic process	48	7755	0.26	0.00015	EEF1A2,SF3A2,PSMA2,SKP1,SPR,RPN2,CAPNS1,NAT10,PSMB7,UBE2K,FAF2,RPL8,XPO5,ESYT1,WDR61,SAE1,PDXK,RAVER1,NPM1,GCN1L1,RRM1,PELP1,ATP5H,CYCS,FARSA,CECR5,RPS7,CPSF7,RPS17,PTBP1,TSNAX,ACAT2,CDC73,MCTS1,POLR1C,MTAP,BTF3,EEF1B2,PSAP,CDC42,NOLC1,CKMT1A,MMS19,FTO,ENO2,RRP12,HADH,AP2B1
GO:0010467	Gene expression	23	2056	0.52	0.00027	EEF1A2,SF3A2,NAT10,RPL8,WDR61,RAVER1,GCN1L1,PELP1,FARSA,RPS7,CPSF7,RPS17,PTBP1,TSNAX,CDC73,MCTS1,POLR1C,BTF3,EEF1B2,PSAP,NOLC1,MMS19,RRP12
GO:0006725	Cellular aromatic compound metabolic process	27	2882	0.44	0.00030	SF3A2,SPR,NAT10,RPL8,XPO5,WDR61,PDXK,RAVER1,NPM1,RRM1,PELP1,ATP5H,FARSA,RPS7,CPSF7,RPS17,PTBP1,TSNAX,CDC73,POLR1C,MTAP,BTF3,NOLC1,MMS19,FTO,ENO2,RRP12
GO:0008152	Metabolic process	49	8298	0.24	0.00030	EEF1A2,SF3A2,PSMA2,SKP1,SPR,RPN2,CAPNS1,NAT10,PSMB7,UBE2K,FAF2,RPL8,XPO5,ESYT1,WDR61,SAE1,PDXK,RAVER1,NPM1,GCN1L1,RRM1,PELP1,ATP5H,UQCRFS1,CYCS,FARSA,CECR5,RPS7,CPSF7,RPS17,PTBP1,TSNAX,ACAT2,CDC73,MCTS1,POLR1C,MTAP,BTF3,EEF1B2,PSAP,CDC42,NOLC1,CKMT1A,MMS19,FTO,ENO2,RRP12,HADH,AP2B1

GO:0016070	RNA metabolic process	20	1584	0.57	0.00030	SF3A2,NAT10,RPL8,XPO5,WDR61,RAVER1,PELP1,FARSA,RPS7,CPSF7,RPS17,PTBP1,TSNAX,CDC73,POLR1C,BTF3,NOLC1,MMS19,FTO,RRP12
GO:0022613	Ribonucleoprotein complex biogenesis	11	423	0.89	0.00030	SF3A2,NAT10,NPM1,PELP1,RPS7,CPSF7,RPS17,CDC73,MCTS1,NOLC1,RRP12
GO:0046483	Heterocycle metabolic process	27	2840	0.45	0.00030	SF3A2,SPR,NAT10,RPL8,XPO5,WDR61,PDXK,RAVER1,NPM1,RRM1,PELP1,ATP5H,FARSA,RPS7,CPSF7,RPS17,PTBP1,TSNAX,CDC73,POLR1C,MTAP,BTF3,NOLC1,MMS19,FTO,ENO2,RRP12
GO:1901360	Organic cyclic compound metabolic process	28	3118	0.43	0.00033	SF3A2,SPR,NAT10,RPL8,XPO5,WDR61,PDXK,RAVER1,NPM1,RRM1,PELP1,ATP5H,FARSA,RPS7,CPSF7,RPS17,PTBP1,TSNAX,ACAT2,CDC73,POLR1C,MTAP,BTF3,NOLC1,MMS19,FTO,ENO2,RRP12
GO:0044238	Primary metabolic process	45	7332	0.26	0.00043	EEF1A2,SF3A2,PSMA2,SKP1,RPN2,CAPNS1,NAT10,PSMB7,UBE2K,FAF2,RPL8,XPO5,ESYT1,WDR61,SAE1,RAVER1,NPM1,GCN1L1,RRM1,PELP1,ATP5H,CYCS,FARSA,CECR5,RPS7,CPSF7,RPS17,PTBP1,TSNAX,ACAT2,CDC73,MCTS1,POLR1C,MTAP,BTF3,EEF1B2,PSAP,CDC42,NOLC1,MMS19,FTO,ENO2,RRP12,HADH,AP2B1
GO:0044271	Cellular nitrogen compound biosynthetic process	19	1522	0.57	0.00043	EEF1A2,SPR,RPL8,WDR61,PDXK,GCN1L1,RRM1,ATP5H,FARSA,RPS7,CPSF7,RPS17,CDC73,MCTS1,POLR1C,MTAP,BTF3,EEF1B2,MMS19
GO:0006139	Nucleobase-containing compound metabolic process	25	2659	0.45	0.00068	SF3A2,NAT10,RPL8,XPO5,WDR61,RAVER1,NPM1,RRM1,PELP1,ATP5H,FARSA,RPS7,CPSF7,RPS17,PTBP1,TSNAX,CDC73,POLR1C,MTAP,BTF3,NOLC1,MMS19,FTO,ENO2,RRP12
GO:0006417	Regulation of translation	10	398	0.87	0.00081	EEF1A2,NAT10,NPM1,GCN1L1,PTBP1,MCTS1,EEF1B2,NOLC1,FTO,CIRBP
GO:0016032	Viral process	13	776	0.7	0.0014	SKP1,PSMB7,RPL8,XPO5,DYNC1LI1,NPM1,RPS7,RPS17,PTBP1,MSN,MCTS1,CDC42,AP2B1
GO:0044085	Cellular component biogenesis	24	2583	0.44	0.0014	STAG2,SF3A2,SKP1,NAT10,UBE2K,NPM1,RRM1,PELP1,FARSA,RPS7,FERMT2,CPSF7,RPS17,CDC73,MCTS1,PSAP,CDC42,NOLC1,MMS19,RRP12,DNM1L,SRP54,CIRBP,AP2B1
GO:1901576	Organic substance biosynthetic process	24	2734	0.42	0.0032	EEF1A2,SPR,RPN2,RPL8,WDR61,PDXK,GCN1L1,RRM1,ATP5H,FARSA,CECR5,RPS7,CPSF7,RPS17,ACAT2,CDC73,MCTS1,POLR1C,MTAP,BTF3,EEF1B2,CKMT1A,MMS19,ENO2
GO:0090304	Nucleic acid metabolic process	21	2178	0.46	0.0036	SF3A2,NAT10,RPL8,XPO5,WDR61,RAVER1,NPM1,PELP1,FARSA,RPS7,CPSF7,RPS17,PTBP1,TSNAX,CDC73,POLR1C,BTF3,NOLC1,MMS19,FTO,RRP12
GO:0043170	Macromolecule metabolic process	38	6137	0.26	0.0054	EEF1A2,SF3A2,PSMA2,SKP1,RPN2,CAPNS1,NAT10,PSMB7,UBE2K,FAF2,RPL8,XPO5,WDR61,SAE1,RAVER1,NPM1,GCN1L1,RRM1,PELP1,CYCS,FARSA,RPS7,CPSF7,RPS17,PTBP1,TSNAX,CDC73,MCTS1,POLR1C,BTF3,EEF1B2,PSAP,CDC42,NOLC1,MMS19,FTO,RRP12,AP2B1
GO:1903311	Regulation of mrna metabolic process	8	338	0.85	0.0104	PSMA2,PSMB7,NPM1,CPSF7,PTBP1,CDC73,FTO,CIRBP
GO:0006396	RNA processing	12	854	0.62	0.0130	SF3A2,NAT10,RAVER1,PELP1,RPS7,CPSF7,RPS17,PTBP1,TSNAX,CDC73,NOLC1,RRP12
GO:0016055	Wnt signaling pathway	8	351	0.83	0.0130	PSMA2,SKP1,PSMB7,WDR61,FERMT2,CDC73,CDC42,AP2B1
GO:0051290	Protein heterotetramerization	3	15	1.77	0.0130	RRM1,FARSA,CPSF7
GO:0006412	Translation	8	366	0.81	0.0149	EEF1A2,RPL8,GCN1L1,FARSA,RPS7,RPS17,MCTS1,EEF1B2

GO:0031329	Regulation of cellular catabolic process	12	875	0.61	0.0149	EEF1A2,PSMA2,CAPNS1,PSMB7,UBE2K,NPM1,RPS7,MSN,PSAP,FTO,DNM1L,CIRBP
GO:0046907	Intracellular transport	16	1520	0.49	0.0149	NUTF2,FAF2,RPL8,XPO5,TNPO3,DYNC1LI1,NPM1,ATP5H,RPS7,RPS17,IPO9,PSAP,CDC42,DNM1L,SRP54,AP2B1
GO:0009987	Cellular process	63	15024	0.09	0.0158	GLG1,EEF1A2,STAG2,NUTF2,SF3A2,PSMA2,SKP1,SPR,RPN2,CAPNS1,NAT10,PSMB7,UBE2K,FAF2,RPL8,XPO5,TNPO3,ESYT1,WDR61,SAE1,DYNC1LI1,CCT5,PDXK,RAVER1,NPM1,GCN1L1,RRM1,PELP1,ATP5H,UQCRFS1,CYCS,FARSA,NCAPD2,CECR5,RPS7,FERMT2,CPSF7,RPS17,PTBP1,MSN,IPO9,TSNAX,ACAT2,CDC73,MCTS1,SURF4,POLR1C,MTAP,BTF3,EEF1B2,PSAP,CDC42,NOLC1,CKMT1A,MMS19,FTO,ENO2,RRP12,DNM1L,SRP54,CIRBP,HADH,AP2B1
GO:0032268	Regulation of cellular protein metabolic process	22	2693	0.38	0.0170	GLG1,EEF1A2,SKP1,PPP1R7,NAT10,UBE2K,WDR61,SAE1,NPM1,GCN1L1,CYCS,RPS7,PTBP1,MSN,MCTS1,EEF1B2,PSAP,CDC42,NOLC1,FTO,DNM1L,CIRBP
GO:0034645	Cellular macromolecule biosynthetic process	16	1592	0.47	0.0226	EEF1A2,RPN2,RPL8,WDR61,GCN1L1,RRM1,FARSA,RPS7,CPSF7,RPS17,CDC73,MCTS1,POLR1C,BTF3,EEF1B2,MMS19
GO:0042254	Ribosome biogenesis	7	292	0.85	0.0226	NAT10,NPM1,PELP1,RPS7,RPS17,NOLC1,RRP12
GO:0051641	Cellular localization	23	2967	0.36	0.0226	NUTF2,PSMA2,SKP1,PSMB7,FAF2,RPL8,XPO5,TNPO3,ESYT1,DYNC1LI1,PDXK,NPM1,ATP5H,RPS7,FERMT2,RPS17,IPO9,SURF4,PSAP,CDC42,DNM1L,SRP54,AP2B1
GO:0034613	Cellular protein localization	16	1610	0.47	0.0239	NUTF2,SKP1,FAF2,RPL8,XPO5,TNPO3,NPM1,RPS7,FERMT2,RPS17,IPO9,PSAP,CDC42,DNM1L,SRP54,AP2B1
GO:0051649	Establishment of localization in cell	20	2375	0.4	0.0241	NUTF2,PSMA2,PSMB7,FAF2,RPL8,XPO5,TNPO3,DYNC1LI1,PDXK,NPM1,ATP5H,RPS7,RPS17,IPO9,SURF4,PSAP,CDC42,DNM1L,SRP54,AP2B1
GO:0006364	rRNA processing	6	212	0.92	0.0264	NAT10,PELP1,RPS7,RPS17,NOLC1,RRP12
GO:0019080	Viral gene expression	5	132	1.05	0.0264	RPL8,RPS7,RPS17,PTBP1,MCTS1
GO:0044249	Cellular biosynthetic process	21	2611	0.38	0.0264	EEF1A2,SPR,RPN2,RPL8,WDR61,PDXK,GCN1L1,RRM1,ATP5H,FARSA,CECR5,RPS7,CPSF7,RPS17,CDC73,MCTS1,POLR1C,MTAP,BTF3,EEF1B2,MMS19
GO:0071840	Cellular component organization or biogenesis	34	5633	0.25	0.0264	STAG2,SF3A2,SKP1,CAPNS1,NAT10,UBE2K,FAF2,ESYT1,WDR61,DYNC1LI1,NPM1,RRM1,PELP1,ATP5H,CYCS,FARSA,NCAPD2,RPS7,FERMT2,CPSF7,RPS17,MSN,CDC73,MCTS1,SURF4,PSAP,CDC42,NOLC1,MMS19,RRP12,DNM1L,SRP54,CIRBP,AP2B1
GO:0042274	Ribosomal small subunit biogenesis	4	70	1.23	0.0293	NAT10,NPM1,RPS7,RPS17
GO:0072594	Establishment of protein localization to organelle	8	433	0.74	0.0293	NUTF2,RPL8,TNPO3,RPS7,RPS17,IPO9,SRP54,AP2B1
GO:0006886	Intracellular protein transport	12	999	0.55	0.0301	NUTF2,FAF2,RPL8,XPO5,TNPO3,NPM1,RPS7,RPS17,IPO9,PSAP,SRP54,AP2B1
GO:1904666	Regulation of ubiquitin protein ligase activity	3	26	1.53	0.0302	SKP1,RPS7,DNM1L
GO:1901566	Organonitrogen compound biosynthetic process	14	1346	0.49	0.0334	EEF1A2,SPR,RPN2,RPL8,PDXK,GCN1L1,ATP5H,FARSA,RPS7,RPS17,MCTS1,MTAP,EEF1B2,CKMT1A
GO:0034660	ncRNA metabolic process	8	467	0.71	0.0419	NAT10,XPO5,PELP1,FARSA,RPS7,RPS17,NOLC1,RRP12
GO:0048522	Positive regulation of cellular process	33	5579	0.24	0.0423	EEF1A2,NUTF2,SF3A2,PSMA2,SKP1,PPP1R7,CAPNS1,NAT10,PSMB7,UBE2K,XPO5,WDR61,SAE1,DYNC1LI1,CCT5,NPM1,GCN1L

						1,PELP1,CYCS,RPS7,PTBP1,MSN,CDC73,MCTS1,SURF4,PSAP,CDC42,NOLC1,MMS19,FTO,DNM1L,CIRBP,AP2B1
GO:0033365	Protein localization to organelle	10	743	0.6	0.0427	NUTF2,SKP1,RPL8,TNPO3,RPS7,RPS17,IPO9,DNM1L,SRP54,AP2B1
GO:0048518	Positive regulation of biological process	35	6112	0.23	0.0427	EEF1A2,NUTF2,SF3A2,PSMA2,SKP1,PPP1R7,CAPNS1,NAT10,PSMB7,UBE2K,XPO5,WDR61,SAE1,DYNC1LI1,CCT5,NPM1,GCN1L1,PELP1,CYCS,RPS7,PTBP1,MSN,CDC73,MCTS1,SURF4,POLR1C,PSAP,CDC42,NOLC1,MMS19,FTO,DNM1L,CIRBP,HADH,AP2B1
GO:0019222	Regulation of metabolic process	38	6948	0.21	0.0453	GLG1,EEF1A2,NUTF2,PSMA2,SKP1,PPP1R7,SPR,CAPNS1,NAT10,PSMB7,UBE2K,RPL8,XPO5,WDR61,SAE1,CCT5,NPM1,GCN1L1,PELP1,CYCS,RPS7,CPSF7,RPS17,PTBP1,MSN,TSNAX,CDC73,MCTS1,POLR1C,EEF1B2,PSAP,CDC42,NOLC1,MMS19,FTO,DNM1L,CIRBP,HADH

Table S7: List of the proteins taking part in the interaction network by using those proteins downregulated by PI-7 compound in HEK293T-ACE2 cells.

The proteins taking part to the neural network generated through the "Search Tool for Retrieval of Interacting Genes/Proteins" (STRING) database by using as input those proteins downregulated by PI-7 molecule in HEK293T-ACE2 cells after 24 hours treatment are shown. The Term ID, the term description, the observed gene count in the network, the background gene count, the strength, the false discovery rate (FDR) and the protein names are listed.

Term ID	**Term description**	**Observed gene count**	**Background gene count**	**Strength**	**FDR**	**Matching proteins in the network**
GO:0070972	Protein localization to endoplasmic reticulum	8	140	1.79	4.64e-09	CHMP4B,RPS11,RPS27A,RPS27,RPL23A,BCAP31,RPS20,RPL18
GO:0045047	Protein targeting to endoplasmic reticulum	7	110	1.84	4.39e-08	CHMP4B,RPS11,RPS27A,RPS27,RPL23A,RPS20,RPL18
GO:0006413	Translational initiation	7	141	1.73	1.16e-07	RPS11,RPS27A,RPS27,EIF1AX,RPL23A,RPS20,RPL18
GO:0006612	Protein targeting to membrane	7	165	1.66	2.69e-07	CHMP4B,RPS11,RPS27A,RPS27,RPL23A,RPS20,RPL18
GO:0006614	SRP-dependent cotranslational protein targeting to membrane	6	96	1.83	6.50e-07	RPS11,RPS27A,RPS27,RPL23A,RPS20,RPL18
GO:0019083	Viral transcription	6	115	1.75	1.38e-06	RPS11,RPS27A,RPS27,RPL23A,RPS20,RPL18
GO:0000184	Nuclear-transcribed mRNA catabolic process, nonsense-mediated decay	6	119	1.74	1.49e-06	RPS11,RPS27A,RPS27,RPL23A,RPS20,RPL18
GO:0072657	Protein localization to membrane	8	495	1.24	6.70e-06	CHMP4B,RPS11,RPS27A,BSG,RPS27,RPL23A,RPS20,RPL18
GO:0016032	Viral process	9	776	1.1	8.86e-06	PSMA3,CHMP4B,RPS11,RPS27A,RPS27,RPL23A,BCAP31,RPS20,RPL18
GO:0044265	Cellular macromolecule catabolic process	8	917	0.98	0.00035	PSMA3,CHMP4B,RPS11,RPS27A,RPS27,RPL23A,RPS20,RPL18
GO:0006886	Intracellular protein transport	8	999	0.94	0.00062	CHMP4B,RPS11,RPS27A,RPS27,RPL23A,BCAP31,RPS20,RPL18
GO:0016071	mRNA metabolic process	7	678	1.05	0.00065	RPS11,RPS27A,RPS27,RBMX,RPL23A,RPS20,RPL18
GO:0034613	Cellular protein localization	9	1610	0.78	0.0016	CHMP4B,RPS11,RPS27A,BSG,RPS27,RPL23A,BCAP31,RPS20,RPL18
GO:0044271	Cellular nitrogen compound biosynthetic process	8	1522	0.76	0.0095	RPS11,RPS27A,RPS27,RBMX,EIF1AX,RPL23A,RPS20,RPL18
GO:0034645	Cellular macromolecule biosynthetic process	8	1592	0.74	0.0118	RPS11,RPS27A,RPS27,RBMX,EIF1AX,RPL23A,RPS20,RPL18
GO:0008152	Metabolic process	16	8298	0.32	0.0167	PSMA3,CHMP4B,TXNDC17,RPS11,RPS27A,HIST1H1E,BSG,RPS27,RBMX,EIF1AX,CIAPIN1,RPL23A,RPS20,RPL18,ERH,COX4I1
GO:0034622	Cellular protein-containing complex assembly	6	816	0.9	0.0173	CHMP4B,RPS27A,HIST1H1E,RPS27,RBMX,RPL23A
GO:0051641	Cellular localization	10	2967	0.56	0.0220	CHMP4B,RPS11,RPS27A,BSG,RPS27,RPL23A,BCAP31,RPS20,MANF,RPL18
GO:0051649	Establishment of localization in cell	9	2375	0.61	0.0247	CHMP4B,RPS11,RPS27A,RPS27,RPL23A,BCAP31,RPS20,MANF,RPL18

GO:0044237	Cellular metabolic process	15	7513	0.34	0.0294	PSMA3,CHMP4B,RPS11,RPS27A,HIST1H1E,BSG,RPS27,RBMX,EIF1AX,CIAPIN1,RPL23A,RPS20,RPL18,ERH,COX4I1
GO:0010629	Negative regulation of gene expression	8	2014	0.64	0.0485	RPS11,RPS27A,HIST1H1E,RPS27,RBMX,RPL23A,RPS20,RPL18

References

Melms, J.C., Biermann, J., Huang, H., Wang, Y., Nair, A., Tagore, S., Katsyv, I., Rendeiro, A.F., Amin, A.D., Schapiro, D., et al. (2021). A molecular single-cell lung atlas of lethal COVID-19. Nature *595*, 114-119. 10.1038/s41586-021-03569-1.